

Conformal Coating of Three-Dimensional Nanostructures via Atomic Layer Deposition for Development of Advanced Energy Storage Devices and Plasmonic Transparent Conductors

By

Copyright 2015

Gary A. Malek

Submitted to the graduate degree program in Physics and the Graduate Faculty of the University of Kansas in partial fulfillment of the requirements for the degree of Doctor of Philosophy.

Chairperson: Dr. Judy Wu

Dr. Cindy Berrie

Dr. Wai-Lun Chan

Dr. Siyuan Han

Dr. Jack Jicong Shi

Date Defended: July 20th, 2015

The Dissertation Committee for Gary A. Malek
certifies that this is the approved version of the following dissertation:

**Conformal Coating of Three-Dimensional Nanostructures via
Atomic Layer Deposition for Development of Advanced Energy
Storage Devices and Plasmonic Transparent Conductors**

Chairperson: Dr. Judy Wu

Date approved: July 30th, 2015

Abstract

Due to the prodigious amount of electrical energy consumed throughout the world, there exists a great demand for new and improved methods of generating electrical energy in a clean and renewable manner as well as finding more effective ways to store it. This enormous task is of great interest to scientists and engineers, and much headway is being made by utilizing three-dimensional (3D) nanostructured materials. This work explores the application of two types of 3D nanostructured materials toward fabrication of advanced electrical energy storage and conversion devices.

The first nanostructured material consists of vertically aligned carbon nanofibers. This three-dimensional structure is opaque, electrically conducting, and contains active sites along the outside of each fiber that are conducive to chemical reactions. Therefore, they make the perfect 3D conducting nanostructured substrate for advanced energy storage devices. In this work, the details for transforming vertically aligned carbon nanofiber arrays into core-shell structures via atomic layer deposition as well as into a mesoporous manganese oxide coated supercapacitor electrode are given.

Another unique type of three-dimensional nanostructured substrate is nanotextured glass, which is transparent but non-conducting. Therefore, it can be converted to a 3D transparent conductor for possible application in photovoltaics if it can be conformally coated with a conducting material. This work details that transformation as well as the addition of plasmonic gold nanoparticles to complete the transition to a 3D plasmonic transparent conductor.

Acknowledgements

Without the assistance, encouragement, and wisdom of others, I would not have been able to complete this dissertation. I am extremely thankful to so many people for helping me achieve a dream of mine. This acknowledgement section is truly too short to express my complete gratitude to everyone who has contributed to my success, but I would like to express my gratitude to a number of you.

Six years ago, Dr. Judy Wu did not know what she was taking on when she kindly agreed to be my adviser. Her endless patience, kindness, encouragement, support, and wealth of knowledge have been appreciated more than words here can express. She took a chance on a rough-around-the-research-edges, too-old-to-still-be-in-school student and has succeeded in molding me into a competent researcher. Only a person of her incredible magnitude could do so. I have learned so much from her and will always be grateful for having the opportunity to work under her guidance. Thank you Dr. Wu; you are a wonderful adviser and exceptional person.

I would also like to thank Dr. Cindy Berrie, Dr. Wai-Lun Chan, Dr. Siyuan Han, and Dr. Jack Jicong Shi for your willingness to be on my Dissertation Committee. I truly appreciate the time that you are devoting to reading though this work and being a part of my defense. Thank you all.

Many wonderful colleagues and collaborators have offered guidance and support as well. Thank you to Rongtao Lu, Alan Elliot, Jianwei Liu, Steven Klankowski, Emery Brown, Paul Harrison, Tolga Aytug, Qingfeng Liu, and Dr. Jun Li for all of your help and assistance. I truly appreciate each and every one of you.

Finally, I would like to thank my family for their love and support. To my mom and dad who have been there throughout my life - thank you for all of your support and encouragement, and for believing in me. I love you both. To my two wonderful boys - Justus and Andrew - you two are so special, and I am so thankful that I get to be your dad. Thank you for always wanting to spend time with me. Your smiles and love make every day wonderful even when I have been too busy or grumpy to let you know that. And most of all, I would like to express my appreciation to my loving wife. Amy, I love you more than words can express and am thankful for our life together. I truly appreciate all the patience you have had, and sacrifices that you have made, so I could pursue my dream. Thank you so much. I look forward to spending a lot more time with you and our boys. I love you dearly.

Publications

1. **A Novel High-Power Battery-Pseudocapacitor Hybrid Based on Fast Lithium Reactions in Silicon Anode and Titanium Dioxide Cathode Coated on Vertically Aligned Carbon Nanofibers**
Steven A. Klankowski, Gaiind P. Pandey, Gary A. Malek, Judy Wu, Ronald A. Rojas, and Jun Li, submitted to Journal of Power Sources, under review.
2. **Higher-Power Supercapacitor Electrodes Based on Mesoporous Manganese Oxide Coating on Vertically Aligned Carbon Nanofibers**
Steven A. Klankowski, Gaiind P. Pandey, Gary Malek, Conor R. Thomas, Steven L. Bernasek, Judy Wu and Jun Li, Nanoscale, 2015, 7, 8485.
3. **Plasmonic Three-Dimensional Transparent Conductor Based on Al-Doped Zinc Oxide-Coated Nanostructured Glass Using Atomic Layer Deposition**
Gary A. Malek, Tolga Aytug, Qingfeng Liu, and Judy Wu, ACS Applied Materials & Interfaces **2015**, 7 (16), 8556-61.
4. **Integrating Atomic Layer Deposition and Ultra-High Vacuum Physical Vapor Deposition for *in situ* Fabrication of Tunnel Junctions**
Alan J. Elliot, Gary A. Malek, Rongtao Lu, Siyuan Han, Haifeng Yu, Shiping Zhao, and Judy Wu, Rev. Sci. Instrum **2014**, 85 (7), 073904.
5. **Atomic layer deposition of Al-doped ZnO/Al₂O₃ double layers on vertically aligned carbon nanofiber arrays**
Gary A. Malek, Emery Brown, Steven A. Klankowski, Jianwei Liu, Alan J. Elliot, Rongtao Lu, Jun Li, and Judy Wu, ACS Applied Materials & Interfaces **2014**, 6 (9), 6865-71.
6. **Probing the Nucleation of Al₂O₃ in Atomic Layer Deposition on Aluminum for Ultrathin Tunneling Barriers in Josephson Junctions**
Alan J. Elliot, Gary Malek, Logan Wille, Rongtao Lu, Siyuan Han, Judy Z. Wu, John Talvacchio, and Rupert M. Lewis, Applied Superconductivity, IEEE Transactions on, 2013, vol.23, no.3, pp.1101405

Table of Contents

1	INTRODUCTION.....	1
1.1	MOTIVATION	1
1.2	THREE-DIMENSIONAL NANOSTRUCTURED MATERIALS.....	3
1.2.1	<i>Three-Dimensional Nanostructured Electrodes</i>	<i>5</i>
1.2.2	<i>Three-Dimensional Nanostructured Transparent Conductors</i>	<i>6</i>
1.3	OBJECTIVE OF THE PRESENT WORK.....	7
2	BACKGROUND.....	9
2.1	ATOMIC LAYER DEPOSITION	9
2.1.1	<i>Introduction to Atomic Layer Deposition</i>	<i>9</i>
2.1.2	<i>ALD Process</i>	<i>11</i>
2.1.3	<i>ALD Precursors.....</i>	<i>13</i>
2.1.4	<i>ALD Custom-Built System Design and Operation.....</i>	<i>21</i>
2.2	VERTICALLY ALIGNED CARBON NANOFIBERS ARRAYS	24
2.2.1	<i>Structure of CNFs and CNTs.....</i>	<i>24</i>
2.2.2	<i>Properties of CNFs and CNTs</i>	<i>26</i>
2.2.3	<i>Characteristics of Vertically Aligned Carbon Nanofibers</i>	<i>30</i>
2.3	PLASMONICS.....	33
2.3.1	<i>Introduction to Plasmonics</i>	<i>33</i>
2.3.2	<i>Surface Plasmon</i>	<i>34</i>
3	VERTICALLY ALIGNED CARBON NANOFIBER ARRAY EXPERIMENTS.....	41
3.1	ALD GROWTH ON VERTICALLY ALIGNED CARBON NANOFIBER ARRAYS.....	41
3.1.1	<i>Experimental Details.....</i>	<i>42</i>
3.1.2	<i>ALD Growth Confirmation</i>	<i>44</i>
3.1.3	<i>Integrity Verification of ALD Al₂O₃ Film</i>	<i>50</i>
3.1.4	<i>Hafnium Oxide Growth on VACNFs.....</i>	<i>57</i>
3.1.5	<i>Solid-State Capacitor based on a VACNF Array Core-Shell Structures</i>	<i>61</i>
3.1.6	<i>Summary and Conclusions.....</i>	<i>64</i>
3.2	MESOPOROUS MANGANESE OXIDE COATING OF VERTICALLY ALIGNED CARBON NANOFIBERS FOR A HIGHER-POWER SUPERCAPACITOR ELECTRODE.....	64
3.2.1	<i>Experimental Details.....</i>	<i>67</i>
3.2.2	<i>Structural Characterization of MnO₂-VACNF Array Electrodes.....</i>	<i>68</i>
3.2.3	<i>Electrochemical Performance of MnO₂-VACNF Array Electrodes</i>	<i>71</i>
3.2.4	<i>Summary and Conclusions.....</i>	<i>77</i>
3.3	HIGH POWER BATTERY-PSEUDOCAPACITOR HYBRID	78
3.3.1	<i>Experimental Details.....</i>	<i>82</i>
3.3.2	<i>Results and Discussion</i>	<i>83</i>
3.3.3	<i>Summary and Conclusions.....</i>	<i>90</i>
4	PLASMONIC THREE-DIMENSIONAL TRANSPARENT CONDUCTOR.....	92
4.1	EXPERIMENTAL DETAILS.....	94
4.1.1	<i>Fabrication of Nanostructured Glass</i>	<i>94</i>
4.1.2	<i>ALD AZO Growth.....</i>	<i>96</i>
4.1.3	<i>Deposition of Gold Nanoparticles</i>	<i>97</i>
4.1.4	<i>Characterization Equipment</i>	<i>97</i>
4.2	RESULTS AND DISCUSSION	98
4.2.1	<i>Schematic and Scanning Electron Microscope Images</i>	<i>98</i>
4.2.2	<i>Transmittance Measurements.....</i>	<i>102</i>

4.2.3	<i>Conductivity Measurements</i>	104
4.3	SUMMARY AND CONCLUSIONS	107
5	OVERALL CONCLUSIONS	109

Table of Figures

FIGURE 1.1 THE NATIONAL RENEWABLE ENERGY LABORATORY'S CHART OF THE HIGHEST CONFIRMED CONVERSION EFFICIENCIES FOR RESEARCH CELLS, FROM 1976 TO THE PRESENT, FOR VARIOUS PHOTOVOLTAIC TECHNOLOGIES.	2
FIGURE 2.1 ALD TEMPERATURE WINDOW	13
FIGURE 2.2 PHYSICAL PROPERTIES OF TMA ALONG WITH A VAPOR PRESSURE VS. TEMPERATURE GRAPH.	16
FIGURE 2.3 KEY SHOWING THE ELEMENTS AND MOLECULES USED IN THE FOLLOWING FIGURES FOR THE GROWTH OF Al_2O_3 .	17
FIGURE 2.4 PHYSICAL PROPERTIES OF DEZ ALONG WITH A VAPOR PRESSURE VS. TEMPERATURE GRAPH.	19
FIGURE 2.5 PHYSICAL PROPERTIES OF TEMA H ALONG WITH A VAPOR PRESSURE VS. TEMPERATURE GRAPH.	20
FIGURE 2.6 DESIGN OF CUSTOM-BUILT ALD SYSTEM	22
FIGURE 2.7 SCHEMATICS OF A (A) SINGLE SHEET OF GRAPHENE, (B) CARBON NANOTUBE, AND (C) CARBON NANOFIBER WITH STACKED GRAPHITIC CONES.	25
FIGURE 2.8 TRANSMISSION ELECTRON MICROSCOPE IMAGES SHOWING THE DIFFERENT STRUCTURES OF A (A) HERRINGBONE CNF AND A (B) BAMBOO CNF.	26
FIGURE 2.9 (A) IMAGE OF A 20 NM DIAMETER CNF NEAR THE METAL CONTACT BASE SHOWING THE LAYERING OF GRAPHENE SHEETS ALMOST PERPENDICULAR TO THE AXIS OF THE CNF. (B) TEM IMAGE OF CNF SHOWING ANGLE α BETWEEN CNF AXIS AND BASAL PLANE OF GRAPHENE CONE. (C) GRAPH SHOWING HOW THE ANGLE α CHANGES WITH DISTANCE TO THE CNF BASE.	27
FIGURE 2.10 SEM IMAGE OF AN AS-GROWN VERTICALLY ALIGNED CARBON.	30
FIGURE 2.11 DRAWING TO SHOW HOW THE CURRENT FLOW THROUGH A CNF CROSSES GRAPHITIC PLANE BOUNDARIES.	32
FIGURE 2.12 A DIAGRAM SHOWING SURFACE PLASMON POLARITONS PROPAGATING ALONG THE X-DIRECTION AND DECAYING EVANESCENTLY IN THE Z-DIRECTION.	34
FIGURE 2.13 A GRAPH OF THE DISPERSION RELATION FOR SURFACE PLASMONS.	36
FIGURE 2.14 DIAGRAM SHOWING LOCALIZED SURFACE PLASMONS.	37
FIGURE 2.15 SEM IMAGES OF 12 NM NOMINAL THICKNESS AUNPs ON (A) NANOLINE PATTERNED FTO AND (B) NANOPILLAR PATTERNED FTO.	38
FIGURE 2.16 COMPUTER SIMULATION OF THE POWER DISTRIBUTION FOR AN INCIDENT GAUSSIAN BEAM PASSING ACROSS (A) A PATTERNED FTO STRUCTURE WITHOUT AUNPs AND (B) THE SAME PATTERNED FTO STRUCTURE WITH AUNPs.	39
FIGURE 2.17 TRANSMITTANCE VS. WAVELENGTH GRAPH REVEALING THE LSPR EFFECT (DIP IN THE GRAPH) FOR AUNPs APPLIED TO A PLANAR FTO (RED), NANOLINE PATTERNED FTO (BLUE), AND NANOPILLAR FTO (PURPLE) SUBSTRATES.	39
FIGURE 2.18 SURFACE MORPHOLOGIES OF <i>IN-SITU</i> FABRICATED AUNPs ON SiO_2/Si [(A)-(D)] AND CVD GRAPHENE [(E)-(H)] WITH DIFFERENT NOMINAL AU THICKNESSES OF: 2NM [(A) AND (E)], 4 NM [(B) AND (F)], 8 NM [(C) AND (G)], AND 12 NM [(D) AND (H)]. THE SCALE BAR IS 100 NM.	40
FIGURE 2.19 OPTICAL TRANSMITTANCE SPECTRA OF AUNP/GLASS (SOLID CURVES) AND AUNP/GRAPHENE/GLASS (DASHED CURVES) CLEARLY INDICATING A REDSHIFT IN THE LSPR WAVELENGTH WITH THE ADDITION OF THE GRAPHENE LAYER.	40
FIGURE 3.1 SCHEMATIC DEMONSTRATING ONE COMPLETE Al_2O_3 ALD CYCLE ALONG THE SIDEWALL OF A VACNF.	42
FIGURE 3.2 FESEM IMAGES OF VACNF ARRAYS. (A) SIDE VIEW AND (B) 45° PERSPECTIVE VIEW OF THE AS-GROWN VACNF ARRAY WITH THE Ni CATALYST SLIGHTLY VISIBLE. (C) SIDE VIEW AND (D) 45° PERSPECTIVE OF AN Al_2O_3 /AZO COATED VACNF ARRAY WITH THE Ni TIP CLEARLY COATED OVER.	45
FIGURE 3.3 TEM IMAGES OF (A) CONFORMAL Al_2O_3 COATING ALONG A CNF INCLUDING THE Ni CATALYST TIP. (B) CONFORMAL Al_2O_3 COATING CONTINUES DOWN THE SHAFT OF THE CNF UNTIL WHERE IT IS BROKEN OFF FROM THE BASE. (C) CONFORMAL Al_2O_3 COATING ALONG ANOTHER CNF WHICH ALSO SHOWS THE “HERRINGBONE” NATURE OF THE CNF. (D) CLOSE-UP OF THE CONFORMAL COATING AROUND THE Ni TIP. (E) EXTREME CLOSE-UP IMAGE OF CNF CORE AND Al_2O_3 SHELL.	47
FIGURE 3.4 (A) Al_2O_3 COATED CNF BEFORE ANNEALING. (B) NO DIFFRACTION PATTERN IS PRESENT BEFORE ANNEALING. (C) Al_2O_3 COATED CNF AFTER ANNEALING. (D) APPARENT DIFFRACTION PATTERN IS PRESENT AFTER ANNEALING.	48

FIGURE 3.5 HRTEM IMAGES OF (A) $\text{Al}_2\text{O}_3/\text{AZO}$ CONFORMAL CORE-SHELL COATING OF CNFs AND (B) CLOSE-UP OF $\text{Ni}/\text{Al}_2\text{O}_3/\text{AZO}$ LAYERING. (C) FESEM IMAGE SHOWING CNF GRAPHITIC CONE AS WELL AS THE ALD CORE-SHELL COATING.	49
FIGURE 3.6 EDX ELEMENTAL ANALYSIS. (A) HRTEM IMAGE OF AN Al_2O_3 COATED CNF WITH THE BLUE SCAN REGION SHOWN. (B) ELEMENTAL COUNT VS. POSITION GRAPH REVEALING THE ELEMENTS ALUMINUM, OXYGEN, AND CARBON.	49
FIGURE 3.7 ELECTRICAL CHARACTERIZATION OF A PLANAR CAPACITOR. (A) I-V CURVES MEASURED BY CYCLING THE BIAS VOLTAGE BETWEEN -0.1 TO +0.1 V AT THE RATES OF 100, 500, AND 1000 V/S, RESPECTIVELY. (B) THE AREA-SPECIFIC CAPACITANCE VS. THE SCAN RATE DERIVED FROM THE CYCLING I-V MEASUREMENTS. (C) GALVANOSTATIC CHARGE-DISCHARGE CURVE AT A CONSTANT CURRENT DENSITY OF 12.5 mA/cm ² . (D) THE AREA-SPECIFIC CAPACITANCE VS. CURRENT DENSITY CALCULATED FROM CHARGE-DISCHARGE CURVES.....	53
FIGURE 3.8 A NYQUIST PLOT ON THE COMPLEX PLANE. THE EXPRESSION FOR THE IMPEDANCE Z (BLUE ARROW) IS COMPOSED OF A REAL PART AND AN IMAGINARY PART. THE DIRECTION OF INCREASING FREQUENCY IS COUNTERCLOCKWISE.....	54
FIGURE 3.9 DIAGRAM OF A RANGLES CIRCUIT WITH THE LEAKING CURRENT RESISTANCE IN PARALLEL WITH THE CAPACITANCE AND BOTH IN PARALLEL WITH THE SERIES RESISTANCE.	55
FIGURE 3.10 THE VIOLET DIAMONDS REPRESENT THE DATA POINTS OF A NYQUIST PLOT FOR THE AC IMPEDANCE SPECTRUM OF THE 2 MM X 2 MM PLANAR CAPACITOR, AND THE BLACK FITTED CURVE REPRESENTS THE ASSOCIATED RANGLES CIRCUIT. THE AC FREQUENCY WAS VARIED FROM 100 kHz TO 10 MHz AND THE AMPLITUDE WAS FIXED AT 5 mV. THE FITTED SERIES RESISTANCE (R_s) AND LEAKING CURRENT RESISTANCE (R_L) WERE 94 Ω AND 7.5 M Ω , RESPECTIVELY, AND THE CAPACITANCE WAS 1.64 x 10 ⁻⁸ F (I.E. 0.41 mF/cm ²).	56
FIGURE 3.11 TEM IMAGES CONFIRMING NON-UNIFORM HfO_2 GROWTH ON CNFs. IMAGE (A) SHOWS THE ENTIRE LENGTH OF THE CNF DOWN TO WHERE IT BROKE OFF OF AT THE BASE. IMAGES (B), (C), AND (D) ARE ALL MAGNIFIED IMAGES OF (A) WITH IMAGE (B) ALSO REVEALING THE EDX LINE SCAN REGION (BLUE LINE).	57
FIGURE 3.12 EDX ELEMENTAL COUNT VS. POSITION GRAPH REVEALING THE ELEMENTS HAFNIUM, OXYGEN, AND CARBON. THE LINE SCAN REGION IS SHOWN IN FIGURE 3.11B.	58
FIGURE 3.13 FULL TEM IMAGE OF CNF REVEALING POSSIBLE CVD HfO_2 GROWTH DOWN THE ENTIRE SHAFT UNTIL WHERE IT BROKE OFF AT THE BASE. THE GRAPHITIC CONE OF THE CNF IS CLEARLY VISIBLE ON THE RIGHT-HAND SIDE WITH SOME ADDITIONAL GRAPHITIC CONES REVEALING THEMSELVES ON THE LEFT-HAND SIDE NEAR THE NICKEL TIP.	59
FIGURE 3.14 TEM IMAGES OF CVD HfO_2 COATED CNFs. IMAGES (A) & (B) DID NOT HAVE AN Al_2O_3 NUCLEATION LAYER WHILE IMAGES (C) & (D) UTILIZED A 1-nm Al_2O_3 NUCLEATION LAYER. IMAGES (A) AND (C) CLEARLY REVEAL THE GRAPHITIC CNF CONES AND IMAGES (B) & (D) REVEAL THE NON-UNIFORM HfO_2 GROWTH.	60
FIGURE 3.15 SCHEMATIC SHOWING AN AZO (GREEN) COATED VACNF ARRAY (BLACK) FOR USE AS A CAPACITOR. THE ENLARGED CYLINDER DETAILS THE OUTER RADIUS A , INNER RADIUS B , AND LENGTH L OF A CYLINDRICAL CAPACITOR. NOTE THAT A DIELECTRIC MEDIUM WAS NOT CHOSEN, BUT ALD Al_2O_3 OR HfO_2 COULD BE USED.	62
FIGURE 3.16 SCHEMATIC OF Mn-COATED VACNFs (A) BEFORE AND (B) AFTER ELECTROCHEMICAL OXIDATION IN 1 M Na_2SO_4 . REPRESENTATIVE SEM IMAGES OF 300 NM NOMINAL Mn THICKNESS AT DIFFERENT MAGNIFICATIONS WITH (C) & (E) BEFORE OXIDATION AND (D) & (F) AFTER OXIDATION.	69
FIGURE 3.17 SEM AND TEM OF THE Mn-COATED VACNFs AFTER Mn SPUTTERING TO VARIOUS NOMINAL THICKNESSES OF 100, 300, AND 600 NM. SCALE BARS ARE 100 NM, 1.0 μm , 300 NM; 200 NM, 1.0 μm , 300 NM; 200 NM, 1.0 μm 500 NM, FOR THE 100 NM, 300 NM AND 600 NM SAMPLES, RESPECTIVELY.	70
FIGURE 3.18 SEM AND TEM IMAGES OF THE MnOx-COATED VACNFs AFTER OXIDATION AND CYCLING CHARACTERIZATION. THE IMAGES ARE SHOWN WITH RESPECT TO THEIR VARIOUS NOMINAL THICKNESSES OF 100, 300, AND 600 NM. SCALE BARS ARE 500 NM IN PANELS (A), (E) AND (I); 1.0 μm IN PANELS (B), (F) AND (J); 2.0 μm FOR PANELS (C), (G) AND (K); AND 300 NM IN PANELS (D), (H) AND (L), RESPECTIVELY, FOR EACH THICKNESS.....	71
FIGURE 3.19 I-V CURVES BY CYCLIC VOLTAMMETRY FOR Mn-COATED VACNF ELECTRODES WITH NOMINAL THICKNESSES OF 100, 200, 300, AND 600 NM, PERFORMED AT THE SCAN RATES OF (A) 1 mV/s, (B) 10 mV/s, (C) 100 mV/s, AND (D) 1000 mV/s. (E) THE SPECIFIC CAPACITY VERSUS THE SCAN RATE FOR VARIOUS NOMINAL THICKNESSES. THE CURVE LABELED AS “50 NM PLANAR” IS MEASURED WITH A CONTROL SAMPLE OF 50 NM THICK PLANAR Mn FILM DEPOSITED ON A FLAT Cr-COATED Si WAFER.	72
FIGURE 3.20 NYQUIST PLOT FROM IMPEDANCE SPECTROSCOPIC ANALYSIS OF THE MnO ₂ -COATED VACNFs WITH THE INSET SHOWING THE FULL REGION.	73

FIGURE 3.21 CHRONOPOTENTIOMETRIC CYCLING PROFILES OF MN-COATED VACNF ELECTRODE WITH (A) 300 NM NOMINAL THICKNESS AT 0.28 A/G, 2.78 A/G, AND 27.8 A/G AND (B) COMPARISON OF VARIED NOMINAL THICKNESS OF 100, 200, 300, AND 600 NM AT 2.78 A/G. (C) LOG-LOG CURVE OF SPECIFIC CAPACITANCE VERSUS SPECIFIC CURRENT RATE FOR VARIOUS NOMINAL THICKNESSES.	74
FIGURE 3.22 RAGONE PLOTS OF MN-COATED VACNF ELECTRODES (A) AT THE NOMINAL MN THICKNESSES OF 100, 200, 300, AND 600 NM; AND (B) AT 100 NM NOMINAL MN THICKNESS (RED DIAMONDS) WITH COMPARISONS TO VALUES ACHIEVED IN PREVIOUS WORK (BLACK SQUARES), AND THE RANGE SEEN FOR COMMERCIAL & STATE-OF-ART SUPERCAPACITORS AS WELL AS LITHIUM BATTERIES. THE BLACK DASHED LINE REPRESENTS A TARGET IN SPECIFIC POWER PROPOSED BY PARTNERSHIP FOR A NEW GENERATION OF VEHICLES (PNGV).....	76
FIGURE 3.23 (A) ILLUSTRATION OF THE FULL CELL CONSISTING OF A PRELITHIATED ANODE MADE OF SI-COATED VACNFs AND A CATHODE MADE OF TiO ₂ -COATED VACNFs, BOTH GROWN ON CUPPER FOILS. THE EXPECTED OPERATING POTENTIALS OF EACH ELECTRODE DURING CYCLING ARE SHOWN TO THE LEFT, WITH ARROWS POINTING THE DIRECTION OF POTENTIAL CHANGE OF INDIVIDUAL ELECTRODES DURING DISCHARGE. THE STRUCTURES OF THE AS-PREPARED ELECTRODE MATERIALS AT VARIOUS SCALES ARE REVEALED BY SEM AND TEM IMAGES IN (B-D) FOR TiO ₂ -COATED VACNFs AND (E-G) FOR SI-COATED VACNFs.	79
FIGURE 3.24 (A) THE VOLTAGE PROFILE OF THE SI-TiO ₂ FULL-CELL AT 90 mA IN COMPARISON WITH THE HALF-CELLS OF TiO ₂ -VACNF AND SI-VACNF ELECTRODES. (B) THE PERFORMANCE OF THE SI-TiO ₂ FULL-CELL DURING CHARGE-DISCHARGE CYCLING BETWEEN 2.2 V AND 0.6 V AS THE CURRENT WAS STEPWISE INCREASED FROM 45 mA TO 4,500 mA, SHOWING CHARGE (BLUE SQUARES) AND DISCHARGE (GREEN SQUARES) CAPACITIES (LEFT VERTICAL AXIS) AND COULOMBIC EFFICIENCY (ORANGE DIAMONDS) (RIGHT VERTICAL AXIS). (C) THE CORRESPONDING CHARGE-DISCHARGE VOLTAGE PROFILES OF THE SI-TiO ₂ FULL-CELL AT VARIOUS CURRENTS.	85
FIGURE 3.25 NYQUIST PLOT OF THE ELECTROCHEMICAL IMPEDANCE SPECTRA (EIS) OF THE SI-TiO ₂ FULL-CELL AFTER GOING THROUGH 400 CHARGE-CHARGE CYCLES. EACH SPECTRUM WAS MEASURED AT A STATIC VOLTAGE VARIED FROM 0.6 V TO 2.2 V USING A CHI 760D POTENTIOSTAT (CH INSTRUMENTS, AUSTIN, TX) WITH A 5 mV AC VOLTAGE OVER A FREQUENCY RANGE FROM 100 kHz TO 0.01 Hz. THE INSET IS AN EXPANDED VIEW OF THE SPECTRA.	87
FIGURE 3.26 (A) THE SPECIFIC CAPACITY OF THE SI-TiO ₂ FULL-CELL VERSUS APPLIED CURRENT. (B) RAGONE PLOT OF THE SI-TiO ₂ FULL CELL OPERATED AT VARIOUS CURRENTS. THE SPECIFIC ENERGY AND SPECIFIC POWER ARE CALCULATED USING EQ. (1) AND (2), RESPECTIVELY.....	89
FIGURE 3.27 THE MAXIMUM POWER DENSITY CALCULATED BY EQ. (4) VERSUS THE SPECIFIC ENERGY CALCULATED BY EQ. (2).	90
FIGURE 4.1 (A) TOP DOWN VIEW OF THE SPINODALLY PHASE-SEPARATED NANOSTRUCTURED GLASS WHICH REVEALS A CORAL-LIKE NATURE. (B) SIDE VIEW OF THE NANOSTRUCTURED GLASS COATING SHOWING A THICKNESS OF APPROXIMATELY 200 NM.	95
FIGURE 4.2 CROSS-SECTIONAL SCHEMATICS REPRESENTING THE (A) POROUS UNCOATED NANOSTRUCTURED GLASS (IN BLUE) AND (B) COATED NANOSTRUCTURED GLASS WITH AZO (IN GREEN) AND AuNPs (IN GOLD).	98
FIGURE 4.3 FESEM IMAGES OF NANOSTRUCTURED GLASS. (A) UNCOATED QUARTZ, (B) & (C) QUARTZ WITH 47 NM AZO AT DIFFERENT MAGNIFICATIONS, AND (D) BOROSILICATE WITH 27 NM AZO AND 8 NM AuNPs.	99
FIGURE 4.4 AFM IMAGES OF THE (A) UNCOATED NANOSTRUCTURED GLASS AND (B) NANOSTRUCTURED GLASS COATED WITH 47 NM AZO AND 8 NM AuNPs. THE HEIGHT PROFILES WERE TAKEN ALONG THE BLUE LINE SHOWN ON THE AFM IMAGES. THESE PROFILES REVEAL THE ROUGH NATURE OF THE SUBSTRATE SURFACES..	101
FIGURE 4.5 (A) PHOTOGRAPH SHOWING TRANSPARENCY OF UNCOATED NANOSTRUCTURED GLASS ON THE LEFT AND NANOSTRUCTURED GLASS WITH 27 NM AZO COATING ON THE RIGHT. (B) TRANSMITTANCE VS. WAVELENGTH SPECTRA FOR THE 17, 27, 37, AND 47 NM THICK AZO COATINGS. DATA FOR THE 47 NM AZO SAMPLE WITH 8 NM AuNPs IS ALSO SHOWN, CLEARLY REVEALING THE LSPR WAVELENGTH OF 728 NM AND THE CORRESPONDING MINIMUM TRANSMITTANCE OF 25.7%.....	102
FIGURE 4.6 FESEM IMAGE OF AuNP COATED NANOSTRUCTURED GLASS. THE REDUCED TRANSPARENCY PROVIDED BY THE AuNP COATED NANOSTRUCTURED GLASS IS REVEALED IN THE INSET.....	104
FIGURE 4.7 VOLTAGE VS. CURRENT CURVES DISPLAYING THE OHMIC NATURE OF THE TRANSPARENT CONDUCTORS DEPOSITED ON NANOTEXTURED GLASS SUBSTRATES. RESISTANCE VALUES OBTAINED FOR EACH SAMPLE ARE DISPLAYED IN THE FIGURE.	105
FIGURE 4.8 TRANSMITTANCE AT 550 NM VERSUS SHEET RESISTANCE FOR DIFFERENT THICKNESSES OF AZO FILMS AND AuNPs DEPOSITED ON THE NANOSTRUCTURED GLASS SUBSTRATES. THE TRANSMITTANCE ERROR BARS	

REPRESENT ONE STANDARD DEVIATION AND THE SHEET RESISTANCE ERROR BARS ARE NOT SHOWN DUE TO NEGLECTIBLE SIZE	107
---	-----

1 Introduction

1.1 Motivation

The International Energy Agency (IEA) and the United States Energy Information Administration (EIA) publish yearly reports documenting the world's energy usage that include past production and consumption in addition to predictions for future energy demand.¹⁻² A large portion of the energy produced and consumed is in the form of electrical energy. The EIA website (eia.gov) reveals that the world consumed $\sim 13 \times 10^{12}$ kWh of electrical energy in the year 2000 and, that by the year 2012, the total consumption increased by 54% to $\sim 20 \times 10^{12}$ kWh. Since global electrical energy consumption displays continual growth according to their data, both entities predict that world electrical energy production and consumption will continue to rise as one would expect.

Much of the electrical energy throughout the world is generated by non-renewable sources (e.g., fossil fuels and nuclear) that produce unwanted byproducts, which are harmful to the environment. Therefore, in order to accommodate the ever-increasing electrical energy demand that contributes so much pollution to the world, new ideas for clean and renewable sources of electrical energy conversion need to be developed and existing technologies (e.g., solar, wind, hydroelectric, etc.) need to be improved upon.

The theoretical power received at the surface of the earth due to the sun is approximately 89×10^{12} kW,³⁻⁵ which equates to 89×10^{12} kWh of energy arriving in one hour. Therefore, in approximately ten minutes the earth receives enough energy from the sun to meet the global electrical energy consumed worldwide for one year ($\sim 20 \times 10^{12}$ kWh).¹⁻² Unfortunately, solar energy conversion only accounted for $\sim 1\%$ of the world's electricity generation in 2014 according to the IEA Photovoltaic Power Systems Programme.⁶ This represents a vast

improvement from just ten years ago, but there is still much room for growth. Therefore, harvesting more clean and renewable solar energy would help make a huge impact toward alleviating the problem of consuming non-renewable sources which are mainly used to meet the global energy demand according to the EIA website.

As shown in Figure 1.1,⁷ many public and private research entities over the past forty years have contributed to the development of new photovoltaic devices as well as toward improving the conversion efficiencies of already developed solar cells. However, the record efficiencies achieved are still far below the theoretical maximum blackbody efficiency of a solar cell which is 85.4% under direct sunlight.⁸ Therefore, since the present record efficiencies of the research cells shown in the figure are well below this value, additional advances can and need to be made in order to increase the overall production of clean and renewable electrical energy from photovoltaics.

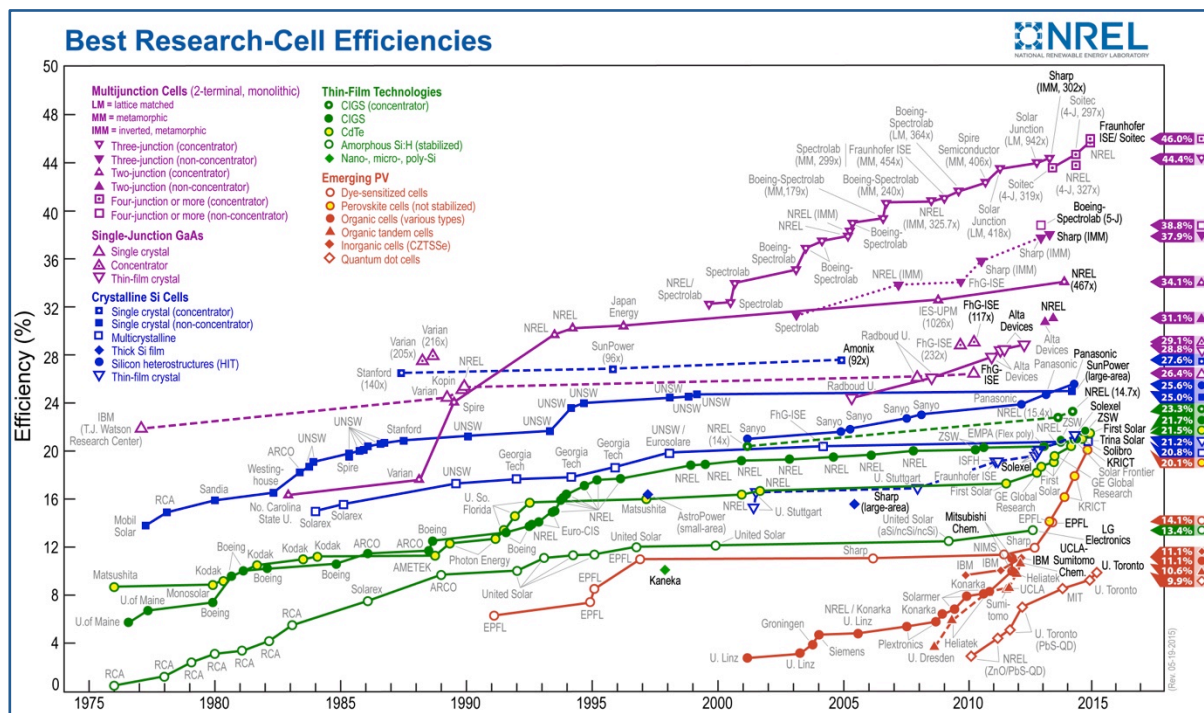


Figure 1.1 The National Renewable Energy Laboratory's chart of the highest confirmed conversion efficiencies for research cells, from 1976 to the present, for various photovoltaic technologies.

Not only does society have a need for clean, renewable sources of electrical energy conversion, but improved electrical energy storage units are also in great demand. An obvious detriment to the advancement of photovoltaic usage is that it does not generate electrical energy during the absence of sunlight. Utilizing an energy storage device, which is able to work in conjunction with solar cells for storing unused energy generated during maximum sunlight exposure, is extremely beneficial. In addition, electric or hybrid motives of transportation are continuing to improve and become more prominent in order to replace traditional fossil fuel based vehicles. Therefore, improvements in their energy storage systems will only help this advancement and decrease the world's dependence on nonrenewable, pollution producing fossil fuels. Furthermore, since portable electrical devices have become commonplace due to the miniaturization of transistors and other electrical components, there is an ever-increasing demand for improved energy storage systems that are compact and lightweight.

In summary, due to the prodigious amount of electrical energy consumed throughout the world, there exists a great demand for new and improved methods of generating electrical energy in a clean and renewable manner as well as finding more effective ways to store it. This enormous task is of great interest to scientists and engineers and much headway is being made. Hence, my interests in the advancements being made toward clean and renewable photovoltaic devices, as well as the improvements in energy storage systems were the catalyst behind this work.

1.2 Three-Dimensional Nanostructured Materials

Much progress has been made toward improving existing photovoltaic technology and electrical energy storage devices by utilizing nanostructured materials as mentioned in a number of review

articles.⁹⁻¹⁶ Because of the overwhelming potential for nanostructured materials to continue to provide solutions to energy-based issues, this work employed two unique three-dimensional (3D) nanostructured substrates coated with nanometer thick functional materials.

Utilizing 3D nanostructured substrates as opposed to traditional two-dimensional (2D) structured substrates leads to an increase in the overall surface-to-volume ratio. This is beneficial because it is at the surface where all relevant interactions between active materials take place. Therefore, if the total surface area is increased while simultaneously decreasing the volume, there will be less overall mass and a larger area for the functional materials while still maintaining the compact size of the traditional 2D structure. Furthermore, coating these 3D nanostructured surfaces with thin-film mediums on the order of nanometers thick can be extremely beneficial in device application. This is because many of the relevant functionalities between active materials for electrical energy storage or conversion benefit from shorter distances (e.g., diffusion lengths, diffusion rates, electron conduction, hole conduction, photon absorption, interfacial charge transfer, etc.).

The use of 3D nanostructured conducting materials as electrodes for batteries, capacitors, and photovoltaic devices is not a new concept. According to the aforementioned review articles, as well as some other references, there are numerous 3D nanostructured forms that can be utilized. Some are of an ordered or periodic nature usually with a high aspect ratio (e.g., vertically aligned carbon nanotubes,¹⁷ vertically aligned carbon nanofibers,¹⁸ anodized aluminum oxide nanopores,¹⁹ etc.) while others have a more randomly orientated or porous nature (e.g., nanoporous glass,²⁰ activated carbons, carbon nanofoam,²¹ etc.). Despite the differences in design, all of the 3D nanostructured materials are engineered to improve the performance of some device in application by providing an increase in total surface area with the potential to

support nanometer thick thin-film functional materials. The next two sections provide a few examples as to how 3D nanostructured electrodes and 3D nanostructured transparent conductors have been employed in order to improve the performance of electrical energy storage or conversion devices.

1.2.1 Three-Dimensional Nanostructured Electrodes

Lithium-ion batteries represent a large portion of commercially produced batteries and the market for them continues to grow.²² They are lightweight, have a large energy density, and provide an acceptable cycling life. Due to these advantages and their successful application, continued research has been focused on improving them.

The use of nanomaterials for the cathode or anode of a lithium-ion battery has received some of this focus due to the potential benefits. Patil *et al.* list the following as possible advantages toward using nanomaterials in a lithium-ion battery.²³

1. A better accommodation of the strain during lithium insertion/removal which improves cycling life.
2. New reactions that would not be the same with the use of a bulk material.
3. Larger electrode surface area leading to more contact area with the electrolyte material and, hence, higher charge/discharge rates.
4. Shorter path lengths for charge/lithium ion transport.

These advantages, along with some disadvantages that are not listed, have provided the impetus behind the research toward new and improved nanostructured materials that can lead to the next generation lithium-ion battery.

Capacitor advancements have also benefited from utilizing 3D nanostructures. For example, 3D carbon-based nanostructures have been utilized as electrode materials in electrochemical capacitors to increase their power density, decrease the charge-discharge rate, and improve cycling life.¹² Many of these 3D carbon-based nanostructures utilize activated carbons, but Pint *et al.* demonstrated a solid-state supercapacitor based on aligned single-walled carbon nanotube arrays.¹⁷ However, not all 3D nanostructured capacitors incorporate carbon-based nanomaterials. Banerjee *et al.* fabricated metal-insulator-metal capacitors inside of anodized aluminum oxide nanopores.¹⁹ Both of these 3D nanostructured designs for solid-state capacitors demonstrated improved performance over previously published results.

The benefits toward the application of 3D nanostructured materials as conducting electrodes for the advancement of energy storage devices are extensive. These few examples and cited works are only meant to validate the need for continued research with 3D nanostructured materials based upon the present progress that has been made.

1.2.2 Three-Dimensional Nanostructured Transparent Conductors

Transparent conductors (TCs) are a fundamental component for any electrical device that requires an electrically conducting surface that is also optically transparent. They are used for touchscreens, organic light-emitting diodes, liquid-crystal displays, and many types of solar cells (e.g., dye-sensitized, perovskite, cadmium telluride, etc.). Because these applications are in great demand, research to improve the performance of TCs and reduce their cost is of much interest.²⁴

The majority of these applications only require the TC to be a 2D surface, but solar cells may benefit the most from a nanostructured 3D design. One of the most common solar cells to utilize a nanostructured surface is the dye-sensitized solar cell (DSSC) first proposed by Dr.

Michael Grätzel.²⁵ In the original design, the 3D nanostructured material consists of a thin film of titanium dioxide (TiO₂) nanoparticles coated with a charge-transfer dye to sensitize the nanoparticles for light harvesting. By utilizing TiO₂ nanoparticles the surface area for absorption of the dye-sensitizer is maximized which optimizes light harvesting. In addition, the increased surface area also provides additional dye-sensitizer/redox electrolyte contact area. Many different designs of the DSSC have followed in an attempt to improve the conversion efficiency,²⁶⁻²⁷ but all of them still incorporate some form of nanostructured material in order to harvest the energy in sunlight and convert it to an electrical form.

There are other applications for 3D nanostructured TCs (e.g., capacitors²⁸), but so far the research conducted and applications for 3D nanostructured transparent conductors does not seem as extensive as that for 3D nanostructured electrodes. Nonetheless, they still have the potential to contribute to the improved performance of solar cells. These few examples given and works cited are only meant to provide evidence of the continued need for research in this area as well.

1.3 Objective of the Present Work

The goal of this work is to utilize two unique 3D nanostructures - vertically aligned carbon nanofiber (VACNF) arrays and nanostructured glass - toward the development of advanced energy storage electrodes and a plasmonic transparent conductor. The VACNF array is an opaque, conducting substrate that has already been researched extensively as an electrode material for numerous applications, while the nanostructured glass is a transparent, non-conducting substrate that is relatively new but can be utilized as the foundation for a 3D transparent conductor.

In order to maximize the surface area provided by either 3D nanostructure, the whole surface must be conformally coated with a functional material. Therefore, a method that is capable of conformally coating the high aspect ratio or porous nanostructures with a functional material had to be utilized. Unfortunately, these 3D nanostructures are difficult to conformally coat because the high aspect ratio VACNFs and the porous, coral-like glass produce unwanted shadowing effects. Furthermore, many traditional deposition techniques utilize a line-of-sight method that varies the thin film thickness as distance increases from the central deposition point. In order to overcome these obstacles, the gas-phase technique atomic layer deposition (ALD) was utilized since gases can penetrate into the crevasses of the 3D nanostructures to provide a layer-by-layer growth that is conformal throughout the surface.

In this work, the process for ALD conformal coating of vertically aligned carbon nanofiber (VACNF) arrays and nanotextured glass is detailed and the growth of the ALD films is verified. The periodic array of VACNFs provided a conducting substrate, that when conformally coated, produced core-shell structures that could potentially be transformed into a solid-state supercapacitor. The nanotextured glass is a highly porous coral-like structure, that when conformally coated, could potentially be utilized as a 3D nanostructured transparent conductor. In addition, the conducting nanotextured glass was coated with nanoparticles in order to provide a plasmonic effect for improved light harvesting. Both of these coated 3D nanostructured substrates could lead toward the development of new and improved electrical energy conversion devices and/or storage technology. The experimental accomplishments and potential creative applications are discussed in this work.

2 Background

Nanotechnology fabrication techniques cover a wide range of possibilities with each technique having a unique benefit or potential limitation toward application. When choosing which fabrication technique is best for a particular project, an understanding of the advantages and limitations must be well understood. In this chapter, background information on the main fabrication technique chosen for this work, ALD, is described in detail. Following the thorough discussion of ALD, an overview of the properties and characteristics of vertically aligned carbon nanofibers (VACNFs) will be covered. This discussion provides the motivation for the utilization of VACNF arrays as one of the three-dimensional nanostructured substrates used for this work. To conclude this chapter on background information, the basic physics of plasmonic nanoparticles is discussed with a focus on the benefits of gold nanoparticles, results obtained from other group member's published research utilizing gold nanoparticles, and the motivation behind their use for this work.

2.1 Atomic Layer Deposition

2.1.1 Introduction to Atomic Layer Deposition

Despite many books and publications stating when ALD was first proposed or demonstrated it is fairly clear that the answers to those questions depend on the source. A website launched in April 2013, named ALD Pulse (aldpulse.com), is currently working on a virtual project called the "History of ALD" in order to determine the original founder or founders. Even though there are small discrepancies as to who should be given credit for first inventing ALD, most seem to recognize that the first mention of a similar concept called "molecular layering" was provided by Prof. Valentin Borisovich Alexkovskil in his Ph.D. thesis published in 1952 in Russia, and the

first invention and patent application on “atomic layer epitaxy” (ALE) was submitted by Dr. Tuomo Suntola in 1974 in Finland.²⁹ Since ALD can grow epitaxial films, but does not necessarily have to, the scientific community has now adopted the term “deposition” instead of “epitaxy” as was originally termed by Dr. Suntola.

Even though ALD originated more than 40 years ago, rapid growth in the technology has occurred over the past 20 years.³⁰⁻³¹ This progress is mainly due to the semiconductor industry’s interest in growing extremely thin, high-k dielectrics with exceptional quality, which ALD is able to achieve. A drastic increase in the number of publications involving ALD has paralleled the industrial growth. Table 2.1 shows the search results of the database Web of Science for the number of publications that include in the title “atomic layer deposition.” An additional column is given that includes “atomic layer deposition” or “atomic layer epitaxy” in the title. The first occurrence of the words “atomic layer epitaxy” in a publication title was by V. P. Tanninen *et al.* in 1981.³² The first occurrence of the words “atomic layer deposition” in a publication title was by B. W. Sanders et al. in 1992.³³

1981 to	ALD only	ALD or ALE
1995	9	402
2000	69	620
2005	560	1170
2010	1569	2209
June 2015	3336	3993

Table 2.1 The number of publications using “atomic layer deposition” and/or “atomic layer epitaxy” since 1981 as provided by Web of Science.

2.1.2 ALD Process

ALD is similar to chemical vapor deposition (CVD), which has been used since the 1920s. But, despite the similarities to CVD, ALD has unique characteristics and advantages that define it as a valuable technique in its own right.³⁴⁻³⁵ Both deposition techniques use at least two gas-phase precursors for a chemical reaction to occur on the surface of a heated substrate, but in ALD the gas-phase precursors are not in the substrate chamber at the same time. Instead, they are separated by an inert gas purge to make sure that only one chemical is present in the chamber at any instant. By doing so, this allows each precursor to react with the surface of the heated substrate independently leaving behind a new surface layer. Once the chemical reaction is complete throughout the surface of the substrate, growth stops completely while the chamber is completely purged until the substrate is exposed to the next precursor. Because the chemical reaction is self-terminating, ALD growth can form monolayer-by-monolayer with unprecedented thickness control. Despite many publications and articles stating that ALD always grows one complete monolayer at a time, it should be noted that actual growth might not be one complete monolayer because of steric hindrance due to the size of the precursor molecule. In this work, that may have occurred while attempting to grow hafnium oxide, which utilizes a precursor that is quite large by ALD standards. This complication, and the results that occurred, will be mentioned more in chapter 3.

In addition to growing thin films monolayer-by-monolayer, ALD provides exceptionally good step coverage since the gas-phase precursors will fill every crevasse of the substrate. This is an advantage over CVD and traditional line-of-sight methods (e.g., sputtering, electron beam evaporation, thermal evaporation, pulsed laser deposition, etc.), which do not have good step coverage because of shadowing effects. Therefore, conformal coating of trenches, grooves,

pores, or any other 3D structure is possible when utilizing ALD. Due to these advantages, ALD is capable of producing high-density films with exceptional quality on 3D substrates.

These benefits of ALD are countered by a few limitations compared to CVD or other line-of-sight deposition techniques. Since ALD growth transpires monolayer-by-monolayer, the growth rate is very slow. Therefore, ALD is mainly conducive for the growth of extremely thin films. Each complete cycle provides a thickness on the order of 1 Å depending on the precursors used which determines the monolayer grown. For example, to grow a 20-nm film, approximately 200 cycles are required. The total time to complete 200 cycles depends on the system and can take a few hours for the custom-built system used in this work. Thankfully, the low growth rate is not a large problem for the film thicknesses needed in modern devices, which require only a couple of nanometers up to few tens of nanometers.

An additional disadvantage of ALD is that the first precursor exposure needs to properly nucleate the surface of the substrate (by physical adsorption or chemisorption) before uniform growth can occur. If complete nucleation occurs throughout the entire substrate surface then conformal coating will result. If nucleation only occurs on some of the surface, then islands of coating will form and ultimately the film will not be uniform.

Finally, proper ALD growth will only occur if the correct temperature window is maintained. If the temperature is too low two situations can arise; either precursor condensation will occur, leading to a higher growth rate than desired, or there will be low reactivity of the precursor, leading to a lower or non-existent growth rate. If the temperature is too high two additional situations can arise; either precursor decomposition will occur, leading to CVD and a higher growth rate than desired, or precursor desorption will occur, leading to a lower or non-

existent growth rate. All of these possibilities, along with the proper temperature window are shown in Figure 2.1.

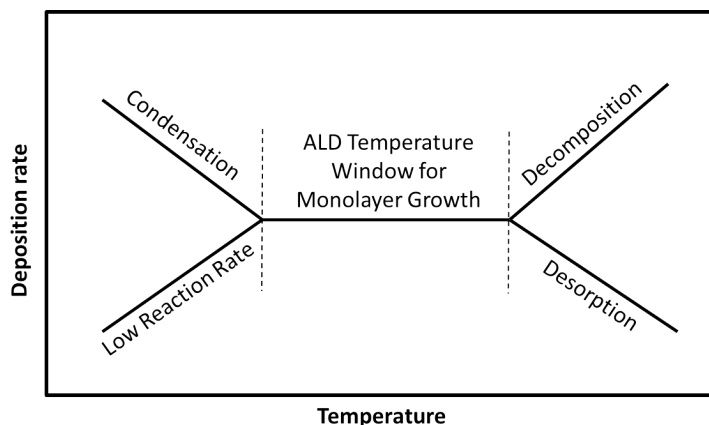


Figure 2.1 ALD temperature window

When two precursors are utilized to grow a thin film by ALD, the precursor exposures are cycled in an ABAB... pattern until the desired thickness is reached. Each AB cycle produces one monolayer of the desired material. A detailed schematic of the ABAB... growth pattern for aluminum oxide will be shown in detail after the introduction to some precursor information is covered.

2.1.3 ALD Precursors

Chemists have developed and synthesized many different ALD precursors which are capable of growing an abundance of materials.³¹ The development and synthesis of precursors is not a trivial process and is beyond the scope of this work, but the final products are expected to meet a number of requirements, which are important to understand.

An ALD precursor has to be stable with itself and the carrier gas (which should be inert) as they mix and enter the heated vacuum chamber. When the source diffuses into the heated

vacuum chamber it should only react with the surface of the substrate. This ensures that growth will only occur in a uniform manner and that it does not occur by CVD. Furthermore, the vapor pressure of an ALD precursor at different temperatures needs to be analyzed. Preferably the vapor pressure should be high enough at room temperature so that it will be able to easily diffuse into the carrier gas and travel to the substrate. Unfortunately, some precursors require heating in order to raise their vapor pressure enough to make this possible. Ultimately, the pressure of the precursor source and carrier gas should be approximately 1 Torr for viscous flow.³⁰ Finally, ALD precursors need to be highly reactive with the heated substrate surface but maintain good thermal stability to avoid premature decomposition. This follows the requirement that the proper temperature window must be maintained during deposition as mentioned earlier.

The only precursor that will not be covered in detail is water (H_2O) considering the physical and chemical characteristics are well known. Ultra-pure water was used as the oxygen source for all of the ALD oxides formed in this work, but it is not the only one mentioned in literature. It is also possible to produce ALD oxide films using oxygen gas (O_2), ozone (O_3), and hydrogen peroxide (H_2O_2) to name a few.³¹

Metal organic precursors constitute a large subset of ALD precursors, which meet many of the required characteristics.³⁵ In this subset is a smaller subset of precursors called organometallics. Organometallic precursors have at least one bond between a carbon atom of an organic compound and a metal. Their volatility and highly reactive nature have made them a favorite among ALD precursors.^{31, 36} Since the required characteristics for organometallic precursors were analyzed before sources were selected, the next section covers the important traits that were considered during the selection process. This work successfully utilized two organometallic precursors and those will be discussed, but the successful attempt to utilize a

third organometallic precursor failed to materialize. Nevertheless, it will also be discussed because lessons were learned in the unsuccessful attempts, and it has potential applications that will be mentioned later. In addition to covering the characteristics of the organometallic precursors, the films grown and chemical reactions that occurred for the two successfully utilized precursors are detailed.

2.1.3.1 Trimethylaluminum

The organometallic compound trimethylaluminum (TMA, $\text{Al}(\text{CH}_3)_3$) is one of the most commonly utilized precursors and has been extremely well researched.^{34, 37-38} For this work, it was used in conjunction with water to grow the insulating film aluminum oxide (Al_2O_3), but it can also be used in combination with other precursors to grow aluminum or materials that contain aluminum (e.g., aluminum-doped zinc oxide, aluminum nitride, aluminum arsenide, etc.).³¹ TMA is a liquid at 20°C with a vapor pressure of 9 Torr as can be seen in Figure 2.2. With the vapor pressure of water at room temperature being ~17 Torr, both precursors easily diffuse into the carrier gas for transport to the ALD chamber. Additionally, the starting decomposition temperature of TMA is 332°C leading to a high enough temperature window for the chemical reaction to occur before it would undergo decomposition. Finally, because TMA is an organometallic precursor, it is extremely volatile and reacts easily with the hydroxyl groups (-OH) on the surface of the substrate, which for this work was accomplished by exposing the heated substrate to a pulse of H_2O before the first exposure of TMA.

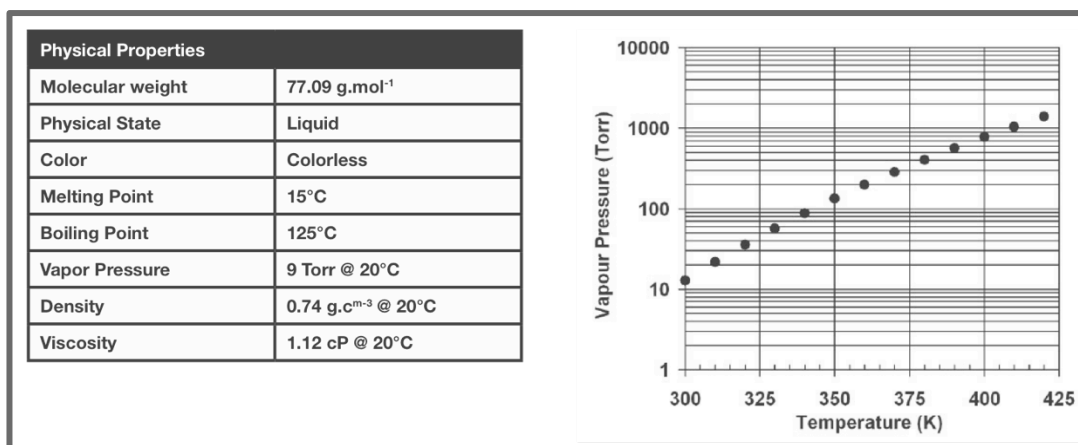
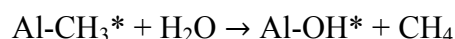
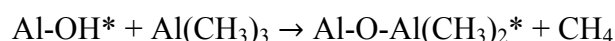


Figure 2.2 Physical properties of TMA along with a vapor pressure vs. temperature graph.

Source: Air Liquide Electronics (www.aloha.airliquide.com)

The two half-reactions that occur due to alternating TMA and H₂O exposures to produce Al₂O₃ are as follows:³⁹



where the asterisks denote the surface species and the byproduct of each half-reaction that is exhausted from the system is methane (CH₄). These two half-reactions produce approximately a monolayer of amorphous Al₂O₃.

Figure 2.3 is a key pertaining to the schematic showing the six steps for one ABA growth cycle of Al₂O₃. The growth is shown on a substrate with trenches to demonstrate how conformal coating would occur on a 3D surface. The chemical reaction that occurs during each exposure depends on the precursor used and surface species present, and it is not impeded by a 3D substrate as long as the exposure time is long enough for the precursor to diffuse into any crevasses present. If the 3D substrate contains crevasses that are very small, it is possible that they will completely close up during ALD growth. This is indicated by the small trench on the left-hand side of the diagrams that ends up being completely filled in the last step.

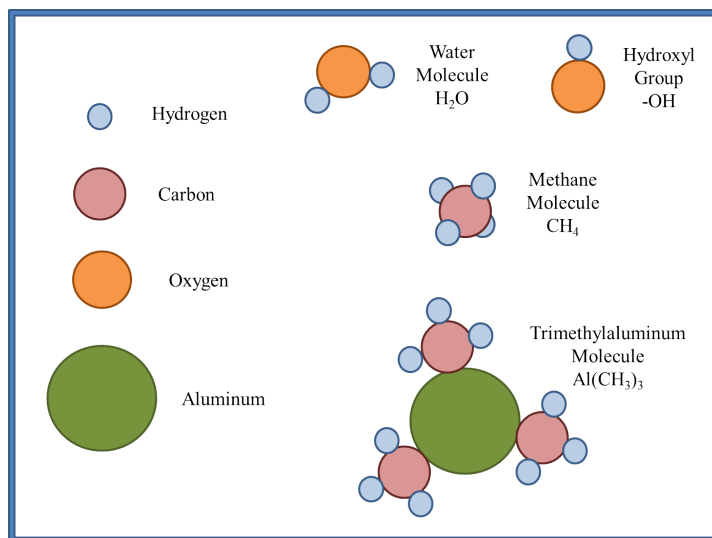
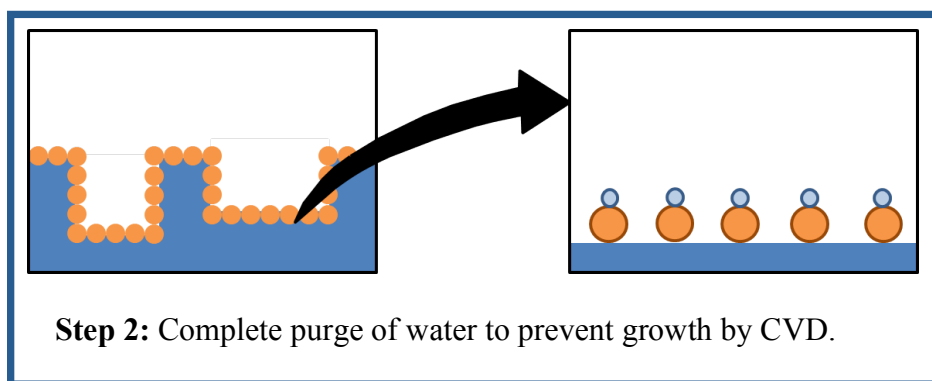
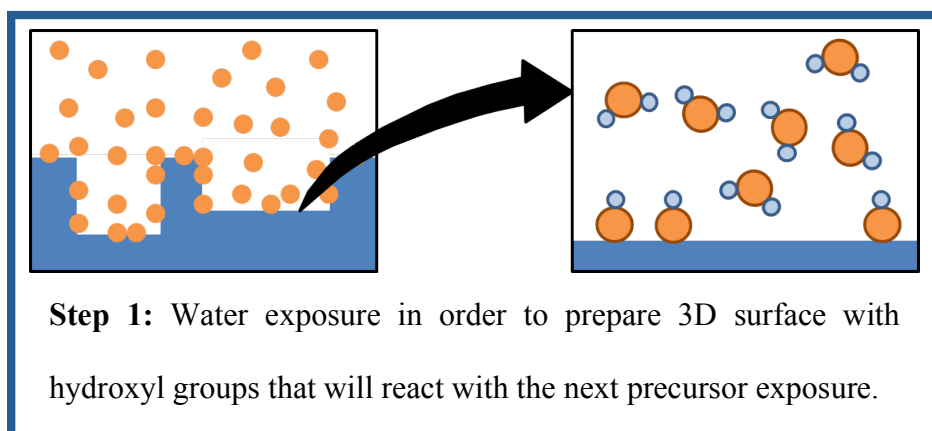
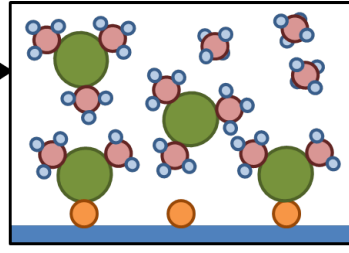
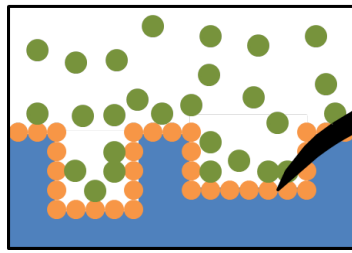
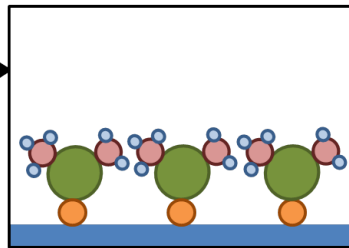
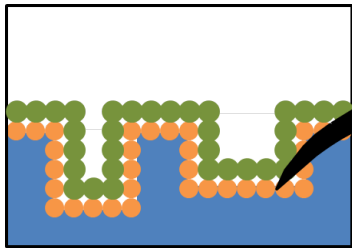


Figure 2.3 Key showing the elements and molecules used in the following figures for the growth of Al_2O_3 .

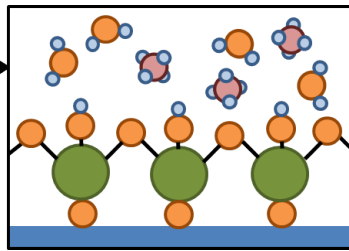
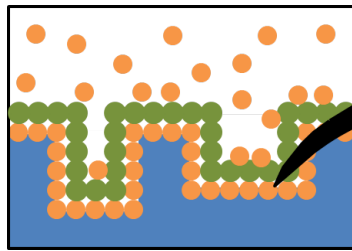




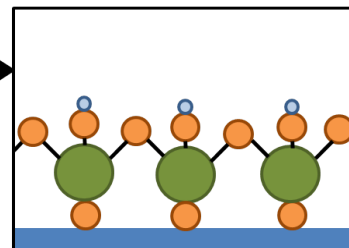
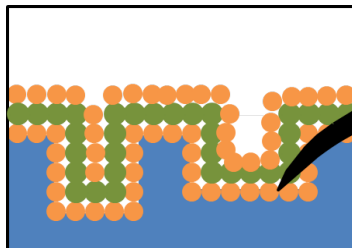
Step 3: TMA exposure in order to provide aluminum atoms that attach to oxygen atoms. Methane is the by-product of this reaction.



Step 4: Complete purge of TMA and methane to prevent growth by CVD.



Step 5: Water exposure in order to finish one layer of Al_2O_3 and hydroxylate the surface again. Methane is again the by-product of this reaction.



Step 6: Complete purge of remaining water and methane to prevent growth by CVD.

2.1.3.2 Diethylzinc

Another organometallic precursor utilized in this work was diethylzinc (DEZ, $\text{Zn}(\text{CH}_2\text{CH}_3)_2$). It was used in conjunction with water and TMA to grow the conducting film aluminum-doped zinc oxide (AZO),⁴⁰⁻⁴⁷ but it can also be used in combination with other precursors to grow zinc or materials that contain zinc (e.g., zinc oxide, zinc sulfide, and zinc selenide).³¹ Similar to TMA, DEZ is a liquid at 20°C with a vapor pressure of 15 Torr as can be seen in Figure 2.4. Therefore, it easily diffused into the carrier gas for transport to the ALD chamber. Unfortunately, the starting decomposition temperature of DEZ is 70°C which meant that it would start to decompose as soon as it entered the heated ALD chamber. Finally, because DEZ is an organometallic like TMA, it is extremely volatile and reacts easily with the hydroxyl groups (-OH) on the surface of the substrate.

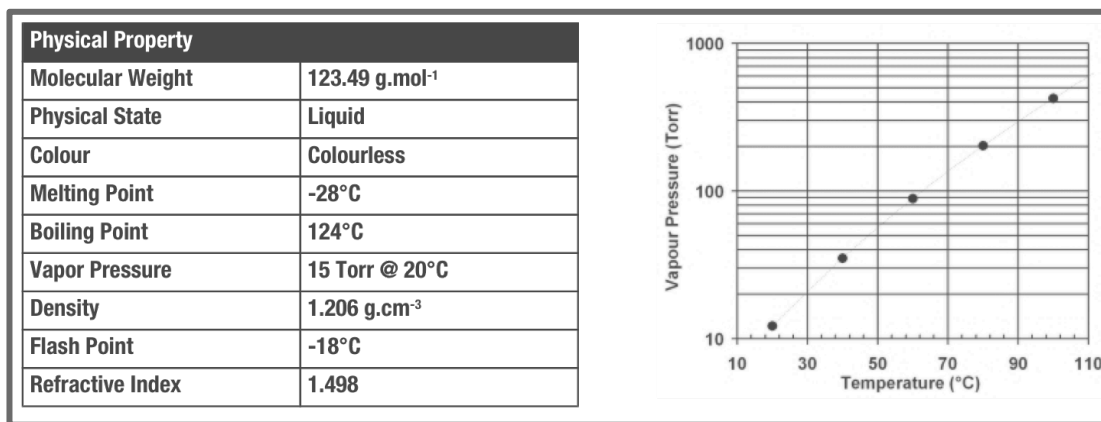
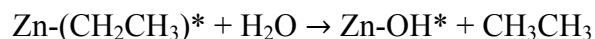
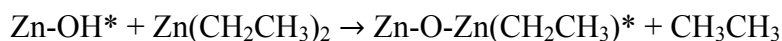


Figure 2.4 Physical properties of DEZ along with a vapor pressure vs. temperature graph.

Source: Air Liquide Electronics (www.aloha.airliquide.com)

The two half-reactions that occur due to alternating DEZ and H_2O exposures to form zinc oxide (ZnO) are as follows:⁴¹



where the asterisks denote the surface species and the byproduct of each half-reaction that is exhausted from the system is ethane (C_2H_6). These two half-reactions produce approximately a monolayer of ZnO with the thermodynamically preferred crystalline orientation. The ALD temperature window was determined to be 130-180°C, but the crystallinity was found to improve with increasing temperature.

If growth of AZO is desired, then all that needs to be done is to dope the ZnO films with aluminum during the ALD process. This requires replacing one DEZ pulse with a TMA pulse on occasion. The effect of various doping ratios has been studied extensively since it is this ratio that controls the conductivity of the AZO film.

2.1.3.3 Tetrakis(ethylmethlamino)hafnium

The final organometallic compound evaluated for this work, but not successfully utilized, was tetrakis(ethylmethlamino)hafnium (TEMAH, $Hf[N(CH_3)(C_2H_5)]_4$). It can be used in conjunction with water to grow the high-k dielectric hafnium oxide (HfO_2),^{36, 48-49} and it can also be used in conjunction with other precursors to grow materials that contain hafnium (e.g., hafnium nitride, $Hf_xAl_yO_z$, $Hf_xSi_yO_z$, and $Hf_xTi_yO_z$).^{31, 50} Similar to TMA and DEZ, TEMAH is a liquid at room temperature but, unlike the other two, it does not have a high vapor pressure. According to Air Liquide's data table shown in Figure 2.5, the vapor pressure at 70°C is only 0.1 Torr. That is very low compared to the vapor pressures of the other precursors and; therefore, diffusion of TEMAH into the carrier gas is not very easy to accomplish. In order to raise the vapor pressure, the source bubbler needs to be heated carefully since it also has a relatively low decomposition temperature (~140°C). It was previously mentioned that DEZ also has a low decomposition temperature (~70°C), but for DEZ the source bubbler did not have to be heated.

This is because it already has a sufficient vapor pressure at room temperature to diffuse into the carrier gas. But for TEMA_H, the source needs to be heated just so it can diffuse into the ALD chamber. The last challenge faced by using TEMA_H is its size. It has four relatively large ligands attached to the central hafnium atom. Therefore, steric hindrance can be a problem when trying to coat high aspect ratio or porous structures. The results of this difficulty will be discussed in more detail in chapter 3.

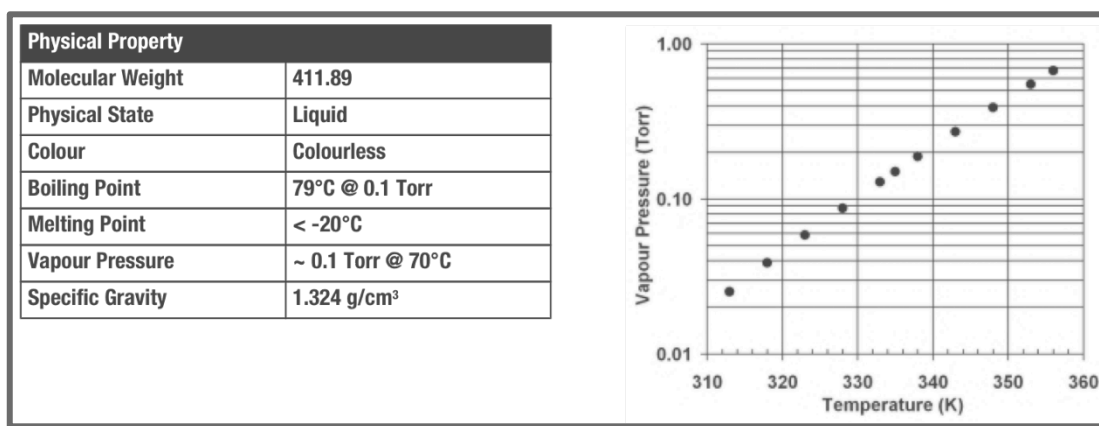


Figure 2.5 Physical properties of TEMA_H along with a vapor pressure vs. temperature graph
Source: Air Liquide Electronics (www.aloha.airliquide.com)

2.1.4 ALD Custom-Built System Design and Operation

The components of an ALD system are relatively quite simple and a schematic of the custom-built system used for this work is shown in Figure 2.6. This system was based off of the design published by J. W. Elam *et al.*⁵¹ and has been described in great detail in a collaborated report.⁵²

The main components for the system are as follows:

1. ALD chamber wrapped with heating rope
2. Gas-phase precursors and an inert carrier gas
3. Rotary vane mechanical pump
4. Computer controlled solenoid valves for AB sequencing

In addition to those four main components, our system has a load lock, magnetic transport rod, and mass flow controller for the inert carrier gas source.

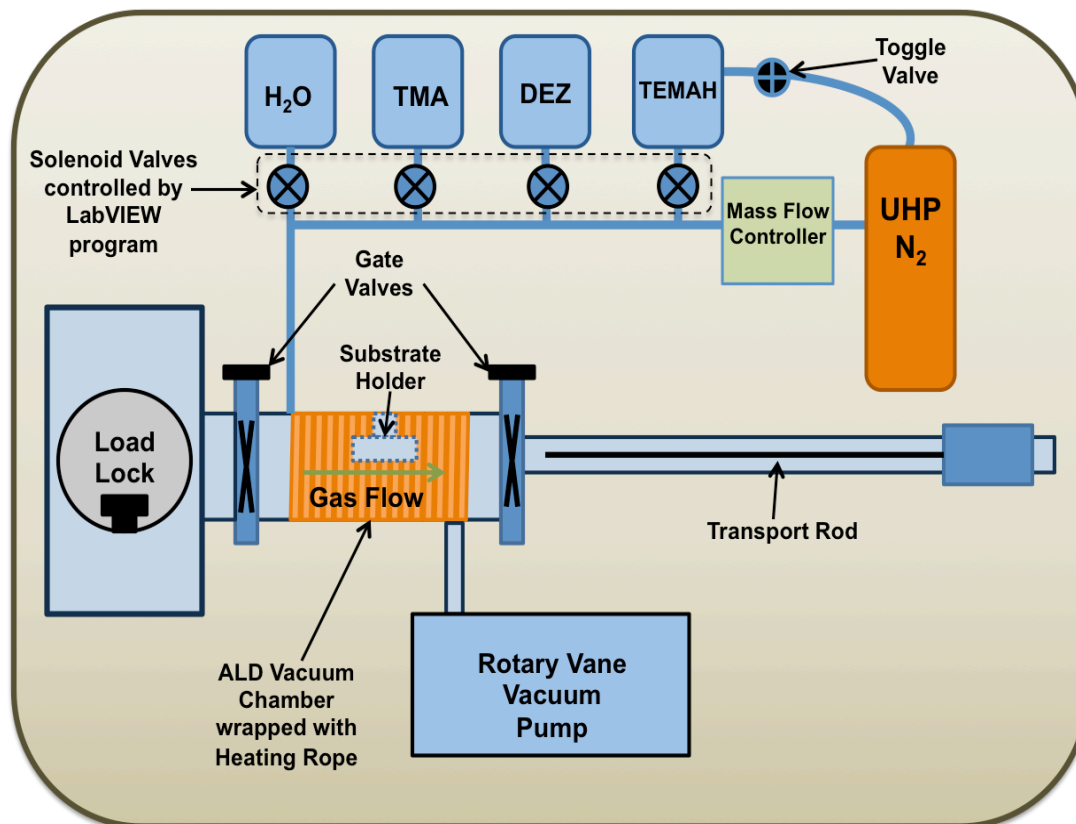


Figure 2.6 Design of custom-built ALD system

Before operation of the ALD system, the substrate was carefully mounted to the sample stage by use of small clamps that are attached along the edge of the stage. After the substrate was mounted to the sample stage, it was screwed onto the end of a magnetic transport rod in the load lock and then transferred to the stainless steel, temperature controlled ALD chamber. Once inside the ALD chamber, the sample stage would be pulled into mounting rails and then unattached from the transport rod. The transfer rod was removed by unscrewing it from the sample stage and then pulled out of the ALD chamber into its storage unit. At this point the gate valves to the load lock and transport rod storage unit were closed so the chamber could be

evacuated by use of a rotary vane mechanical pump. A gate valve connecting the mechanical pump to the ALD chamber was opened until it reached its base pressure (~ 30 mTorr). Once the ALD chamber reached its base pressure, the gate valve to the vacuum pump was closed, and a Variac variable transformer was turned on to raise the temperature of the resistive heating rope for radiant heating of the substrates. The internal temperature of the ALD chamber was monitored by a thermocouple connected through a viewport. While the temperature was slowly increasing until it reached thermal equilibrium inside of the ALD chamber, an automated LabVIEW program, which operated a computer controlled solenoid valve system, was used to pump down the stainless steel delivery lines connected to the precursors. Pumping of these lines was done through a separate solenoid valve that was attached directly to the mechanical pump so as not to expose the substrates to any stray precursors. Once the ALD chamber reached the required temperature, and all of the delivery lines were pumped down properly, ultra-high purity nitrogen (UHP N₂) was allowed to flow into the delivery lines via a mass flow controller. The LabVIEW program was then again utilized to deliver doses of the gas-phase precursors through the AB sequencing mentioned previously. The total cycling count was maintained by the LabVIEW program, and automatic closure of the solenoid valves to the precursors was done once the anticipated number of cycles was completed. Throughout the deposition, the ultra-high purity nitrogen gas was used to purge the chamber of stray precursor gas in between cycles. This makes sure that growth does not occur by CVD. In addition, the carrier gas helps to raise the pressure to ~ 1 Torr to achieve viscous flow, which is ideal for ALD growth to occur.

2.2 Vertically Aligned Carbon Nanofibers Arrays

Carbon-based nanostructured materials come in many different forms with each form having a unique structure while displaying a specific set of properties. These individual characteristics allow the carbon-based material to be utilized in nanotechnology applications in various fashions to maximize their effectiveness.¹⁰⁻¹² This section discusses a specific type of carbon-based nanostructured material, vertically aligned carbon nanofiber (VACNF) arrays, and why its high aspect ratio 3D nature is beneficial toward coating with functional materials.⁵³ In addition, this section introduces the structure and properties of carbon nanofibers (CNFs), explains how they are different from carbon nanotubes (CNTs), and discusses the properties of many free-standing CNFs in a vertically aligned array.

2.2.1 Structure of CNFs and CNTs

Carbon-based nanostructured materials exist in many forms with some of them composed of a hexagonal network of covalently bonded carbon atoms as they are in graphene. Single-layer graphene has drawn a great deal of attention since its isolation in 2003,⁵⁴ and its base structure is shown in Figure 2.7a.⁵⁵ It resembles a honeycomb crystal lattice where each carbon atom is covalently bonded to three other carbon atoms. Because carbon has four valence electrons, one of those three bonds must contain a double-bond. Since all four valence electrons are accounted for in the hexagonal network, a single sheet of graphene is chemically inert and the in-plane bonding of the carbon atoms gives graphene its outstanding electrical and mechanical properties.

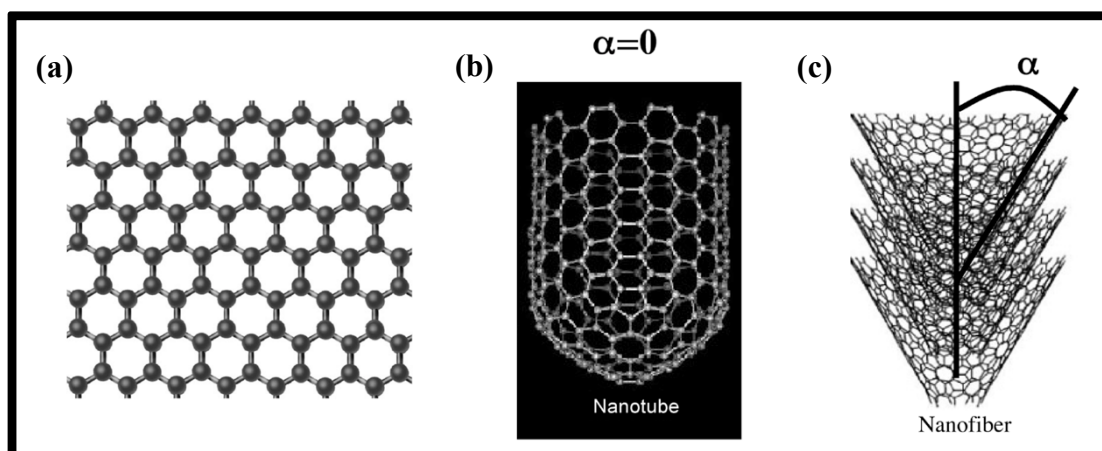


Figure 2.7 Schematics of a (a) single sheet of graphene, (b) carbon nanotube, and (c) carbon nanofiber with stacked graphitic cones.

CNTs and CNFs are two distinct examples of carbon nanostructured materials that contain the same carbon hexagonal network as in graphene. Both structures are grown as long cylinders and can look similar to each other under low magnification imaging, but they have distinct structural differences that are important to note. Since CNTs have been known and researched for a longer period of time, it was not uncommon in early references to mistake CNFs for CNTs and not distinguish between the two. As of late, attention to detail has prevailed, and most publications are very specific in describing the type of cylindrical carbon structure that is being utilized. This is important since the specific structure determines its properties.

The main structural difference between CNTs and CNFs is in how the graphene-based sheets are organized to make up the long cylinders. Single-walled CNTs (Figure 2.7b)⁵⁶ resemble a rolled sheet of graphene⁵⁷ and multi-walled carbon nanotubes (MWCNTs) resemble concentric rolled sheets of graphene, whereas, CNFs resemble stacked cups or cones of graphene sheets (Figure 2.7c).⁵⁶ As can be seen in Figures 2.7b and c, the angle between the cylindrical axis and the basal plane of the graphene sheet, α , determines what type of cylindrical structure formed. CNTs and MWCNTs have $\alpha = 0^\circ$, but the two main types of CNFs mentioned in literature have $\alpha > 0^\circ$. The first type has a stacked cone-like nature and is referenced as a “herringbone” CNF

because it resembles a fish skeleton under TEM imaging as is shown in Figure 2.8a.⁵⁵ This was the type of CNF that was utilized for this experiment. The second type of CNF has a stacked cup-like nature and is referenced as a “bamboo” CNF because it resembles a bamboo stem under TEM imaging as shown in Figure 2.8b.⁵⁵ In some earlier works, this type of CNF is referenced as a MWCNT, but the latest literature does a better job of distinguishing between the different forms. Since both types of CNFs are fabricated using a metal catalyst, they grow with a metallic tip that is clearly visible as a dark black object at the top of each CNF under TEM imaging as shown in Figures 2.8a and b. However, since CNTs are not fabricated in the same fashion, they do not contain a metallic tip but instead are capped with a graphene dome at one end as the drawing shows in Figure 2.7b.

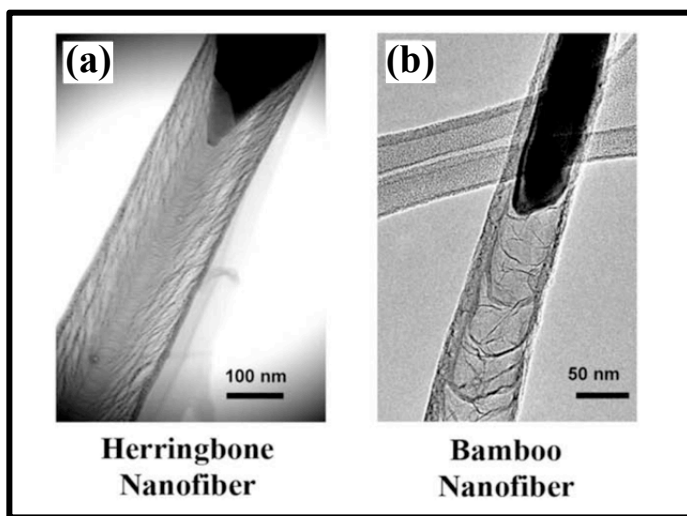


Figure 2.8 Transmission electron microscope images showing the different structures of a (a) herringbone CNF and a (b) bamboo CNF.

2.2.2 Properties of CNFs and CNTs

While the angle between the cylinder axis and basal plane defines the type of cylindrical carbon nanostructure that formed, the arrangement and bonding of the carbon atoms determines the electrical, mechanical, and chemical properties of each. Graphene layers, which are relatively

short and stacked together with each one spanning only a portion of the entire nanofiber, have different properties than one sheet of graphene rolled into a tube that spans the entire length of the cylinder. The following subsections discuss the three main properties that are affected by the structural differences.

2.2.2.1 Electrical

In a CNT, electrons move along the outside of the cylinder in the basal plane, which consists of the covalently bonded carbon atoms. This can lead to exceptional electrical properties when the graphene sheet is formed accordingly and when the sidewalls are defect-free. Different formations of the rolled graphene sheets result in either a metallic or semi-metallic nature for the CNT.⁵⁸ However, CNFs consisting of the stacked cups or cones of graphene would have electrons moving along both the basal plane and from one graphene sheet to another. Because of this, the overall resistivity increases but not significantly. Furthermore, the spacing between the graphene cones changes as the electrons travel toward the base as shown in Figures 2.9a and b.⁵⁶

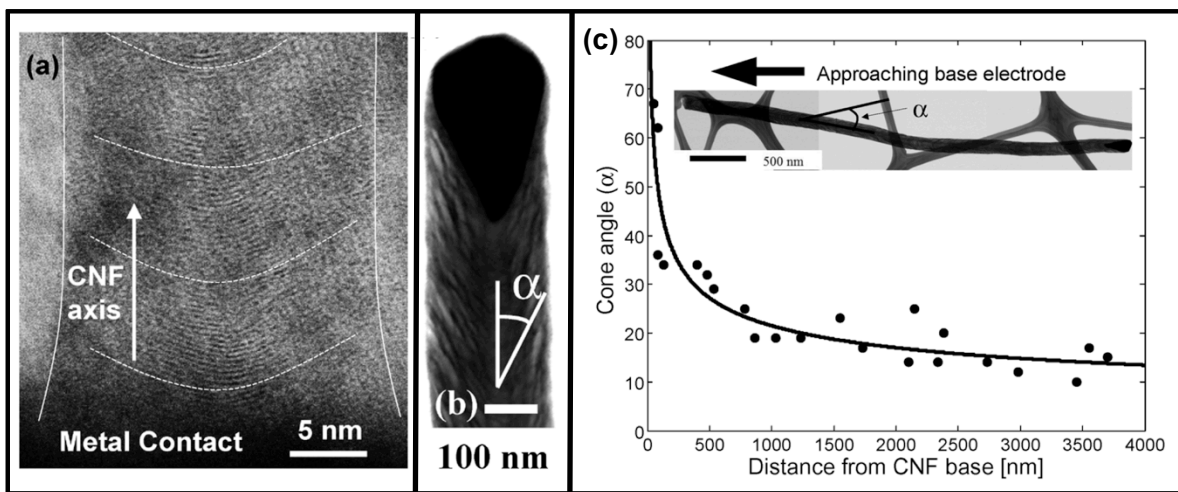


Figure 2.9 (a) Image of a 20 nm diameter CNF near the metal contact base showing the layering of graphene sheets almost perpendicular to the axis of the CNF. (b) TEM image of CNF showing angle α between CNF axis and basal plane of graphene cone. (c) Graph showing how the angle α changes with distance to the CNF base.

This is because the cone angle, α , increases as the distance decreases from the CNF base as shown in the graph of Figure 2.9c.⁵⁶ Despite these differences in structure compared to CNTs, CNFs still provide exceptional charge transport characteristics, which will be mentioned more in the next section.

2.2.2.2 Mechanical

Additionally, the mechanical properties of a CNF are quite different from a CNT since the van der Waals bonding between the graphene planes differs drastically from the covalently bonded carbon atoms along the basal plane. Because covalently bonded carbon atoms are extremely strong, CNTs have exceptional mechanical strength along the length of the tube with a Young's modulus up to approximately 1 TPa.⁵⁹ The strength of a CNF along the length of the fiber is considerably less due to the weak van de Waals bonds between the stacked graphitic cones. Therefore, they can easily be pulled apart exposing the graphitic cones, which will be shown in future figures. This is an unfortunate property of CNFs, but it did not affect the results of this work. Despite the mechanical weakness along the length of the fiber, the interlayer spacing of $\sim 3.4 \text{ \AA}$ ⁶⁰ is conducive toward ALD growth. This spacing is less than either of the lattice constants for crystalline Al_2O_3 and, hence, small enough for amorphous growth to occur.

2.2.2.3 Chemical

The chemical property distinction between CNFs and CNTs is the most important difference for this work. Because ALD was chosen to conformally coat the 3D nanostructures, it is important that the nanostructured surfaces are able to support proper nucleation and, hence, ALD growth. The difference between the physical structures of a CNT and a CNF is what provides a CNF the

advantage for ALD coating.

The structural nature of a pristine, defect-free CNT does not contain any exposed graphitic edges with unsaturated bonds along the nanotube wall. Therefore, if the sidewalls of a CNT are defect-free, then they are chemically inert as well.⁶¹ As a result, CNTs are far less reactive than CNFs. For ALD growth to occur, the sidewall first needs to be covalently or noncovalently functionalized. Covalent functionalization induces defect sites along the sidewall of the CNT, but this causes degradation in the electron-transport properties in addition to only providing random nucleation sites for ALD growth to occur.⁶² Since the nucleation sites are random, ALD growth does not cover the surface conformally but instead in patches or islands of growth. Noncovalent functionalization does not create defect sites; hence, uniform ALD growth can be achieved. However, in order to functionalize the surface noncovalently, additional procedural steps and chemicals are required, which leads to higher cost and longer fabrication time.⁶³

Whereas pristine CNTs do not contain any unsaturated bonds, the exposed graphitic edges of a CNF contain dangling bonds that provide the perfect sites for chemical reactions to occur via ALD. Therefore, CNFs do not require the additional functionalization steps for ALD nucleation to occur. The growth process can begin with a simple water pulse, which prepares the dangling bonds along the graphitic edges with hydroxyl groups ($-OH$) that are then reactive with the next precursor exposure. This simple process for hydroxylating the surface of a CNF is the main advantage for use in this work.

2.2.3 Characteristics of Vertically Aligned Carbon Nanofibers

Vertically aligned carbon nanofiber (VACNF) arrays are grown by catalytic decomposition of a carbon-containing gas (e.g., acetylene; C_2H_2) on a hot metal surface. Their lower growth temperature and superior vertical alignment make them an advantageous option over vertically aligned MWCNTs.¹⁸ Figure 2.10 reveals a pristine VACNF array grown by plasma-enhanced chemical vapor deposition (PECVD).⁶⁴ Each individual CNF free-stands on the substrate surface and contains a nickel catalyst particle at the top, which is enclosed by a few graphitic carbon layers. The nickel tip is difficult to verify under SEM imaging, but in the earlier TEM images shown in Figures 2.8a and b it is clearly visible on top of the stacked graphitic cones.

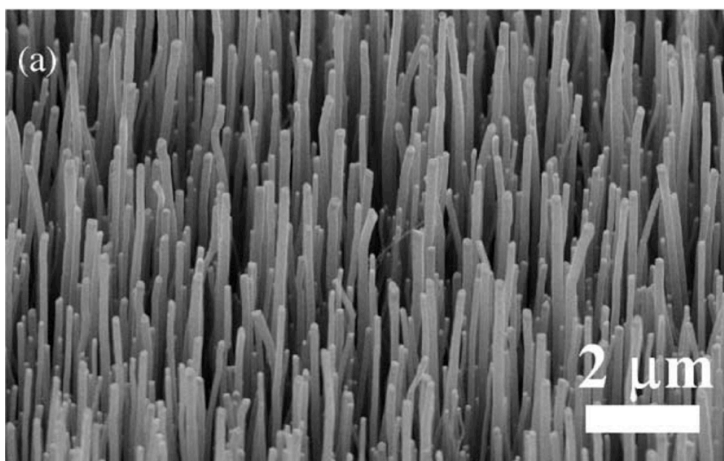


Figure 2.10 SEM image of an as-grown vertically aligned carbon

The growth conditions (e.g., time, gas flow rates, and temperature) can be tuned, and the substrate surface or catalyst varied, to alter the physical features of the VACNFs. They commonly have diameters ranging from ~50-150 nm and lengths of a few micrometers but can be grown to tens of micrometers.^{18, 59, 64-66} When CNFs are grown with a small diameter and large length they have a high aspect ratio, which leads to a large surface to volume ratio. Unfortunately, CNFs with too small of a diameter are not as mechanically durable compared to

those that are thicker. Those with a larger diameter (larger than 100 nm) have much stronger mechanical properties and can still provide a large aspect ratio. For example, a CNF with a length of 4 μm and a diameter of 100 nm provides a 40:1 aspect ratio.

VACNF arrays have areal densities up to $\sim 2 \times 10^9$ CNFs/cm² which leads to an average spacing between the CNFs of $\sim 300 - 400$ nm.^{65, 67} This amount of space in between CNFs is enough to allow for easy access of the gas-phase precursors down the whole length of the fiber in order to ensure proper ALD growth. The large spacing between VACNFs is another distinguishing factor compared to vertically aligned CNTs, which have a much higher density but also smaller diameters (less than 20 nm) usually leading to bundles¹⁷ or a tangled structure.

The electrical characteristics of the CNFs were determined using either a single CNF with leads attached to the sidewalls (4-probe design) or as multiple VACNFs with leads attached to the ends (2-probe design). All measurements were taken at room temperature. Resistivities acquired from the 2-probe design ranged from $\rho = 0.4 - 0.7$ m $\Omega\cdot\text{cm}$ ^{65, 67} while those acquired from the 4-probe design ranged from $\rho = 3 - 7$ m $\Omega\cdot\text{cm}$.⁶⁶⁻⁶⁷ A 4-probe design should reduce the resistivity by eliminating the contact resistance, but the results obtained reveal that it was actually one order of magnitude larger. This order of magnitude difference can be attributed to the varying measurement methods and the CNFs not having the exact same geometry.⁵⁶

The 4-probe measurements performed by L. Zhang *et al.* determined the average resistivity to be 4.2×10^{-3} $\Omega\text{ cm}$ which was calculated using $\rho = (R \cdot A)/L$ where $A = \pi r^2$ ($L = 0.880$ μm and $r = 67.75$ nm and $R = 2700$ Ω).⁶⁶ The resistivity of graphite parallel to the basal plane is 4×10^{-5} $\Omega\cdot\text{cm}$ and perpendicular to the basal plane is 4×10^{-2} $\Omega\cdot\text{cm}$. Therefore, the value they received would imply that it is a combination of the two. That is to be expected as indicated by the structure shown in their drawing used to represent the CNF (Figure 2.11)⁶⁶. When electrons

travel down the CNF they have to cross from one graphitic layer to another. This increases the overall resistance of the CNF compared to the resistance experienced by an electron that only travels along the basal plane of a graphene sheet, as in the case of a CNT. Furthermore, Zhang *et al.* showed that the net resistivity for a CNF could be calculated using the following equation:

$$\rho(\theta) = \rho_a \sin^2 \theta + \rho_c \cos^2 \theta \quad (2.1)$$

where ρ_a is equal to the resistivity parallel to the basal plane of graphite and ρ_c is equal to the resistivity perpendicular to the basal plane. The angle θ is related to the angle α , which both depend on the formation of the CNF.

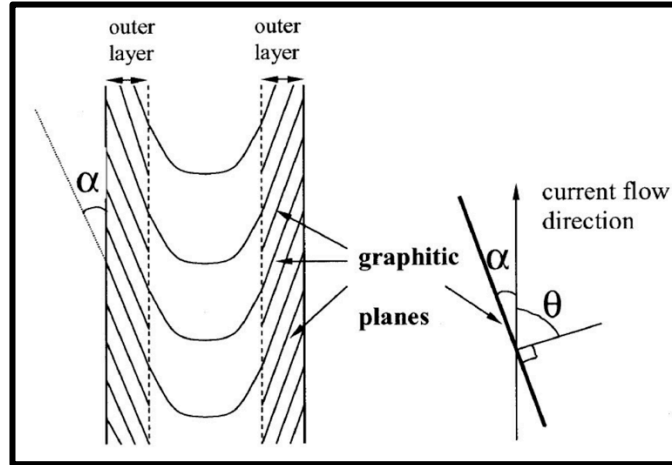


Figure 2.11 Drawing to show how the current flow through a CNF crosses graphitic plane boundaries.

Q. Ngo *et al.* performed two-probe measurements using multiple VACNFs.⁵⁶ After PECVD growth of the VACNF array, they embedded the CNFs with SiO₂ by CVD. This allowed for the individual CNFs to remain vertical and ensure electrical isolation after the top was mechanically polished. Once the top of the VACNF array was mechanically polished, electrodes were attached to the conducting base and on top of the VACNF array in order to complete the circuit for

characterization. They determined the VACNF arrays to have a highly metallic property with an average resistivity for Ni-catalyzed CNFs to be $(6.3 \pm 1.5) \times 10^{-4} \Omega \text{ cm}$.

2.3 Plasmonics

2.3.1 Introduction to Plasmonics

In the early 1950's, D. Pines and D. Bohm worked toward an explanation as to why fast moving electrons through metal foils experienced energy losses.⁶⁸⁻⁷⁰ They predicted that some of the losses were due to the formation of plasma oscillations (i.e., "plasmons" as they called it) of the free electrons in the metal foils. Subsequently, the innovative work published by R. H. Ritchie in 1957 led to the prediction of coherent collective oscillations of the conduction electrons along metal surfaces when exposed to fast moving electrons.⁷¹ These quanta of coherent collective oscillations along a metal surface have since been named surface plasmon by Stern and Ferrell.⁷²

The prediction of surface plasmon has ultimately led to the field of science called plasmonics, which is the study and application of the interaction between electromagnetic field oscillations with the free electrons in a metal. The field of plasmonics has a wide range of applications for use in numerous scientific disciplines, which include photovoltaics, surface-enhanced spectroscopies, biological and chemical sensing, and lithographic fabrication to name a few.⁷³ For this work, plasmonic nanoparticles were added to a 3D nanostructured transparent conductor as a proof-of-concept idea. By utilizing plasmonic nanoparticles in photovoltaics, it is possible to improve a solar cell's efficiency due to increased light harvesting.⁷⁴⁻⁷⁷ Further details on this application will be covered in chapter 4.

2.3.2 Surface Plasmon

Surface plasmons can occur along the interface between a material with a negative permittivity that contains free electrons and another material with a positive permittivity.⁷⁸ They are produced when an electromagnetic wave is incident upon a metal surface. When this occurs, the free electrons (i.e., conduction band electrons) of the metal are displaced in accordance with the oscillating electric field of the electromagnetic wave. As the electrons along the metal surface are displaced, a charge separation occurs with respect to the ionic lattice, which forms an electric dipole that oscillates along with the incident electric field. Hence, surface plasmons are quantized collective oscillations of surface charge that behave like particles with a discrete energy.

When surface plasmons propagate along the metal-dielectric interface they have momentum and are called surface plasmon polaritons. A diagram of a surface plasmon polariton propagating in the x- and y-directions along the metal-dielectric interface is shown in Figure 2.12.⁷³ Along the direction of propagation, they can travel a distance on the order of tens to hundreds of microns, but along the z-direction they decay exponentially on the order of only a couple

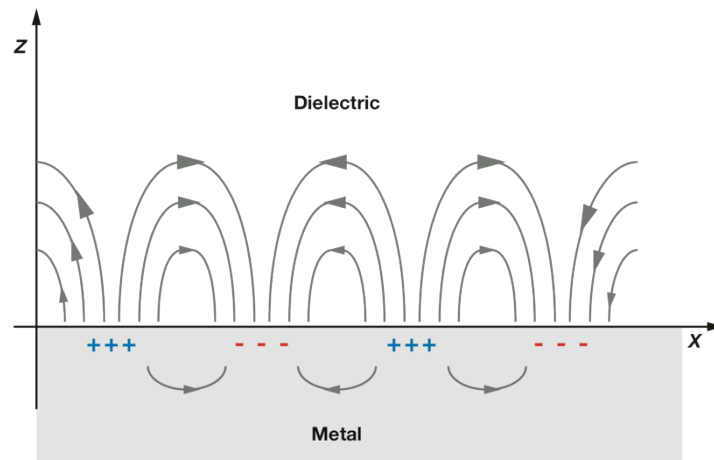


Figure 2.12 A diagram showing surface plasmon polaritons propagating along the x-direction and decaying evanescently in the z-direction.

hundred nanometers. The field perpendicular to the direction of propagation (z-direction in Figure 2.12) is said to be near field in nature because of the bound, non-radiative nature of the surface plasmon.

The dispersion relation for a surface plasmon is given by the following equation.

$$k_x = \frac{\omega}{c} \sqrt{\frac{\epsilon_1 \epsilon_2}{\epsilon_1 + \epsilon_2}} \quad (2.2)$$

In this equation k_x represents the wave vector in the x-direction, ω the radial frequency of the incident electromagnetic wave, c the speed of light, ϵ_1 the dielectric constant of the metal, and ϵ_2 the dielectric constant of the dielectric material ($\epsilon_2 \approx 1$ for air). The bulk plasmon frequency, ω_P , for a metal is given by:

$$\omega_P = \sqrt{\frac{ne^2}{\epsilon_0 m^*}} \quad (2.3)$$

where n is the electron density of the associated metal ($\sim 10^{23}$ electrons/cm³), e is the charge of an electron, ϵ_0 the permittivity of free space, and m^* the effective mass of the electron, which is equal to the mass of an electron in a metal.

A plot of the dispersion relation is shown in Figure 2.13. Notice that when k_x is small a surface plasmon polariton behaves like a photon following the blue line where $\omega = ck_x$. As k_x increases the dispersion relation levels off as it approaches the horizontal asymptote. This occurs when the surface plasmon polariton oscillates at the surface plasmon frequency. The surface plasmon frequency, ω_{SP} , is related to the bulk plasmon frequency by the following equation.

$$\omega_{SP} = \frac{\omega_P}{\sqrt{1+\epsilon_2}} \quad (2.4)$$

where ϵ_2 is again the dielectric constant of the dielectric medium. If the dielectric medium is air, then $\epsilon_2 \approx 1$, and the surface plasmon frequency reduces to the following equation.

$$\omega_{SP} = \frac{\omega_P}{\sqrt{2}} \quad (2.5)$$

This simplified expression for the surface plasmon frequency represents the horizontal asymptote shown in Figure 2.13.

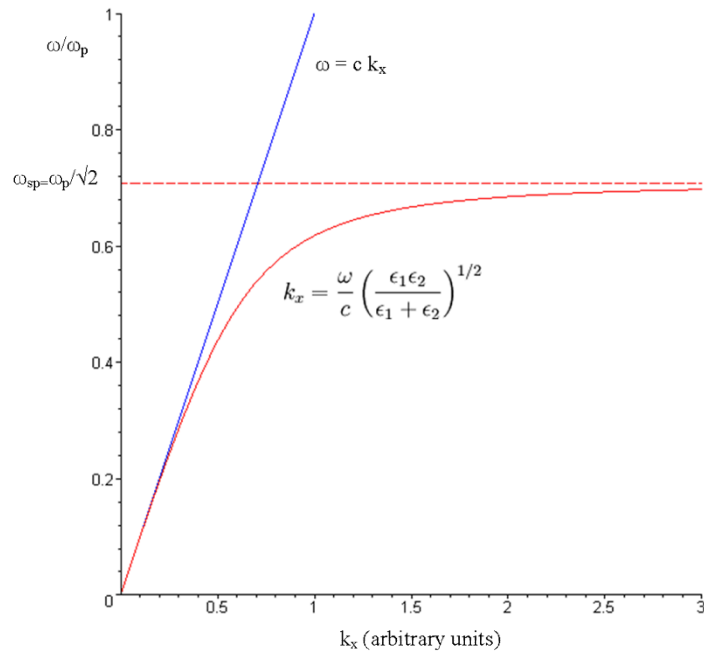


Figure 2.13 A graph of the dispersion relation for surface plasmons.

Source: https://en.wikipedia.org/wiki/Surface_plasmon

The maximum amplitude of the surface plasmon oscillation occurs when the frequency of the incident electromagnetic wave matches the surface plasmon frequency of the metal shown in equation 2.4. This produces a phenomenon called surface plasmon resonance. When surface

plasmon resonance occurs the free electrons at the metal surface are excited in a coherent oscillation with the incident electromagnetic wave.

If an electromagnetic wave is incident upon metal particles that are much smaller than the wavelength of the incident electromagnetic wave, the surface plasmons produced are termed localized surface plasmons. The metal particles in this case are called metal nanoparticles since the incident electromagnetic wave is on the nanoscale. A diagram representing localized surface plasmons is shown in Figure 2.14.⁷³ As the electron cloud is displaced due to the incident electric field, the metal nanoparticle obtains a positive charge on the opposite end. This in turn provides a restoring force for the electron cloud after the electric field has passed through. Hence, the localized surface plasmon frequency is a result of this restoring force, and it can be tuned by the size and shape of the metal nanoparticles in addition to the materials used to form the metal nanoparticles and surrounding dielectric material. Due to this phenomenon, plasmonic devices that employ metal nanoparticles have the ability to confine electromagnetic oscillations to volumes that are much smaller than the wavelength that would be generated in free space at that same frequency.

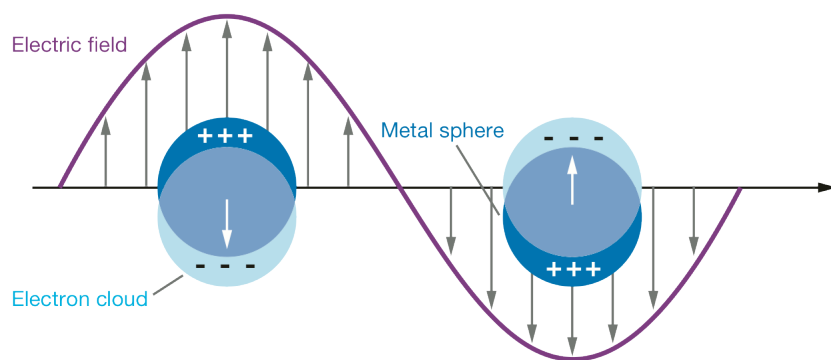


Figure 2.14 Diagram showing localized surface plasmons.

In a similar manner to surface plasmon resonance, it is also possible to induce a localized

surface plasmon resonance. This occurs when an incident electromagnetic wave has a frequency that matches the resonant frequency for localized plasmon oscillation in a metal nanoparticle. This frequency is determined by the type of metal (i.e., different metals have different complex dielectric constants), dimensions, and shape of the metal nanoparticles. In addition, LSPR produces both strong absorption and strong scattered of the incident light.

Our group has been particularly interested in the plasmonic effect of gold nanoparticles (AuNPs), and papers regarding this topic have been published. F. Wang *et al.* generated AuNPs on fluorine-doped tin oxide (FTO) photonic nanopatterns.⁷⁹ The AuNPs were produced via thermally assisted self-assembly from gold films formed by electron-beam evaporation and the FTO photonic nanopatterns by nanoimprint lithography. Scanning electron microscope (SEM) images clearly revealed the AuNPs on top of the FTO nanopatterned structures as shown in Figure 2.15⁷⁹. These AuNPs were formed from a 12 nm nominal thickness gold film.

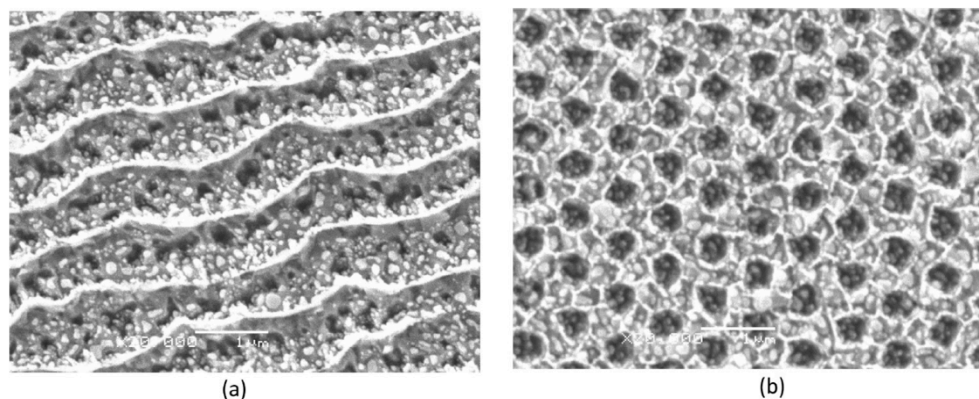


Figure 2.15 SEM images of 12 nm nominal thickness AuNPs on (a) nanoline patterned FTO and (b) nanopillar patterned FTO.

This work also clearly revealed the LSPR effect by both experiment and computer simulation. Figure 2.16⁷⁹ displays a computer simulation of an electromagnetic field distribution after passing through an FTO nanopatterned surface without (Figure 2.16a) and with AuNPs

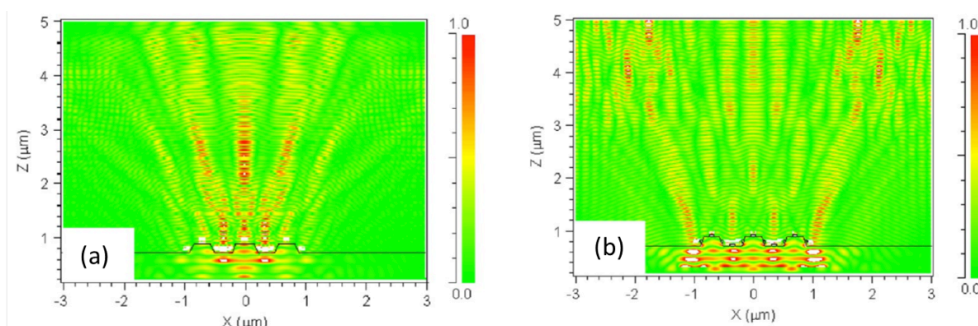


Figure 2.16 Computer simulation of the power distribution for an incident Gaussian beam passing across (a) a patterned FTO structure without AuNPs and (b) the same patterned FTO structure with AuNPs.

(Figure 2.16b). There is a clear increase in the power distribution with the addition of AuNPs to the surface of the FTO photonic nanopatterned surface. In addition, Figure 2.17⁷⁹ shows the experimental LSPR effect on a transmittance vs. wavelength graph. This graph has noticeable dips in the transmittance when the LSPR frequency of the AuNPs is reached. In addition, the LSPR wavelength is redshifted when applied to the nanopatterned FTO surfaces in comparison to the planar FTO sample.

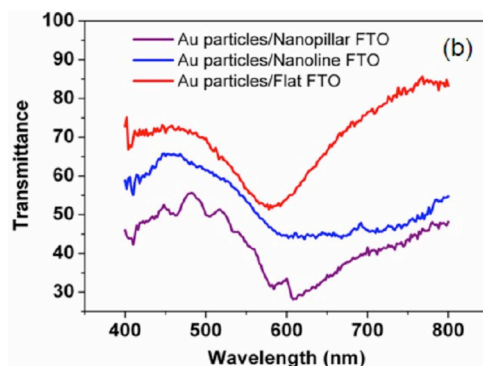


Figure 2.17 Transmittance vs. wavelength graph revealing the LSPR effect (dip in the graph) for AuNPs applied to a planar FTO (red), nanoline patterned FTO (blue), and nanopillar FTO (purple) substrates.

An additional work from our group, by R. Lu *et al.*, also revealed some valuable information on the physical dimensions of plasmonic AuNPs grown on different surfaces.⁸⁰ In this paper, it was clearly evident that the AuNP's lateral dimensions increased when assembled from a larger

nominal film thickness of gold as indicated by the SEM images in Figure 2.18⁸⁰.

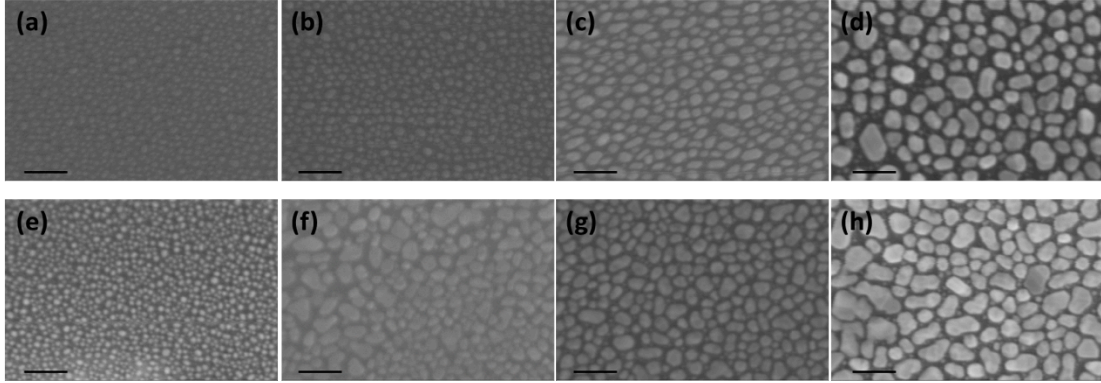


Figure 2.18 Surface morphologies of *in-situ* fabricated AuNPs on SiO₂/Si [(a)-(d)] and CVD graphene [(e)-(h)] with different nominal Au thicknesses of: 2 nm [(a) and (e)], 4 nm [(b) and (f)], 8 nm [(c) and (g)], and 12 nm [(d) and (h)]. The scale bar is 100 nm.

Furthermore, this paper verified the LSPR wavelength range for the varied nominal thicknesses of AuNPs (Figure 2.19)⁸⁰. Included in this graph is some additional information that will be referred to later in chapter 4. When a conducting substrate is located between the AuNPs and glass interface, the LSPR wavelength (i.e., lowest point in the dip) is redshifted compared to the substrate without this conducting layer. For Lu *et al.*, the conducting layer was CVD graphene, but for this work it was ALD AZO.

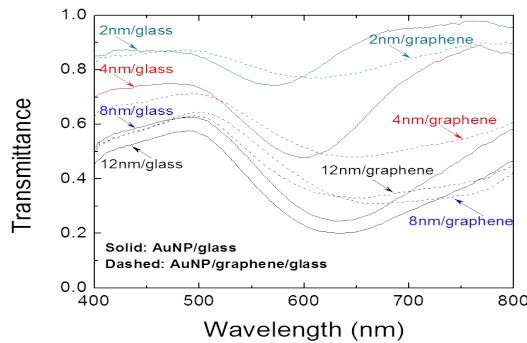


Figure 2.19 Optical transmittance spectra of AuNP/glass (solid curves) and AuNP/graphene/glass (dashed curves) clearly indicating a redshift in the LSPR wavelength with the addition of the graphene layer.

3 Vertically Aligned Carbon Nanofiber Array Experiments

This chapter details the two experiments conducted with VACNF arrays. The first experiment consisted of the conformal ALD coating of VACNF arrays to fabricate VACNF array core-shell structures, which represent a unique 3D nanostructured electrode design. Included is a theoretical overview toward possible application in the design of a solid-state capacitor that may have the potential to reach the same energy and power densities as traditional supercapacitors. The second experiment details the fabrication of a high-power supercapacitor based on mesoporous manganese oxide coatings on vertically aligned carbon nanofibers. The performance of this exceptional supercapacitor is detailed through cyclic voltammetry and EIS.

3.1 ALD Growth on Vertically Aligned Carbon Nanofiber Arrays

Considering that coating of functional materials is such a crucial component for making a VACNF array relevant toward application, this section describes the fabrication of conformally coated double layers on the VACNFs via ALD. As alluded to earlier, ALD was chosen to conformally coat the 3D, high aspect ratio structures because the gas-phase precursors are able to penetrate in between the VACNFs. Noting that the CNFs having exposed graphitic edges down the entire length of the fiber, it is expected that nucleation for ALD film growth would occur without the need for intrusive functionalization as discussed earlier. A simple exposure to water coats the unsaturated, dangling bonds with the required hydroxyl groups (-OH) that easily react with the volatile organometallic precursor, TMA. Figure 3.1⁵³ is a schematic showing the process for forming Al₂O₃ on the CNFs by ALD.

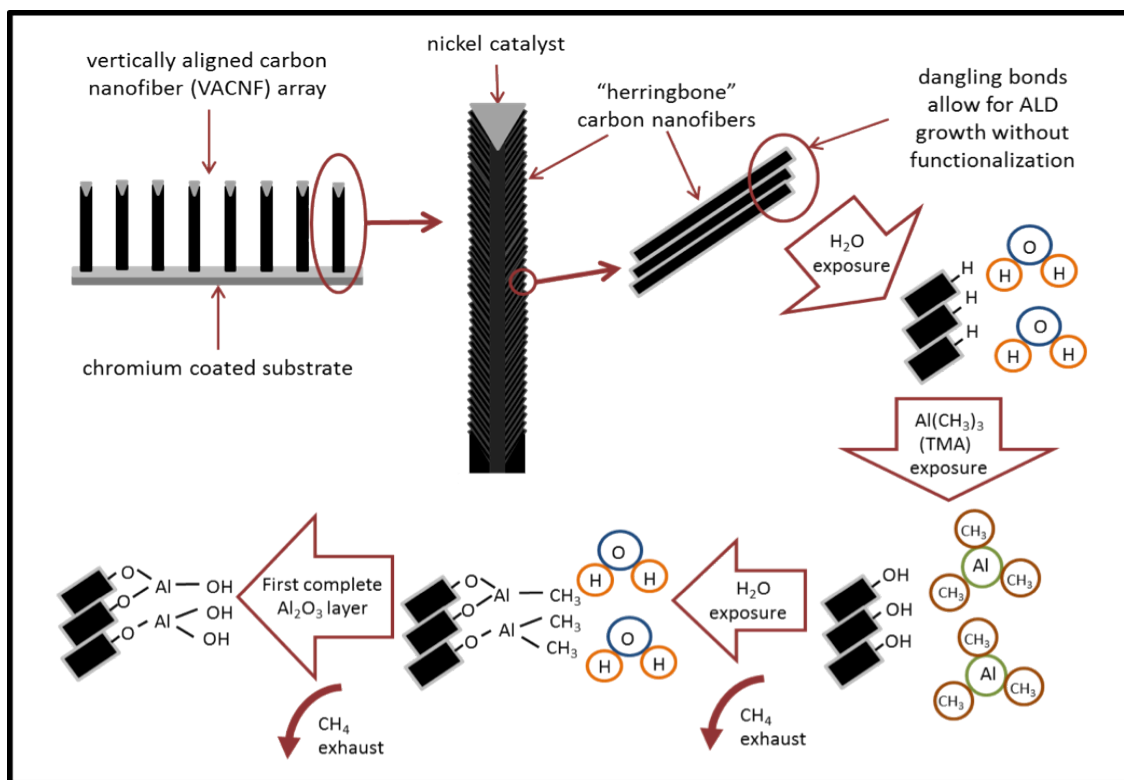


Figure 3.1 Schematic demonstrating one complete Al_2O_3 ALD cycle along the sidewall of a VACNF.

3.1.1 Experimental Details

The VACNF arrays for this experiment and the next were fabricated at Kansas State University in collaboration with Dr. Jun Li's group. The fabrication procedure was similar to the procedures used to produce the VACNF arrays for many previous publications.^{56, 59, 65} For this experiment, the VACNF arrays were grown on $1\text{ cm} \times 2\text{ cm}$ silicon substrates which were all coated with a 100-nm thick chromium barrier layer and then a 22.5-nm nickel catalyst film. The VACNF arrays were grown in a DC-biased PECVD system at $800\text{ }^\circ\text{C}$ utilizing acetylene (C_2H_2 at 63 sccm) and ammonia (NH_3 at 250 sccm) at a pressure of ~ 4.1 Torr. The growth time ranged from 20-30 minutes and produced VACNFs that had an average areal density of $\sim 10^9$ CNFs/ cm^2 , diameters in the range of 50-150 nm, and lengths from 3-5 μm .

All ALD fabrication was accomplished in the custom-build system described in detail in chapter 2. ALD Al_2O_3 films were grown using high-purity H_2O (optima grade, Fisher Scientific) and TMA (semiconductor grade, Akzo Nobel) as the precursors. Ultrahigh purity (99.9999%) N_2 was used as the carrier and purging gas with a maintained flow rate of 5 sccm throughout all cycles. The VACNF array substrates were heated to 200 °C for Al_2O_3 growth via radiant heating of the ALD chamber. ALD cycling began with a one-second H_2O exposure to prepare the graphitic edges with hydroxyl groups for reaction with the TMA molecules. After the initial H_2O exposure, the ALD chamber and gas feeding lines were purged with N_2 for 30 seconds to prevent chemical vapor deposition occurrence during the TMA exposure. Following the N_2 purge, a one-second TMA exposure provided the aluminum atoms that bonded to the hydroxyl group oxygen atoms on the VACNF sidewalls. Another 30-second N_2 purge was then performed to clear the chamber and gas lines of any residual TMA. This process was repeated for a total of 200 cycles with a final exposure of H_2O to end with hydroxyl groups along the sidewalls. The as-grown Al_2O_3 is typically amorphous.³¹ Therefore, in order to improve the crystallinity of the Al_2O_3 layer, a coated VACNF array sample was thermally annealed in a tube furnace at 450 °C for 30 minutes and then cooled to room temperature.

After growth of the Al_2O_3 conformal coating, an additional layer of AZO was grown in order to demonstrate that conformal coating of ALD double layers was possible to produce CNF/ Al_2O_3 /AZO core-shell nanostructures. The ALD AZO was grown with DEZ (research grade, SAFC Hitech) in addition to the same H_2O and TMA precursors that were utilized to grow the Al_2O_3 film. The Al_2O_3 /VACNF array substrates were again heated to 200 °C for the AZO growth. Every run of 200 ALD cycles consisted of 10 supercycles where each supercycle contained 19 cycles of alternating H_2O and DEZ for every one doping cycle of H_2O and TMA.

The single TMA pulse was used in place of every twentieth DEZ pulse in order to achieve a 19:1 Zn/Al as performed by Kong *et al.*⁴⁶ A 19:1 ratio provides the appropriate Al doping concentration of ~2.4% to minimize the resistivity of the AZO film. Additional publications have also verified that the 19:1 cycling ratio and 2.4% Al doping concentration are approximately what is needed in order to achieve optimal ALD AZO conducting films.^{43, 47} During cycling, each precursor exposure was one second with a 30-second N₂ purge in between. Resistivity verification of the AZO film was determined by growing a film on a glass slide that was placed alongside the Al₂O₃/VACNF array during fabrication.

The structure and morphologies of the samples were examined using field-emission scanning electron microscopy (FESEM, FEI Nova SEM 430) at an electron beam accelerating voltage of 3.5 keV. High-resolution transmission electron microscopy (HRTEM) images and selected area electron diffraction (SAED) patterns were obtained using an FEI Tecnai F20 XT field-emission transmission electron microscope at 200 kV. The chemical composition and distribution of the core-shell structures were analyzed using energy dispersive X-ray spectroscopy (EDX). Electrical characterization was conducted on the planar capacitor using a 760D Bipotentiostat (CH Instruments Inc., TX). The specific capacitance was measured by cycling the bias voltage between -0.1 to +0.1 V at various scan rates, and the galvanostatic charge-discharge at selected current densities. The Ohmic resistance across the 20-nm thick Al₂O₃ dielectric layer was measured using AC impedance spectroscopy for further insight.

3.1.2 ALD Growth Confirmation

The custom-build ALD system used for this experiment had previously provided a growth rate of 1.1 Å per cycle for amorphous Al₂O₃, which is less than the lattice constants for crystalline

Al_2O_3 . This growth rate was determined by spectroscopic ellipsometry for Al_2O_3 on SiO_2 -coated silicon utilizing the same growth conditions as mentioned previously.⁸¹ Therefore, after 200 cycles, a thickness of approximately 20 nm was expected.

The AZO growth rate was solely determined by HRTEM imaging. It grew at a rate of approximately 1.7 Å per cycle. This was expected for the 19:1 doping ratio and 200 °C growth temperature and is similar to that mentioned in literature. The resistivity of the 19:1 AZO on glass was approximately $4.2 \times 10^{-3} \Omega \text{ cm}$, which is within the expected values according to previously published results. This resistivity corresponds to a sheet resistance of $1.3 \times 10^3 \Omega/\square$. In addition, this result suggests that aluminum doping of ZnO during the ALD supercycles was sufficient. Unfortunately, these results were not maintained after growth on the Al_2O_3 film. This was originally unexpected but, due to the relationship between the doping ratio and resistivity, not surprising. Considering the AZO film has a low resistivity on glass, it is most likely the case

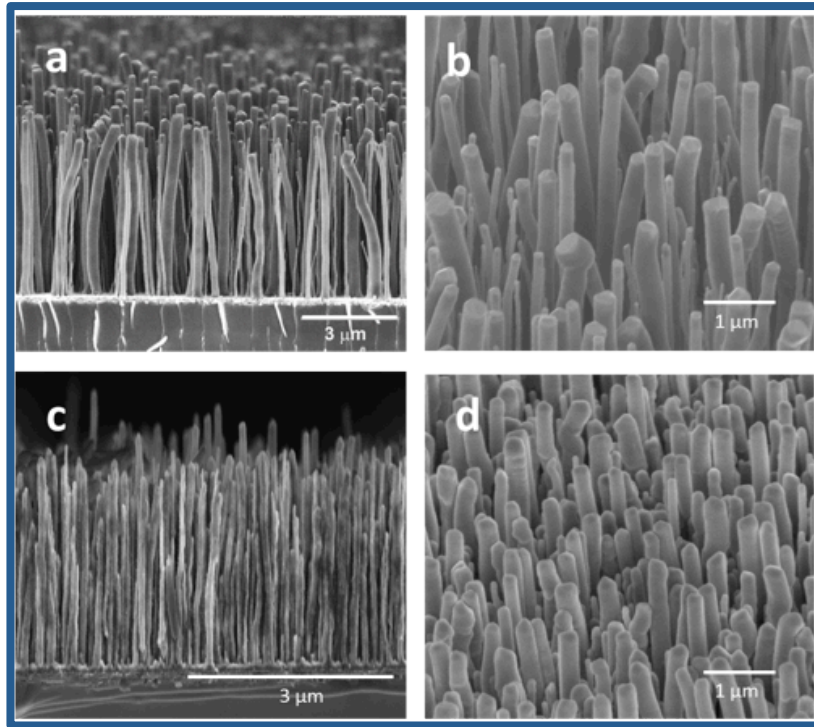


Figure 3.2 FESEM images of VACNF arrays. (a) Side view and (b) 45° perspective view of the as-grown VACNF array with the Ni catalyst slightly visible. (c) Side view and (d) 45° perspective of an Al_2O_3 /AZO coated VACNF array with the Ni tip clearly coated over.

that aluminum atoms diffuse between the $\text{Al}_2\text{O}_3/\text{AZO}$ boundary which caused the resistivity to increase to a level that was not acceptable. In order to remedy the problem, either a much thicker film of AZO needs to be grown, the doping ratio changed, or a diffusion barrier utilized.

FESEM images of as-grown VACNF arrays (Figures 3.2a & b)⁵³ and coated VACNF arrays (Figures 3.2c & d)⁵³ were used for verification of the overall structures. The images do not represent the same VACNF array, but instead were chosen as the best images for each orientation and coating. Therefore, the physical properties are not quite the same but nonetheless close to each other. Each image clearly shows the vertically aligned nature of the CNFs and verifies an approximate areal density of 10^9 CNFs/cm². Furthermore, the images verify the diameters to be in the range of 50 – 150 nm with the heights ranging from 3 – 6 μm . In addition to verifying the physical dimension, the Ni catalyst tip can be observed in Figure 3.2b. It is clearly not visible in Figure 3.2d after growth of the ALD thin films.

Figure 3.3⁵³ shows multiple TEM images of CNFs coated with Al_2O_3 . Figures 3.3a & b consist of a long CNF from the Ni catalyst tip down to the shaft where it broke off of the base. The Al_2O_3 coating appears uniform along the entire CNF. The graphene cone is clearly visible at the bottom of the CNF where it broke off from the main substrate. Figures 3.3c & d show another CNF coated with Al_2O_3 but focus on the Ni tip portion. The higher magnification image in Figure 3.3d clearly indicates that the Al_2O_3 film was ~ 20 nm and coated the entire Ni tip. The final image in the set, Figure 3.3e, contains the highest magnification showing that the Al_2O_3 film was approximately 20 nm along the edge of the CNF. All of the images reveal that the type of CNF used for this experiment was the “herringbone” version with the graphene-stacked cones clearly visible.

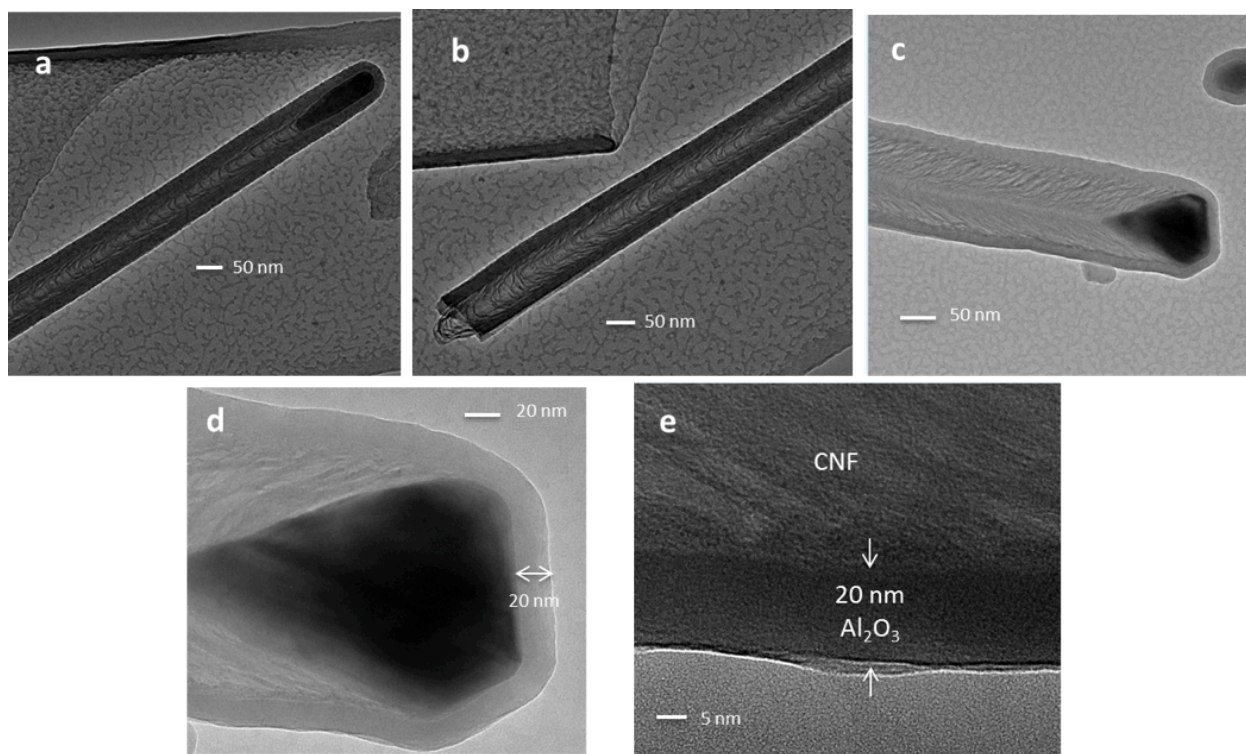


Figure 3.3 TEM images of (a) conformal Al₂O₃ coating along a CNF including the Ni catalyst tip. (b) Conformal Al₂O₃ coating continues down the shaft of the CNF until where it is broken off from the base. (c) Conformal Al₂O₃ coating along another CNF which also shows the “herringbone” nature of the CNF. (d) Close-up of the conformal coating around the Ni tip. (e) Extreme close-up image of CNF core and Al₂O₃ shell.

Since annealing an amorphous structure has been shown to convert it to a polycrystalline form,⁸² a sample coated with Al₂O₃ was annealed to see if it would crystallize on the CNF. Figure 3.4⁵³ consists of HRTEM images along with the electron diffraction patterns for pre- and post-annealed CNFs. For the pre-annealed CNF (Figure 3.4a), there was no diffraction pattern present but only continuous rings (Figure 3.4b) indicating the presence of amorphous Al₂O₃. Only after annealing the coated CNF (Figure 3.4c) in air does a clear ring-like diffusive diffraction pattern form (Figure 3.4d). This ring-like diffraction pattern verifies that the Al₂O₃ layer was now polycrystalline, which may be beneficial for some applications.

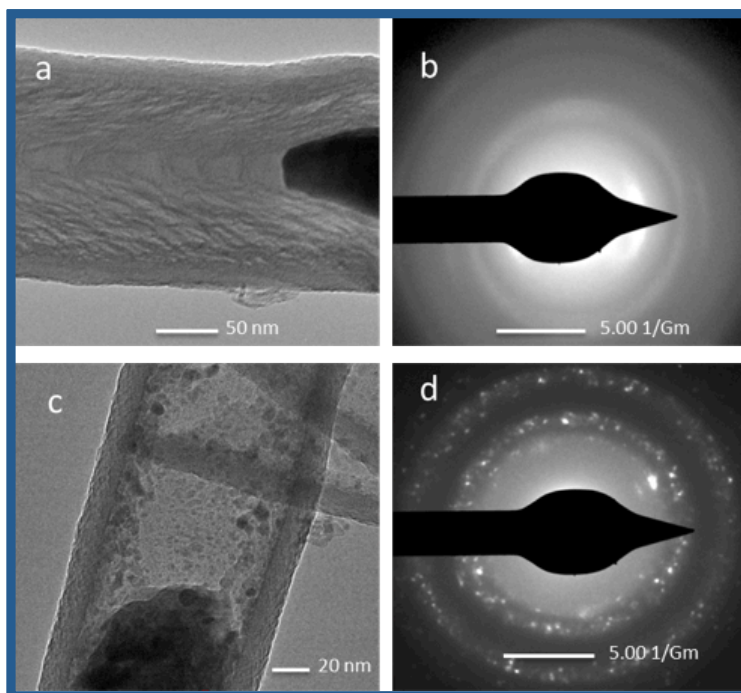


Figure 3.4 (a) Al_2O_3 coated CNF before annealing. (b) No diffraction pattern is present before annealing. (c) Al_2O_3 coated CNF after annealing. (d) Apparent diffraction pattern is present after annealing.

Additional images (Figure 3.5)⁵³ were taken to confirm the growth of AZO on top of the Al_2O_3 film. Figure 3.5a shows three $\text{Al}_2\text{O}_3/\text{AZO}$ coated CNFs with amazing alignment. The tip of each coated CNF clearly reveals the two distinct ALD layers as well as the Ni tip. The total diameter of each coated CNF varies from ~ 180 to 225 nm which is too be expected considering the total thickness of the ALD film is approximately 53 nm as seen in Figure 3.5b. It is also interesting to note that the ALD AZO film appears much rougher than the ALD Al_2O_3 film. This was expected since the Al_2O_3 film grows amorphous while the AZO contains ZnO which grows as nanocrystals.³⁹ Figure 3.5c is a wonderful FESEM image of a coated CNF that broke apart. The graphitic cone of the CNF is clearly visible as well as the $\text{Al}_2\text{O}_3/\text{AZO}$ core shell.

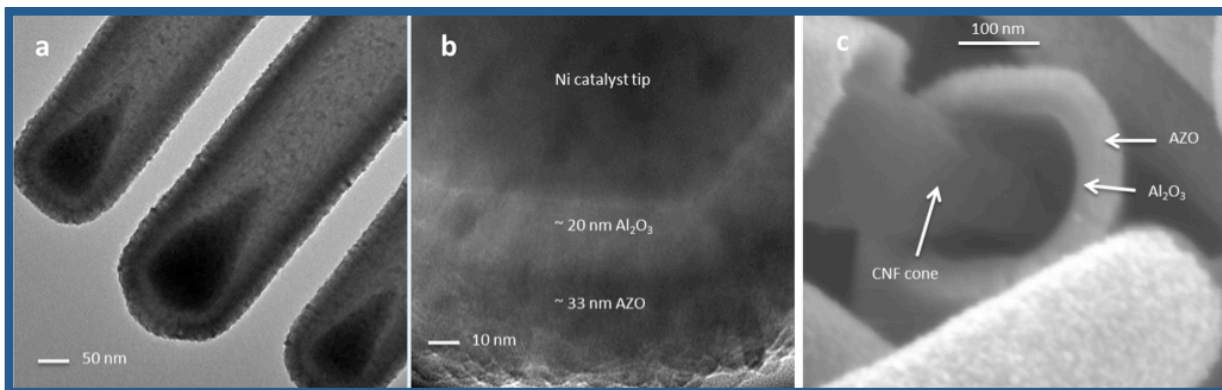


Figure 3.5 HRTEM images of (a) $\text{Al}_2\text{O}_3/\text{AZO}$ conformal core-shell coating of CNFs and (b) close-up of $\text{Ni}/\text{Al}_2\text{O}_3/\text{AZO}$ layering. (c) FESEM image showing CNF graphitic cone as well as the ALD core-shell coating.

In addition to determining the Al_2O_3 film thickness, the chemical composition of the film was verified using EDX (Figure 3.6)⁵³. The core-shell structure shown in Figure 3.6a had an approximate diameter of 165 nm. Once again, the Al_2O_3 film appears to have the expected thickness of 20 nm on each side, leaving the CNF to have a diameter of approximately 125 nm. The elemental count vs. position graph shown in Figure 3.6b was approximately taken along the blue line in Figure 3.6a. This scan clearly reveals that the elements aluminum and oxygen are present, which compose the Al_2O_3 shell. The higher count rate along the edges is to be expected

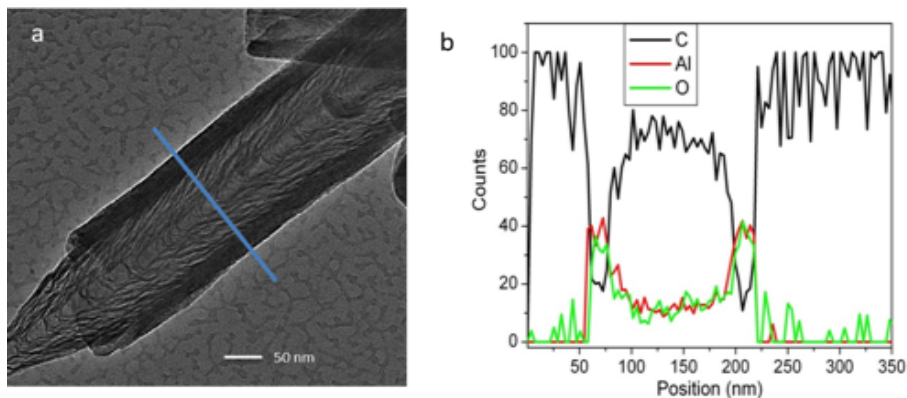


Figure 3.6 EDX elemental analysis. (a) HRTEM image of an Al_2O_3 coated CNF with the blue scan region shown. (b) Elemental count vs. position graph revealing the elements aluminum, oxygen, and carbon.

considering the cross-sectional thickness of Al_2O_3 is greater there than along the middle of the core-shell structure. As the scan moves toward the center of the CNF, the carbon count increases greatly as expected. The carbon count is high outside of the CNF because the TEM grid was carbon-based.

3.1.3 Integrity Verification of ALD Al_2O_3 Film

In order to verify the integrity of the annealed and unannealed ALD Al_2O_3 films, two planar capacitors were fabricated and characterized. The base electrodes for both were comprised of n-doped silicon substrates coated with 100 nm of chromium. After preparation of the base electrodes, 20-nm Al_2O_3 dielectric layers were grown on the chromium surfaces utilizing the same ALD method mentioned previously. One of the samples was annealed in a tube furnace using the same conditions as the VACNF array sample except at a temperature of 400 °C. This lower temperature was chosen in order to eliminate cracking of the film that appeared at the higher temperature. The top electrodes were applied by masking the substrates and then sputtering 600 nm of palladium onto the exposed 2 mm × 2 mm portion of the Al_2O_3 surface. Once fabrication of the planar capacitors was completed, electrostatic measurements were performed to determine the dielectric constants and specific capacitances of each. Interestingly, both capacitors performed similarly. Therefore, discussion of the results will be limited to only the annealed sample.

3.1.3.1 Galvanostatic Charge-Discharge and Cyclic Voltammetry

When an ideal electrostatic capacitor is cycled between two voltage settings, it should display a rectangular shaped I-V curve. The I-V scans consisting of 100, 500, and 1000 V/s shown in

Figure 3.7a⁵³ trace out near perfect rectangular shapes indicating a quality electrostatic capacitor performance. Both the charging and discharging curves are nearly horizontal indicating high Ohmic resistance across the thin Al₂O₃ dielectric film. The small rounded corners, along with the nearly vertical I-V curves at the voltage limits, indicate a low RC time constant and low equivalent series resistance (ESR), which is expected for an electrostatic capacitor.

The approximate area-specific capacitance (C_0) was calculated at each cycling rate using the following equation:

$$C_0 = \frac{I_c - I_d}{2Av} \quad (3.1)$$

where I_c is the charging current and I_d the discharging current at 0 V, v the cycling rate, and A the geometric area of the sandwiched dielectric capacitor. A plot of the area-specific capacitance versus the cycling rate is depicted in Figure 3.7b⁵³. The value is nearly constant for scan rates from 100 V/s to 1000 V/s, indicating the capability of a high power density, which is essential for an electrostatic capacitor and a distinct advantage over electrolytic capacitors.

The area-specific capacitances of the planar capacitors were also determined by galvanostatic charge-discharge cycling at constant current densities. An ideal capacitor shows perfectly symmetric charging and discharging curves with identical time duration. A charge-discharge curve for the annealed planar capacitor at a current density of 12.5 $\mu\text{A}/\text{cm}^2$ is shown in Figure 3.7c⁵³ with duration of ~ 9 milliseconds. A small IR drop can be seen at the beginning of each curve due to ESR ($< 1 \text{ k}\Omega$, mostly due to contact resistance) in the circuit.

The area-specific capacitance was further determined by galvanostatic charge-discharge measurements at each current density, J , using the following equation:

$$C_0 = \frac{J \cdot \Delta t}{\Delta V} \quad (3.2)$$

where Δt is the charge-discharge time interval and ΔV the voltage window. The slowly decreasing trend of the area-specific capacitance vs. current density in Figure 3.7d⁵³ is consistent with the good dielectric capacitive behaviors revealed by cycling I–V measurements in Figures 3.7a and b.

3.1.3.2 Impedance Spectroscopy

To further evaluate the quality of the Al_2O_3 layer in the annealed planar capacitor, electrochemical impedance spectroscopy (EIS) was performed.⁸³ Even though EIS is commonly employed for characterizing electric double-layer capacitors, which contain a liquid electrolyte, the frequency response information from a solid-state capacitor can also be obtained and plotted on a complex plane forming what is called a Nyquist plot. This data can then be fitted with an appropriate equivalent circuit model in order to elucidate more information about the capacitor. For this work, the equivalent circuit model was a Randles circuit that was obtained from the fitted curve to the Nyquist plot. The Randles circuit was used to verify the specific capacitances obtained from cyclic voltammetry. The following is a detailed explanation of this process.

In EIS, an applied sinusoidal potential, V_t , produces a corresponding sinusoidal current response, I_t , that is shifted in phase as follows:

$$V_t = V_0 \sin(\omega t) \quad (3.3)$$

$$I_t = I_0 \sin(\omega t + \phi) \quad (3.4)$$

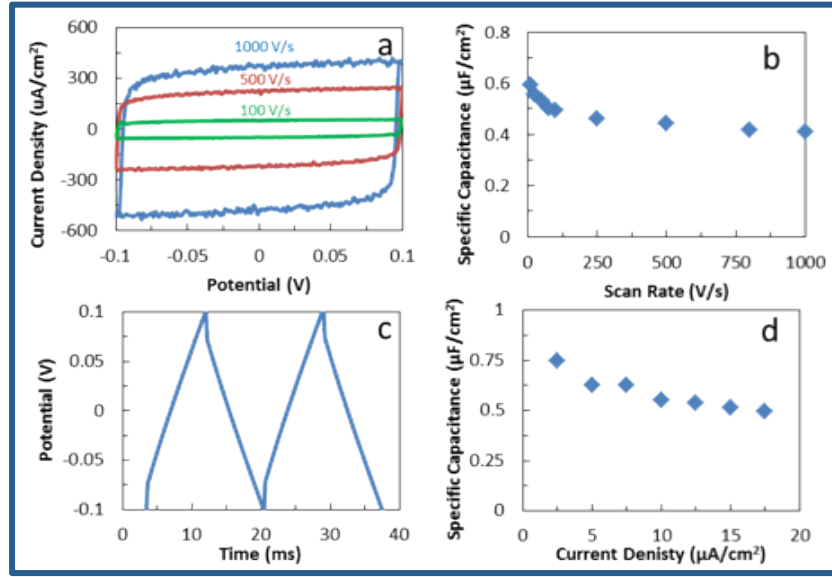


Figure 3.7 Electrical characterization of a planar capacitor. (a) I-V curves measured by cycling the bias voltage between -0.1 to +0.1 V at the rates of 100, 500, and 1000 V/s, respectively. (b) The area-specific capacitance vs. the scan rate derived from the cycling I-V measurements. (c) Galvanostatic charge-discharge curve at a constant current density of 12.5 $\mu\text{A}/\text{cm}^2$. (d) The area-specific capacitance vs. current density calculated from charge-discharge curves.

In these equations t represents the time, ω the radial frequency, and ϕ the phase shift. The current response to an applied sinusoidal potential, being sinusoidal at the same frequency but shifted in phase, is representative of a linear or pseudo-linear system. Therefore, the expressions for V_t and I_t can be used in a linear fashion to determine the impedance of the circuit as shown:

$$Z_t = \frac{V_t}{I_t} = Z_0 \frac{\sin(\omega t)}{\sin(\omega t + \phi)} \quad (3.5)$$

where Z_t , the impedance of the circuit, is expressed in terms of the amplitude Z_0 and phase shift ϕ . Considering a Nyquist plot is obtained on the complex plane, the impedance needs to be converted to a complex relationship. This is accomplished by using Euler's formula.

$$e^{i\phi} = \cos(\phi) + i \sin(\phi) \quad (3.6)$$

The potential can now be expressed as,

$$V_t = V_0 e^{i\omega t} \quad (3.7)$$

and the corresponding current response as,

$$I_t = I_0 e^{(i\omega t - i\phi)} \quad (3.8)$$

The complex impedance can then be written as a function of the phase angle and independent of time. It is determined as follows:

$$Z = \frac{V_t}{I_t} = Z_0 e^{i\phi} = Z_0 (\cos \phi - i \sin \phi) \quad (3.9)$$

This expression for Z is composed of a real part and an imaginary part, and can now be plotted in the complex plane to display a Nyquist plot (Figure 3.8). It is important to note that the vertical axis (imaginary portion) is negative and that each point on the Nyquist plot represents the impedance at one frequency. Since the capacitive reactance of a capacitor is very large (i.e., an

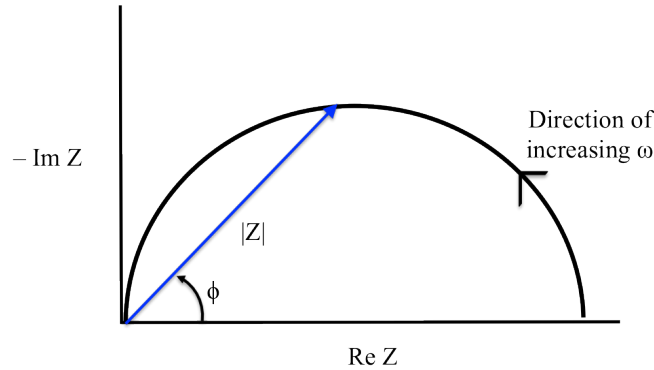


Figure 3.8 A Nyquist plot on the complex plane. The expression for the impedance Z (blue arrow) is composed of a real part and an imaginary part. The direction of increasing frequency is counterclockwise.

open circuit) at low frequencies, and the resistance of a resistor is independent of frequency, the low frequency data starts at the maximum real impedance value and then increases clockwise as shown in Figure 3.8. On the Nyquist plot, the impedance at any specific frequency is represented by the blue arrow of length $|Z|$, and the angle between this vector and the horizontal axis is the phase angle ϕ . A Nyquist plot is beneficial for determining how the impedance of a system changes with frequency, but it is not beneficial for determining the frequency at any specific impedance.

In order to determine more information from the EIS data used to form the Nyquist plot, it can be analyzed in terms of an equivalent circuit model. The shape of an equivalent circuit model's impedance spectrum is determined by its electrical components and how they are connected to each other. Furthermore, the values associated with the electrical components control the overall size of the impedance spectrum. The semicircular shape from a Nyquist plot is indicative of a Randles circuit. A Randles circuit consists of a capacitor and resistor in parallel, which are both in series with another resistor, as shown in Figure 3.9. The resistances for the Randles circuit are easy to determine from the Nyquist plot. The real axis value at the low frequency intercept is the sum of the series resistance, R_S , and the leaking current resistance, R_L .

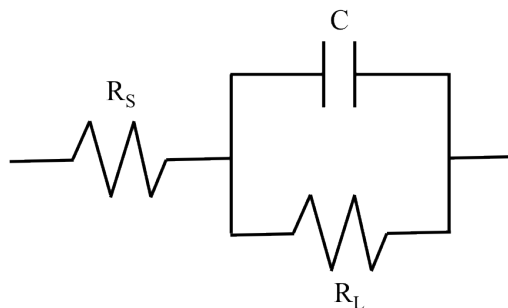


Figure 3.9 Diagram of a Randles circuit with the leaking current resistance in parallel with the capacitance and both in parallel with the series resistance.

Hence, the diameter of the semicircle is equal to the leaking current resistance. If the dielectric material is of good quality, very little leakage current should flow through it and the leaking current resistance should be large. On the other hand, if the capacitor behaves properly at high frequencies it acts as a short circuit. Therefore, only the very low series resistance is obtained.

A Nyquist plot of the annealed planar capacitor for this work, along with the fitted curve using a Randles circuit, is shown in Figure 3.10⁵³. The frequency of the AC voltage bias was varied from 100 kHz to 10 mHz with a fixed amplitude of 5 mV. The fitted series resistance (R_S , or ESR) and leaking current resistance (R_L) were 94 Ω and 7.5 M Ω , respectively. An R_L of 7.5 M Ω indicates very high Ohmic resistance across the annealed Al₂O₃ dielectric film. The semicircle symmetry of the spectrum indicates near perfect electrostatic capacitive behavior and a single time constant. The capacitance determined from the Randles circuit was 1.6×10^{-2} μ F, which translates to a specific capacitance of 0.4 μ F/cm². Utilizing this specific capacitance, a

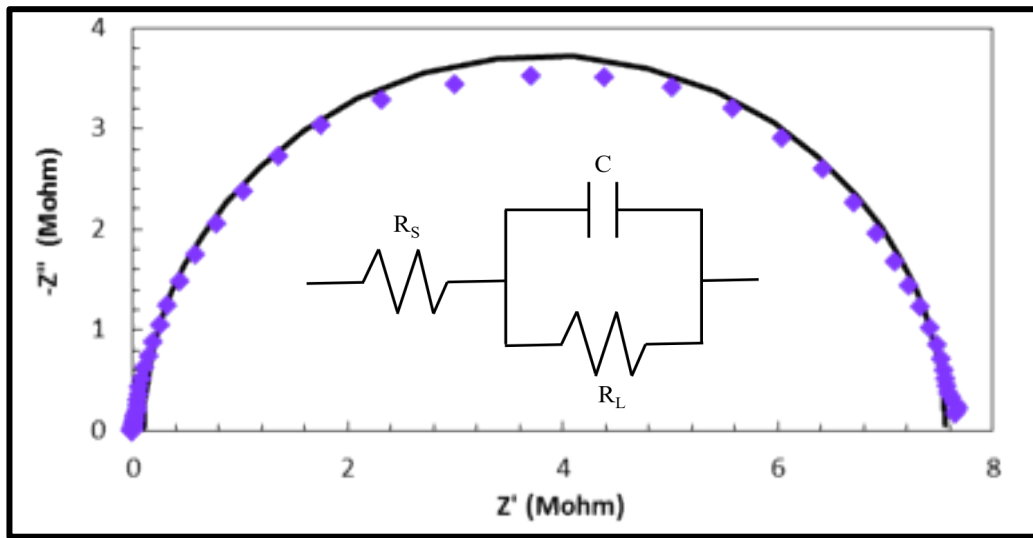


Figure 3.10 The violet diamonds represent the data points of a Nyquist plot for the AC impedance spectrum of the 2 mm x 2 mm planar capacitor, and the black fitted curve represents the associated Randles circuit. The AC frequency was varied from 100 kHz to 10 mHz and the amplitude was fixed at 5 mV. The fitted series resistance (R_S) and leaking current resistance (R_L) were 94 Ω and 7.5 M Ω , respectively, and the capacitance was 1.64×10^{-8} F (i.e. 0.41 μ F/cm²).

dielectric constant of $k \approx 9.3$ can then be determined for the 20 nm thick Al_2O_3 film. This was calculated from the following equation:

$$C_0 = \frac{k\varepsilon_0 A}{d} \quad (3.10)$$

where ε_0 is the vacuum permittivity and d the thickness of the dielectric layer. This value for the dielectric constant of Al_2O_3 is in agreement with the known value of 9.34.⁸⁴ The electrical characterization verified that the ALD Al_2O_3 film was of high quality as expected.

3.1.4 Hafnium Oxide Growth on VACNFs

Despite the difficulties in achieving uniform growth of hafnium oxide (HfO_2) on the VACNF arrays, non-uniform growth was accomplished. The following is a summary of the attempts made and possible reasons that non-uniform growth occurred.

Figure 3.11 contains TEM images of a single CNF after 150 cycles of ALD HfO_2 growth.

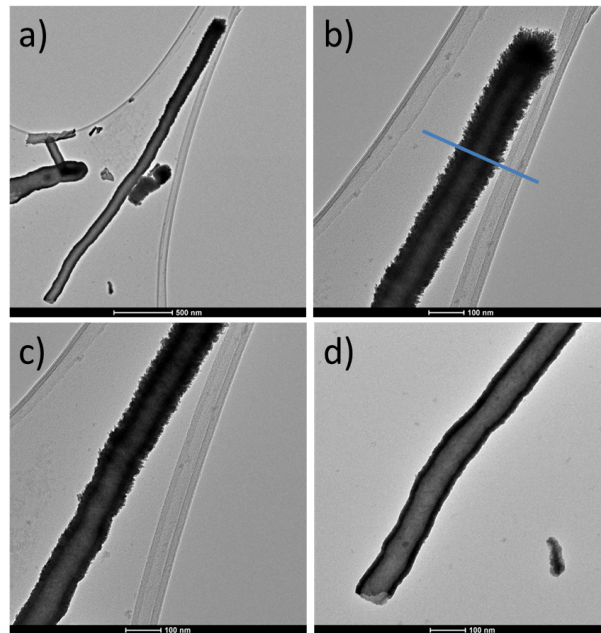


Figure 3.11 TEM images confirming non-uniform HfO_2 growth on CNFs. Image (a) shows the entire length of the CNF down to where it broke off at the base. Images (b), (c), and (d) are all magnified images of (a) with image (b) also revealing the EDX line scan region (blue line).

The growth rate for HfO_2 under the conditions performed should have been between 0.07–0.1 nm/cycle producing a uniform film thickness of from 11–15 nm.^{48, 50, 85} Unfortunately, from these TEM images, it is clear that the HfO_2 coating is non-uniform. Figure 3.11a is an image of the entire CNF until where it broke off at the base. It clearly indicates thicker growth near the tip and thinner growth near the base. Figures 3.11b, c, & d are magnified images of the same CNF at three locations along the shaft. Figure 3.11b indicates that the HfO_2 grew in a brush-like manner with long fibers sticking out near the top. It has a thickness between 30–50 nm. The brush-like nature fades as the growth continues down the shaft with the thickness in Figure 3.11b between 20–30 nm and for Figure 3.11c between 10–20 nm. The variations may be due to steric hindrance of the TEMAH molecule since it is a relatively large in comparison to TMA or DEZ. Furthermore, this growth was attempted on an early version of the custom-build ALD system. For the early versions, the delivery tubing was too long leading to possible TEMAH precursor reaction as it traveled to the chamber and also possible incomplete purging which would allow for CVD growth.

In order to verify that the growth on the CNFs was HfO_2 , EDX elemental analysis was conducted. The blue line marked in Figure 3.11b shows approximately where the line scan was

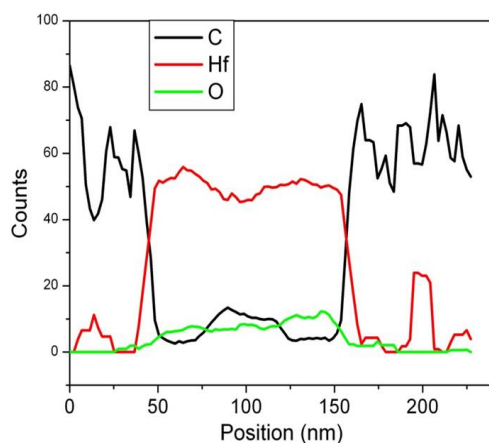


Figure 3.12 EDX elemental count vs. position graph revealing the elements hafnium, oxygen, and carbon. The line scan region is shown in Figure 3.11b.

taken for the EDX results shown in Figure 3.12. It is clear that the HfO_2 was thick as very few carbon counts are indicated in the middle of the scan. Furthermore, if the bump in the middle of the graph represents a CNF with a diameter of approximately 100 nm, then the thickness of the HfO_2 layers on either side of it are approximately 50 nm, which was anticipated by the TEM images.

A later attempt at ALD HfO_2 was performed on an updated version of the ALD system, but this system also had very long delivery lines. This trial consisted of 200 cycles with an anticipated thickness for the HfO_2 film between 14–20 nm. This attempt did not appear to produce the long brush-like fibers near the top, but it still did not produce a uniform coating, as the Ni tip coating looks thicker than the coating near the base (Figure 3.13). The TEM images obtained from these trials did showcase the graphitic cones at the bottom of the CNFs. Of all the TEM images obtained, these were clearly the best images for the graphitic cones of the “herringbone” CNF.

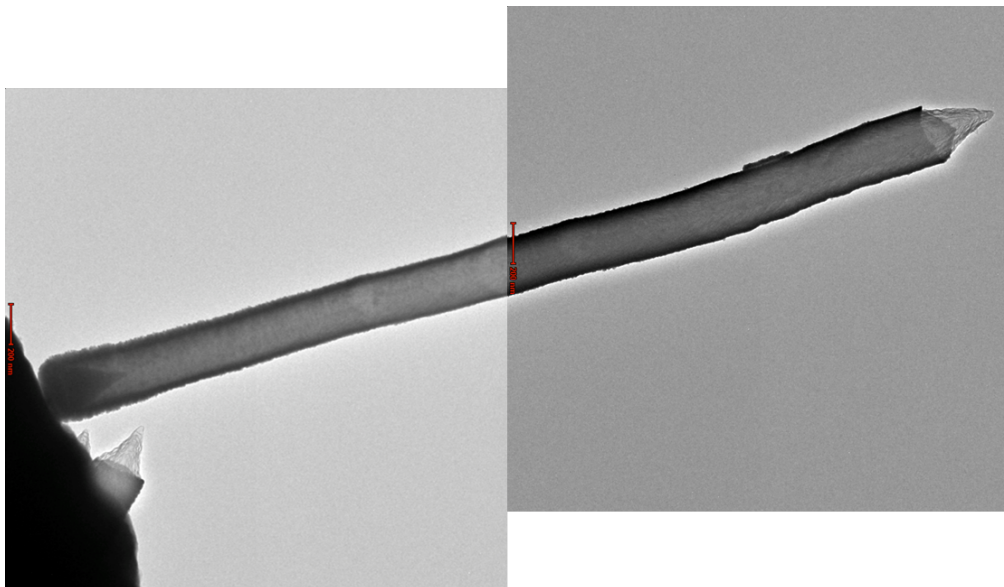


Figure 3.13 Full TEM image of CNF revealing possible CVD HfO_2 growth down the entire shaft until where it broke off at the base. The graphitic cone of the CNF is clearly visible on the right-hand side with some additional graphitic cones revealing themselves on the left-hand side near the nickel tip.

One option that was approached to solve the non-uniform coating problem was to utilize an Al_2O_3 nucleation layer. The first trial did not use a nucleation layer and the second trial utilized 10 cycles of ALD Al_2O_3 growth (~ 1 nm) before conducting the HfO_2 growth. The TEM image in Figure 3.13 did not use a nucleation layer as well as the TEM images shown in Figures 3.14a and b. The TEM images shown in Figures 3.14c and d did have the nucleation layer. Despite this addition, no noticeable difference was observed between all the images. All of them appear to have a growth greater than 20 nm near the tip and the thickness appears to decrease down the shaft toward the base. This thicker growth may have been the result of CVD instead of ALD. Fortunately, the difference in thicknesses between the tip and base of the CNF in Figure 3.14 does not appear to be as extreme as it was in Figure 3.11.

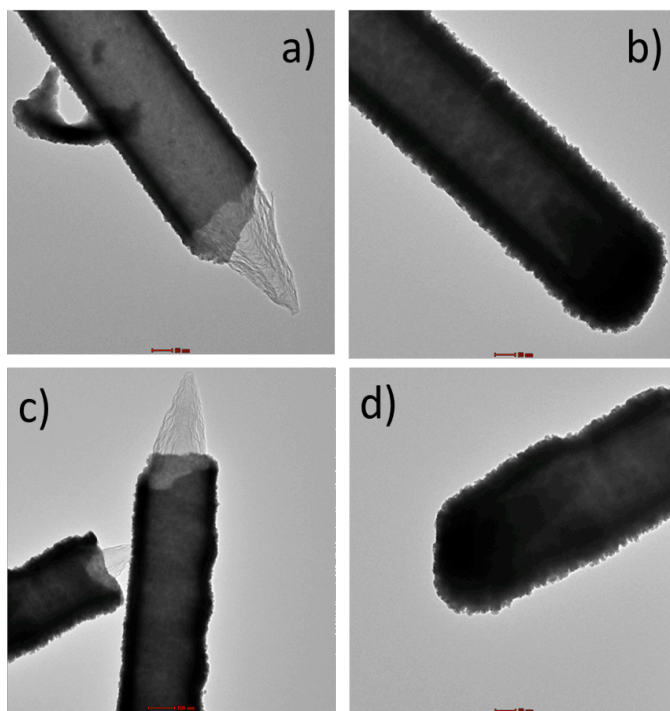


Figure 3.14 TEM images of CVD HfO_2 coated CNFs. Images (a) & (b) did not have an Al_2O_3 nucleation layer while images (c) & (d) utilized a 1-nm Al_2O_3 nucleation layer. Images (a) and (c) clearly reveal the graphitic CNF cones and images (b) & (d) reveal the non-uniform HfO_2 growth.

Further experimentation needs to be performed in order to optimize HfO_2 growth on the present version of the ALD system. The latest version includes much shorter delivery lines than were used for the growth shown here. Furthermore, I have determined that the temperature of the TEMA source needs to be higher than 40 °C but less than 100 °C from the latest trials. Growth attempted at 40 °C produced no film, while growth at 100 °C was too thick. It is thought that the growth at 100 °C was again by CVD because the film thickness was determined to be approximately 50 nm when it was expected to be around 20 nm.

3.1.5 Solid-State Capacitor based on a VACNF Array Core-Shell Structures

Traditional electrolyte-based supercapacitors utilize liquids that are not conducive to extreme high or low temperature conditions. Furthermore, liquid electrolytes slow down charge transport kinetics, which leads to lower scan rates. These two drawbacks are why a complete solid-state design for a capacitor, that can achieve traditional supercapacitor power and energy density results, may be beneficial depending upon the application. A complete solid-state design can operate under a larger temperature window in addition to being able to provide higher scan rates if needed. Additionally, for a complete solid-state device, there would be no liquid electrolyte containment issues.

The original VACNF/ Al_2O_3 /AZO core-shell design was intended to function as a solid-state capacitor as shown in Figure 3.15, but this did not materialize because of diffusion between the Al_2O_3 and AZO layers. Since the AZO doping ratio needs to be maintained for optimal conductivity, any diffusion between the Al_2O_3 /AZO layers that changes the doping ratio will turn the conducting AZO layer into a non-conducting layer. Therefore, the use of a diffusion barrier or alternative conducting material is necessary for proper device fabrication and performance.

Despite the AZO layer not maintaining a conducting nature, the images still provide proof of growth and, hence, the potential for the fabrication of a solid-state supercapacitor device.

A theoretical capacitance per unit area can be estimated by modeling each coated VACNF as a cylindrical capacitor. The dielectric constant determined from the fabricated planar capacitor can be used as well as the approximate dimensions of one average fiber and the thicknesses of the deposited films. A cylindrical capacitor consists of a solid cylindrical conductor of radius a and length L surrounded by a coaxial conducting cylindrical shell of inner radius b as shown in Figure 3.15. The region between a and b is filled with a dielectric material, which in this example is Al_2O_3 . The average diameter of the CNFs was 100 nm so then the average radius would be 50 nm while the average length of each fiber was 4 μm . The radius b is actually the average radius of the CNF plus the thickness of the Al_2O_3 film, which was 20 nm. Therefore, the radius $b = 70$ nm. The capacitance of a cylindrical capacitor is easily derived and given by the following equation:

$$C = \frac{2\pi k \epsilon_0 L}{\ln\left(\frac{b}{a}\right)} \quad (3.11)$$

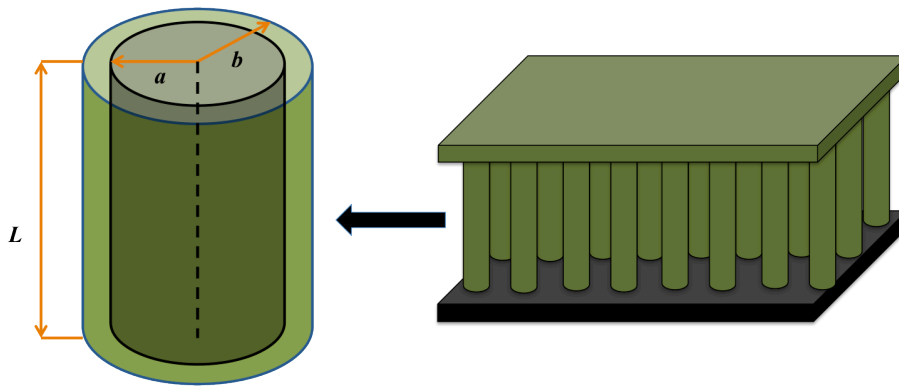


Figure 3.15 Schematic showing an AZO (green) coated VACNF array (black) for use as a capacitor. The enlarged cylinder details the outer radius a , inner radius b , and length L of a cylindrical capacitor. Note that a dielectric medium was not chosen, but ALD Al_2O_3 or HfO_2 could be used.

where k is the dielectric constant of the Al_2O_3 film (~ 9.3) and ϵ_0 is the permittivity of free space. For the values given above, the capacitance for one CNF neglecting the top is $C \approx 6 \times 10^{-15}$ F. Utilizing a maximum areal density of 2×10^9 CNFs/cm², the total specific capacitance would be about 0.12 $\mu\text{F}/\text{cm}^2$ for only the CNFs. Maximizing the growth length to ~ 10 μm , minimizing the dielectric thickness to 5 nm, and replacing Al_2O_3 with HfO_2 ($k \approx 25$) would increase the capacitance for one CNF to $\sim 1.5 \times 10^{-13}$ F. Therefore, the total specific capacitance would reach ~ 0.3 mF/cm².

These values are worthy of note compared to other solid-state designs that have been recently published. For example, Banerjee *et al.* fabricated metal-insulator-metal capacitors based on an anodized aluminum oxide nanopore template coated by ALD.¹⁹ They reported a value of 0.1 mF/cm² at a frequency of 20 Hz for the sample with a pore depth of 10 μm , but for some reason they do not achieve the same equivalent planar capacitance for the sample with a pore depth of 1 μm . For that sample, they only reported a value of 0.01 mF/cm² also at 20 Hz. An additional example was published by Pint *et al.* where they fabricated three-dimensional solid-state capacitors from aligned single-walled carbon nanotube array templates coated by ALD.¹⁷ They achieved an equivalent planar capacitance value up to ~ 0.043 mF/cm² at a frequency of 20 Hz. When they raised the frequency beyond 20 kHz though, the equivalent planar capacitance fell below ~ 0.010 mF/cm². Even though the theoretical value for the equivalent planar capacitance may not turn out to match an experimental value, it is important to predict what would be possible. As can be seen from the reported values in these two examples, a solid-state supercapacitor based on the ALD coated core-shell structure may provide an improvement over other published devices.

3.1.6 Summary and Conclusions

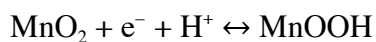
3D VACNF arrays were used as conducting, high aspect ratio substrates for ALD coating of AZO/ Al_2O_3 double layers. HRTEM imaging revealed that the ALD AZO/ Al_2O_3 double layers could form a smooth and conformal shell on VACNF arrays without any pre-functionalization. This uniform growth was achieved along the entire length of the VACNFs from the nickel catalyst tip down to the base. The elemental make-up of the Al_2O_3 core-shell was verified using EDX analysis. HRTEM/SAED images obtained with pre- and post-annealed samples revealed that the Al_2O_3 originally grew in an amorphous state on the CNFs and changed to a polycrystalline state after thermal annealing. FESEM images were also obtained in order to show the vertically aligned state of the CNFs uniformity across the substrate. Electrical characterization utilizing planar capacitors confirmed that the Al_2O_3 dielectric deposited by ALD matched the ideal theoretical behavior. This result is important toward the development of high-performance, solid-state capacitors for energy storage.

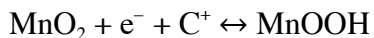
3.2 Mesoporous Manganese Oxide Coating of Vertically Aligned Carbon Nanofibers for a Higher-Power Supercapacitor Electrode

Supercapacitors are frequently divided into two classes: electric double layer capacitors (EDLCs) and pseudo-capacitors. Both types of supercapacitors utilize an electrode/electrolyte interface, but the unique electrode materials and charge storage mechanisms differentiate the two. EDLCs depend on the high surface area of chemically stable electrode materials to store significant amounts of charges at the electrode/electrolyte interfaces. Because the charge is only stored along the electrode/electrolyte interface and does not cross it, EDLCs are able to obtain very quick charge-discharge rates. This, in turn, translates to a larger power density. Activated

carbons are the most commonly used EDLC electrode material due to their extremely high specific surface area ($\sim 3000 \text{ m}^2/\text{g}$) and good electrical conductivity ($2\text{-}20 \text{ S/cm}$).^{16, 86} Conversely, pseudo-capacitors rely on fast, reversible faradaic reactions that are a result of electrochemical charge-transfer processes at or near the surface of the solid electrode materials. Transition metal oxides (e.g. RuO_2 , MnO_2 , TiO_2 , Fe_2O_3 , VOx , etc.) and a family of conducting polymers (e.g. polypyrrole, polyaniline) are most commonly used pseudo-capacitor electrode materials.⁸⁶ The potential charge storage capability for a pseudo-capacitor is much larger than for an EDLC, hence, the specific energy would be much greater. However, due to the reaction kinetics of the faradaic reaction, the specific power is limited and less than that of an EDLC. Much recent research is focused on developing hybrid nanostructured materials for high-performance electrochemical capacitors that blend the high specific surface area and efficient current collection capability of EDLC materials with the fast surface redox reactions of pseudo-capacitor materials so that both a high specific energy and high power rate can be obtained.⁸⁶⁻⁸⁷

Ruthenium oxide (RuO_2) is a common supercapacitor electrode material, but due to its high production cost and environmental toxicity other transition metal oxides are being researched as possible replacements. Manganese oxides (MnOx) have received a lot of attention as a possible replacement due to their abundance, low cost, and benign nature. The theoretical specific capacitance value of MnO_2 is 1370 F/g for a redox process involving one electron per Mn atom, which is comparable to RuO_2 in terms of reaction mechanism. MnO_2 is also similar to RuO_2 with its pseudo-capacitance behavior. Both follow the same proton or alkali metal cation (C^+) insertion into the lattice structure during reduction processes as follows:





where C^+ is either K^+ , Na^+ , or Li^+ . In addition, MnO_2 has a greater diffusion coefficient than RuO_2 , but it also has a lower electrical conductivity.

Unfortunately, despite some similarities to RuO_2 , MnO_2 has not been able to perform as well as RuO_2 as a pseudo-capacitance material. The highest reported specific capacitance so far is 1380 F/g at a very low scan rate of 5 mV/s. This low scan rate is not practical in application and would not allow MnO_2 to replace RuO_2 . However, if the active surface area can be increased while also improving the electrical conductivity through the MnO_2 material all while maintaining the integrity of the electrode to endure tens-of-thousands of charge-discharge cycles MnO_2 may be able to replace RuO_2 as a pseudo-capacitance material.

In this work, manganese oxide (MnO_2) coated VACNF arrays were used as electrodes in the development of a 3D core-shell architecture for high-power energy storage devices.⁸⁸ For this experiment, ALD was not utilized, but instead the VACNFs were coated with Mn by DC sputtering and then electrochemically oxidized in sodium sulfate (Na_2SO_4). This produced a mesoporous MnO_2 structure that provides an improved electrode/electrolyte interface, which allows protons and cations greater access to the whole MnO_2 material. This lowers diffusion rates since the ions do not have to pass through as much solid MnO_2 material since the ion diffusion length across the resulting MnO_2 material is less than ~10 nm. The result of such a design is a faster reaction rate that leads to a higher power density. The structural characterization for this design was accomplished by SEM and TEM imaging, and electrical characterization was performed by cyclic voltammetry and EIS.

3.2.1 Experimental Details

An oxygen-free titanium foil with a thickness of 25 μm (Titanium Grade 2, Hamilton Precision Metals, PA) was cut to a 15 cm x 15 cm sheet. A 300 nm thick chromium barrier layer followed by a 30 nm nickel catalyst layer were deposited using a high-vacuum Perkin Elmer 4400 series magnetron sputtering system at UHV Sputtering Inc. (Morgan Hill, CA). This Ni/Cr/Ti sheet was then cut into disks of 18 mm in diameter for test cell use. VACNFs with an average length of 5.0 μm , average diameter of 150 nm, and areal density of $\sim 1.1 \times 10^9$ CNFs/ cm^2 were grown on the Ti foils using a DC-biased PECVD system (AIXTRON, CA).

Pure Mn (99.95%, ACI Alloy) was deposited on the individual disks of VACNF arrays using a custom-built sputtering chamber. The substrate was mounted in an on-axis configuration relative to the two-inch sputtering gun. Before Mn deposition, the chamber was flushed with UHP N_2 (99.999%) and then pumped down to a base pressure of $\sim 10^{-6}$ Torr. It was then filled with UHP argon gas (99.999%) to a pressure of approximately 20 mTorr. The Mn target was pre-sputtered for three minutes to expose a fresh surface. Sputtering was conducted at room temperature with a power of 48 W and at a rate of approximately 0.67 nm/s as determined by profilometry (KLA Tencor P-16 Profiler). The nominal thicknesses of deposited Mn (equivalent to the film thicknesses on a flat surface) were 100, 200, 300, and 600 nm.

The cycling tests of the Mn-coated VACNF arrays were performed using a Teflon cell sealed against the Mn-coated VACNF array with an O-ring, leaving a total area of 1.39 cm^2 exposed. The electrolyte for this experiment was 1.0 M Na_2SO_4 solution prepared with 18.2 M Ω deionized water. All measurements were conducted in a three-electrode configuration in 6.0 mL of electrolyte with the Mn or MnO_2 -coated VACNF array as the working electrode, an Ag/AgCl (4 M KCl) reference electrode, and a Pt foil counter electrode. The initial Mn coating was

oxidized by the chronopotentiometry method from an open circuit potential (-1.3 V) to the maximum potential of $+0.9$ V vs Ag/AgCl (4 M KCl) reference electrode. The electrolyte was quickly replaced with new solution after oxidation and CV measurements were then performed from 0.0 V to 0.8 V with a scan rate varying from 1 mV/s to 2000 mV/s. Chronopotentiometric charge/discharge tests were performed at various currents from 0.28 A/g to 140 A/g (44.2 μ A to 22.5 mA total). EIS measurements were performed from 100 kHz to 10 mHz, at an amplitude of 5.0 mV and a bias of 0.4 V. All electrochemical measurements were conducted with a CHI 760D Electrochemical Workstation (CH Instruments, *Austin, TX*). The structures of the electrodes, before and after electrochemical testing, were examined by SEM (FEI Nano 430) and TEM (FEI Tecnai F20 XT).

3.2.2 Structural Characterization of MnO₂-VACNF Array Electrodes

Figures 3.16c–f⁸⁸ are SEM images of the sputtered Mn-coating on the VACNF array before and after electrochemical oxidation. The Mn sputtering process appears to form a thin film of Mn particles (Figures 3.16c and e), with a shell coating in the range of 10 – 40 nm thick for the samples of 100 nm nominal thickness and up to 200 nm thick for the larger samples of 600 nm nominal thickness (Figure 3.17)⁸⁸. These Mn particles are well distributed around the CNF cores, appearing not to have followed any model of deposition, but are noted to be larger near the fiber's tip where Mn flux is greatest during deposition (Figures 3.17b, 3.17e, and 3.17h). The larger particles appear crystalline in-nature, with sizable facets and lattice edges; broken up by small crevasses that penetrate deep to the core, which provide numerous surfaces for the electrolyte to interact and create active oxidation sites for MnO₂ formation. A uniform method of coating would be beneficial considering the entire CNF surface would be utilized, but ALD was

not chosen as the deposition technique because growth of Mn is presently not possible by ALD and the growth of MnO_2 directly would be too dense for ion diffusion.

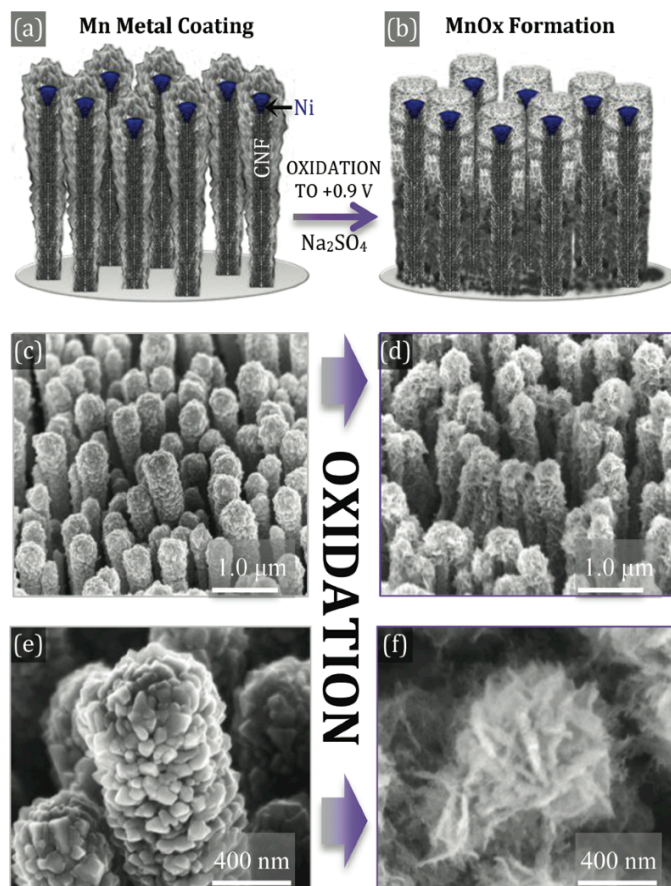


Figure 3.16 Schematic of Mn-coated VACNFs (a) before and (b) after electrochemical oxidation in 1 M Na_2SO_4 . Representative SEM images of 300 nm nominal Mn thickness at different magnifications with (c) & (e) before oxidation and (d) & (f) after oxidation.

The Mn-coated VACNF electrodes were then oxidized in galvanostatic mode by applying a current density of $127 \mu\text{A}/\text{cm}^2$ ($177 \mu\text{A}$ total) starting at an open circuit potential of about -1.3 V. The electropotential was monitored with chronopotentiometry until reaching the upper limit at $+0.9$ V. The oxidized Mn shell appeared to expand for all of the coated VACNFs, with very intricate dendrites that resembled rose petals indiscriminately arranged on the VACNF sidewall (Figures 3.16d, 3.16f, and 3.18)⁸⁸. Such MnO_2 shells are highly porous, with very thin walls (~ 20 nm) extending out radially from the CNF core, forming a large expanded shell with cavernous pores across the whole MnO_2 layer. The 100 nm nominal coating showed a coarser structure, with large thick petals (Figures 3.18a-d), while the 600 nm coatings are more ornate with thinner and more convoluted petals (Figures 3.18i-l). The high porosity of the MnO_2 shell is expect to

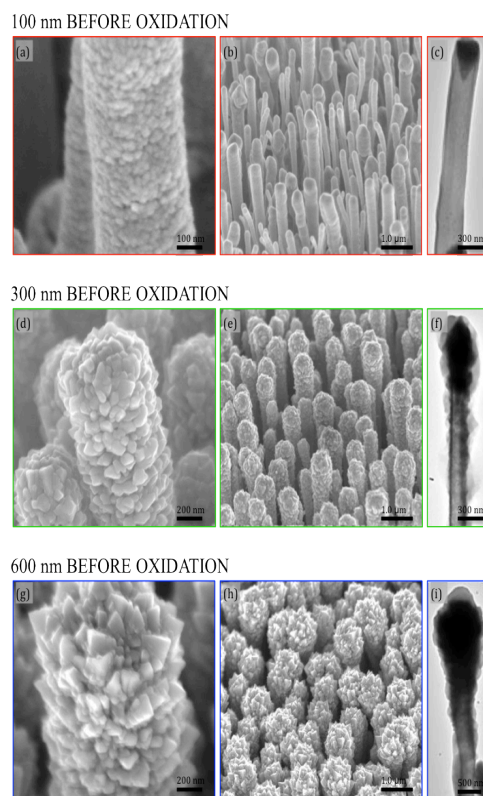


Figure 3.17 SEM and TEM of the Mn-coated VACNFs after Mn sputtering to various nominal thicknesses of 100, 300, and 600 nm. Scale bars are 100 nm, 1.0 μm , 300 nm; 200 nm, 1.0 μm , 300 nm; 200 nm, 1.0 μm 500 nm, for the 100 nm, 300 nm and 600 nm samples, respectively.

significantly improve the power density since ions can access the whole MnO_2 film faster through diffusion in electrolyte solution and only need to transport less than 10 nm across the solid MnO_2 material from both sides of the petal plane.

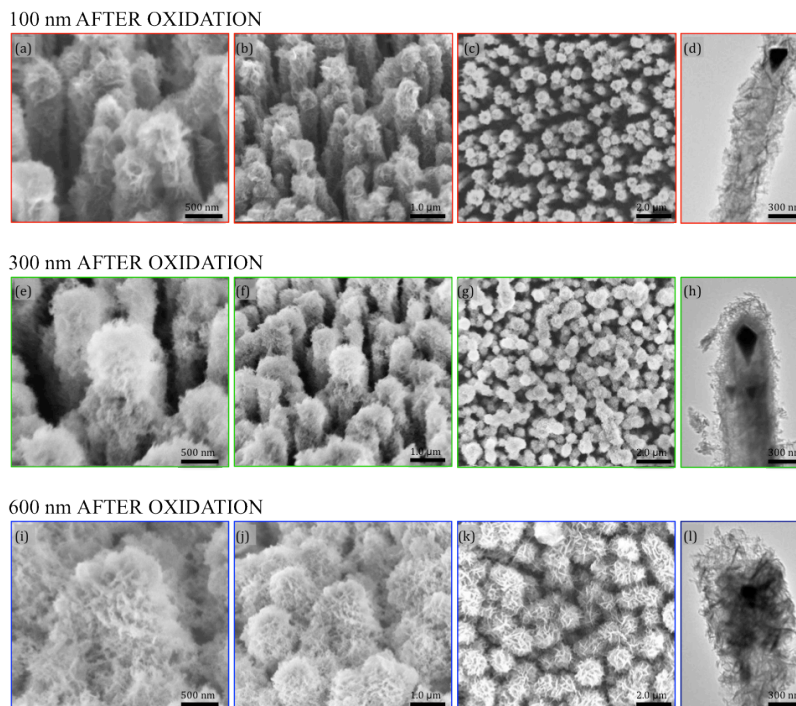


Figure 3.18 SEM and TEM images of the MnO_x -coated VACNFs after oxidation and cycling characterization. The images are shown with respect to their various nominal thicknesses of 100, 300, and 600 nm. Scale bars are 500 nm in panels (a), (e) and (i); 1.0 μm in panels (b), (f) and (j); 2.0 μm for panels (c), (g) and (k); and 300 nm in panels (d), (h) and (l), respectively, for each thickness.

3.2.3 Electrochemical Performance of MnO_2 -VACNF Array Electrodes

After oxidation, cyclic voltammetry was performed from 0.0 V to 0.8 V at scan rates varying from 1 mV/s to 1000 mV/s. Figure 3.19⁸⁸ shows a comparison in the I-V curves of the four samples at scan rates of 1, 10, 100, and 1000 mV/s. At both low and high scan rate, all four samples exhibit good capacitor behavior in forming a symmetrical rectangular loop that shows a small time constant (represented by the small rounding corners as the polarity is reversed). The MnO_2 redox peaks are not observed distinctly, implying that the electrodes behave as faradaic

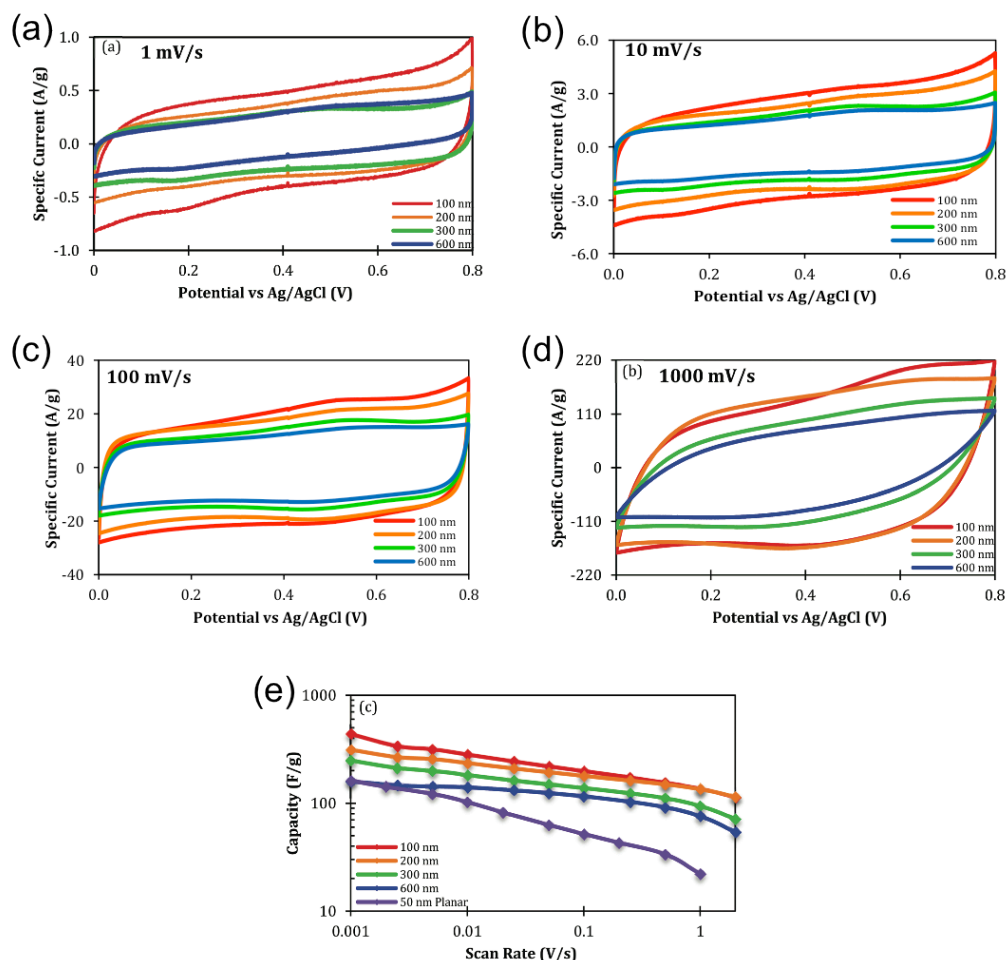


Figure 3.19 I–V curves by cyclic voltammetry for Mn-coated VACNF electrodes with nominal thicknesses of 100, 200, 300, and 600 nm, performed at the scan rates of (a) 1 mV/s, (b) 10 mV/s, (c) 100 mV/s, and (d) 1000 mV/s. (e) The specific capacity versus the scan rate for various nominal thicknesses. The curve labeled as “50 nm Planar” is measured with a control sample of 50 nm thick planar Mn film deposited on a flat Cr-coated Si wafer.

pseudo-capacitors whose voltammograms consist of many fast and reversible successive surface redox reactions overlapping with each other. This is also supported by EIS which shows a steep rise along the imaginary axis, low charge-transfer resistance, and negligible series resistance ($< 2 \Omega$) (Figure 3.20)⁸⁸. In general, the specific capacitance monotonically decreases as the nominal Mn thickness is increased (Figure 3.19e). At the 1 mV/s scan rate, the 600 nm sample provided 162 F/g, while the 100 nm sample achieved a notable 437 F/g. Increasing the scan rate up to

1000 mV/s only caused the specific capacitance value to descend to 76 F/g and 135 F/g, respectively. In comparison, the control experiment with a planar 50 nm thick Mn film on Cr-coated Si wafer only matches the specific capacitance value of the worst sample (600 nm nominal thickness) for all Mn-coated VACNFs at 1.0 mV/s, but decreased significantly to 22.1 F/g at 1000 mV/s (Figure 3.19e). This result illustrates that the nanoscale architecture provided by the VACNF array is indeed critical to the better performance.

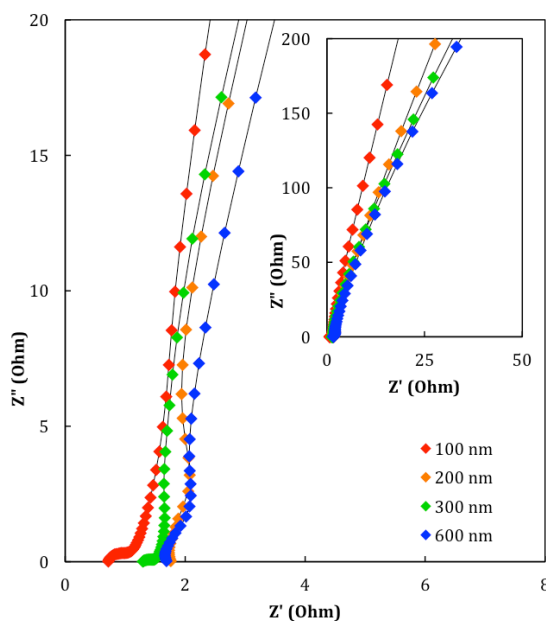


Figure 3.20 Nyquist plot from impedance spectroscopic analysis of the MnO_2 -coated VACNFs with the inset showing the full region.

The charge-discharge capability at high current densities is one of the most important factors in the development of new electrodes for supercapacitors. Following cyclic voltammetry, a series of chronopotentiometric measurements were performed (Figure 3.21)⁸⁸. Figure 3.21a shows the rate capability of the 300 nm nominal thickness electrode at three different current rates: 0.28 A/g, 2.78 A/g, and 27.8 A/g. The nearly linear and symmetric features of the voltage profiles suggest good capacitance behavior of the MnO_2 -coated VACNF arrays. The corresponding

specific capacitance values are 246, 171, and 97 F/g. Hence, the specific capacitance value only dropped by about a factor of 2.5 as the current density was raised by a factor of 100, indicating the high reaction rate which matches the high current density.

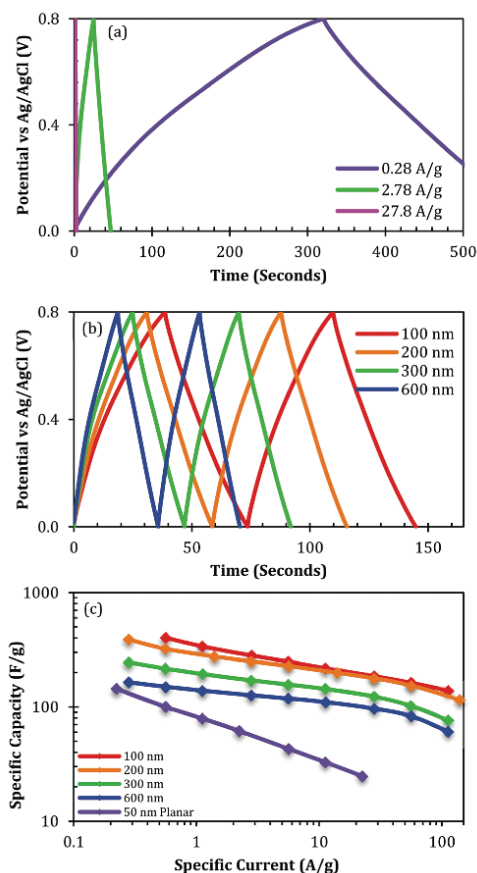


Figure 3.21 Chronopotentiometric cycling profiles of Mn-coated VACNF electrode with (a) 300 nm nominal thickness at 0.28 A/g, 2.78 A/g, and 27.8 A/g and (b) comparison of varied nominal thickness of 100, 200, 300, and 600 nm at 2.78 A/g. (c) Log-log curve of specific capacitance versus specific current rate for various nominal thicknesses.

Fig. 3.21b shows the charge-discharge curves at 2.78 A/g for the four samples with 100, 200, 300, and 600 nm nominal Mn thicknesses. Similar to the cyclic voltammetry measurements, the specific capacitance value gradually decreases as the thickness of MnO_2 is increased, achieving a capacitance of 250 F/g for the 100 nm nominal thickness electrode, decreasing to

127 F/g for the 600 nm nominal thickness electrode. This reveals that while mass loading increases, the thicker MnO₂ shell was not fully utilized. However, even the sample with 600 nm nominal Mn thickness was able to achieve a specific capacitance of 61 F/g at an extremely large current of ~110 A/g (Figure 3.21c). Overall, the MnO₂-coated VACNFs at lower nominal Mn thicknesses consistently show higher specific capacitance values that drop slower at high current density.

All energy storage devices can be categorized by their specific power (W/kg) and specific energy (Wh/kg) capabilities. When these values are plotted as specific power versus specific energy (i.e., also known as a Ragone plot) it reveals the true performance of the device (Figure 3.22)⁸⁸. For a single supercapacitor electrode, the maximum specific energy is related to the specific capacitance, *C*, of the capacitor and the maximum potential, *V*, between the two electrodes by the following equation:

$$E_0 = \frac{1}{2} CV^2 \quad (3.12)$$

However, for a full cell consisting of two identical electrodes, the specific energy is represented by the following equation:

$$E_{0,full\ cell} = \frac{1}{8} CV^2 \quad (3.13)$$

Furthermore, the specific power, *P*₀, of a supercapacitor represents the maximum power output. It can be calculated by the following equation:

$$P_0 = \frac{V^2}{4\ m\ ESR} \quad (3.14)$$

where m is the total mass of MnO_2 on both electrodes and ESR is the equivalent series resistance determined by the voltage drop after the current polarity is flipped during the charge-discharge processes.

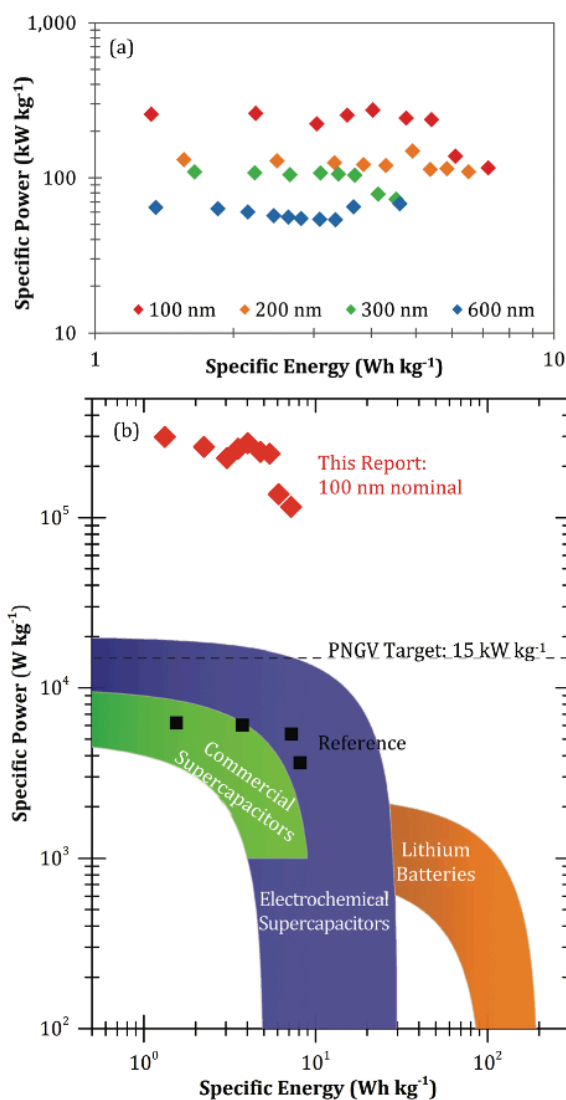


Figure 3.22 Ragone plots of Mn-coated VACNF electrodes (a) at the nominal Mn thicknesses of 100, 200, 300, and 600 nm; and (b) at 100 nm nominal Mn thickness (red diamonds) with comparisons to values achieved in previous work (black squares), and the range seen for commercial & state-of-art supercapacitors as well as lithium batteries. The black dashed line represents a target in specific power proposed by Partnership for a New Generation of Vehicles (PNGV)

It is interesting to see in Figure 3.22a that as the current density was varied from 0.28 A/g to 28 A/g in galvanostatic charge–discharge, the specific power P_0 remained nearly constant. This indicates that the change in ESR is negligible in this wide current density range. This is quite different from common supercapacitors. As shown in Figure 3.22b, while the specific energy in this study is between 1 to 10 Wh/kg, comparable to commercial supercapacitors⁸⁹ and compact MnO₂ shells on VACNFs in our own previous study,⁵⁹ the specific power is more than one order of magnitude higher than the other studies (Figure 3.22b), reaching 240 kW/kg for the 100 nm nominal thickness and over 70 kW/kg for the 600 nm nominal thickness. This greatly surpasses the target in specific power of 15 kW/kg (but including the whole system), proposed by the Partnership for a New Generation of Vehicles (PNGV).⁹⁰ The high-power capability can be attributed to the improvement of ion diffusion through the electrolyte penetrating into the mesoporous MnO₂ shell in the hybrid structure. The specific energy, however, is limited by the low electrical conductivity that prevents effective electrical connection to the outer shells. Improving Mn coating by coating it more uniformly along the VACNFs (i.e., possibly by ALD) and incorporating an additional conductive polymer (or carbon) coating at the electrolyte/MnO₂ interface may enhance the specific energy in future studies.

3.2.4 Summary and Conclusions

Sputtered Mn shells were coated on VACNF arrays and then electrochemically oxidized to form rose-petal-like mesoporous MnO₂ layers. The 3D MnO₂/VACNF array hybrid architecture provides enhanced ion diffusion across the mesoporous MnO₂ shell and yields excellent current collecting capability using the conductive VACNF core, both required for high-performance supercapacitors. Enhanced ion diffusion along with higher electron and ion transport collectively

enabled the fast redox reaction in thick MnO_2 shells up to 200 nm during charge–discharge processes in 1 M Na_2SO_4 electrolyte. More than one order of magnitude higher specific power (~ 240 kW/kg) was obtained with such a hybrid electrode material as compared to the state-of-the-art supercapacitors based on other MnO_2 structures at the similar specific energy range (~ 1 to 10 Wh/kg). This design strategy clearly demonstrates the remarkable capability of using VACNF core structures as a template for high-powered energy storage devices.

3.3 High Power Battery-Pseudocapacitor Hybrid

A project related to the mesoporous MnO_2 supercapacitor electrode was also conducted in conjunction with Dr. Jun Li's group at Kansas State University, and this research resulted in a recently submitted manuscript that is presently under review.⁹¹ This study reports on an electrochemical cell that behaves like a battery-supercapacitor hybrid based on lithium ion (Li^+) chemistry using a silicon (Si) anode and a titanium dioxide (TiO_2) cathode also referred to as a full cell (Figure 3.23)⁹¹. Both electrode materials were fabricated as coaxial shells with an oblique nanocolumnar structure anchored onto vertically aligned carbon nanofiber arrays. A full cell, containing similar volumes of silicon and titanium dioxide, shows a high specific energy (103 Wh/kg) at low current rates comparable to a decent battery, and a remarkable specific power (56,000 W/kg) at high current rates matching the state-of-the-art supercapacitors. Therefore, continued research in this area may lead to the development of an energy storage device with a high power density and large energy density.

An ideal electrochemical energy storage system would contain a large energy density while also having a maximum power density. Presently, lithium ion batteries (LIBs)⁹² represent the best-known energy density device, while electrochemical supercapacitors⁹³ represent the best-

known power density device. Unfortunately, due to the mechanisms that provide either the large energy density or large power density, they cannot be combined into one system without sacrificing either a significant loss in energy density or power density. LIBs have a very large energy density due to the large amount of Li involved in intercalation or by allowing reactions to occur in the bulk electrode material. However, their power density is low because of the slow Li^+ diffusion in solid materials.⁹² In contrast, electrochemical supercapacitors, particularly pseudocapacitors, can charge and discharge at much higher rates than LIBs based on fast electrochemical reactions that occur at the electrode surface or in a thin layer near the surface. However, since only the surface or a thin layer near the surface is involved in the chemical reactions, the energy density of a supercapacitor is much lower in comparison to an LIB.⁹³⁻⁹⁴

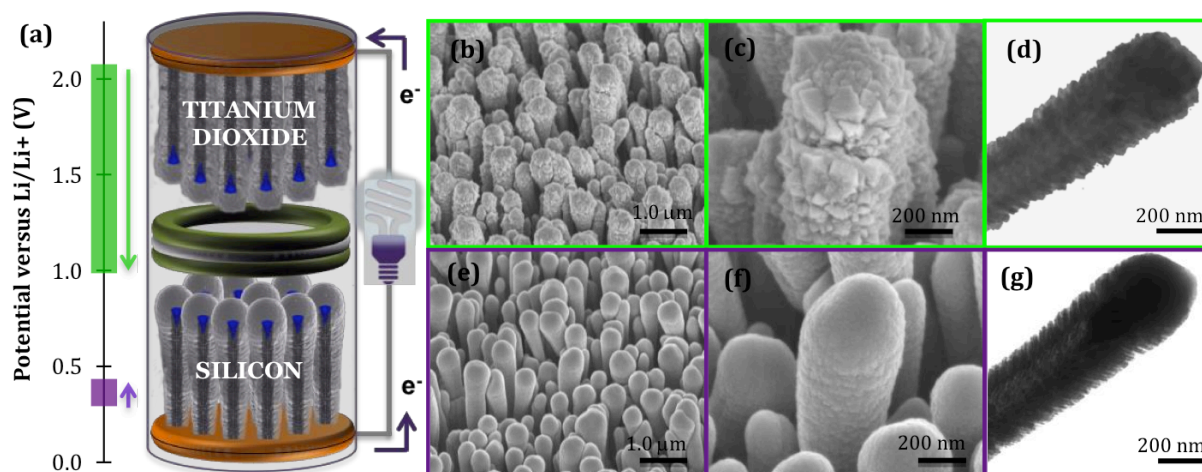


Figure 3.23 (a) Illustration of the full cell consisting of a prelithiated anode made of Si-coated VACNFs and a cathode made of TiO_2 -coated VACNFs, both grown on copper foils. The expected operating potentials of each electrode during cycling are shown to the left, with arrows pointing the direction of potential change of individual electrodes during discharge. The structures of the as-prepared electrode materials at various scales are revealed by SEM and TEM images in (b-d) for TiO_2 -coated VACNFs and (e-g) for Si-coated VACNFs.

An extensive amount of research has been conducted for LIBs in order to decrease the Li^+ diffusion length to tens of nanometers in the active materials. By doing so, the reaction kinetic rates would decrease leading to a higher power density.^{16, 95} Furthermore, the fast surface reactions lead to higher power properties similar to a pseudo-capacitor.^{16, 95} However, if the nanoparticle size is decreased to this scale, there is evidence that the Li storage capacity as well as the specific energy would significantly decrease.^{94, 96} Therefore, designing nanostructures that can obtain the optimal balance required for achieving a large energy density as well as a high power density is a challenging problem. In this work we detail a unique 3D architecture based on vertically aligned core-shell nanofibers in order to achieve a large energy density with a corresponding high power density for an electrochemical energy storage device.

LIBs contain two different types of electrodes that operate between a large potential difference. Silicon has been extensively studied⁹⁷⁻⁹⁹ as a potential anode material due to its low Li insertion/extraction potential ($\sim 0.3\text{-}0.6$ V vs Li/Li^+) and excellent specific capacity (with 4,200 mAh/g theoretical limit for crystalline Si and 3,800 mAh/g for amorphous Si at room temperature).¹⁰⁰ However, since bulk Si materials have suffered from poor stability due to mechanical failure caused by large volume expansion (by $> 300\%$) during lithiation,¹⁰⁰ tremendous efforts have been made toward developing various nanostructures to alleviate this problem.^{98, 101-103} An additional advantage of nanostructured Si materials is that their larger surface area and shorter Li^+ diffusion length help to improve the rate performance.^{11, 98, 104} Hybrid core-shell structures utilizing highly conductive nanotubes as the stable cores to support thin Si shells have further demonstrated the ability for providing high specific capacity and good cycle stability around the normal C-rates of C/1 (i.e., completing the charge/discharge process in 1 hr).¹⁰⁴⁻¹⁰⁹ Recently, Dr. Li's group has demonstrated the use of a core-shell structure composed

of co-axial Si shells deposited on a VACNF array.¹¹⁰⁻¹¹¹ An ultra-high capacity of ~3,000 to 3,500 mAh/g (relative to Si mass) was obtained at low to normal power rates, from C/10 to C/0.5 (or 2C), matching the theoretical properties of amorphous Si.¹¹⁰ More importantly, this value was maintained around ~3,000 mAh/g at high rates up to ~8C.¹¹¹ This unique anode is used in this work to match a TiO₂ cathode for assessing the power performance at high charge-discharge rates comparable to those used in supercapacitors.

Reversible lithiation of bulk anatase TiO₂ to the final form of Li_xTiO₂ (with x = 0.5) at ~1.7 V (vs. Li/Li⁺) gives a theoretical specific capacity of 168 mAh/g.¹¹²⁻¹¹³ Interestingly, this potential lies in the middle of typical anode and cathode materials. Hence, it could be used either as an anode or a cathode for unconventional LIBs. Here we use TiO₂ as the cathode material to match the Si-coated VACNF anode in order to test the high-rate performance of the full cell. Another consideration is that anatase TiO₂ can be easily deposited as nanostructured shells on VACNFs in a similar fashion to the Si-coated VACNF anode using a reactive ion sputtering process.

The rate capability of bulk TiO₂ is generally poor due to its low electrical conductivity and slow ion diffusion capability.^{112, 114} Nanostructured TiO₂ with the crystal size of a few tens of nanometers has been demonstrated to overcome these problems.¹¹⁴⁻¹¹⁵ In addition, the large electrode/electrolyte interface generates additional pseudo-capacitance due to the fast surface reactions, which lifts the overall capacity higher than the theoretical bulk value.¹¹³⁻¹¹⁵ For example, Shin *et al.* demonstrated that a hierarchical nanoporous anatase TiO₂ was able to provide 229 mAh/g of fully reversible discharge capacity at 5C to retain a capacity of ~50 mAh/g even at an extremely high rate of 60C (namely completing charge/discharge in only 1 min), approaching the characteristics of pseudo-capacitors.¹¹⁴ In this study, we demonstrate that

a similar high-rate performance can be obtained with nanostructured TiO₂ shells deposited on the VACNF arrays in a full cell with a Si-coated VACNF anode. The full cell shows unique battery-pseudocapacitor hybrid features and can operate in a wide range of C-rates, revealing new insights into developing high-performance electrochemical energy storage systems that combine the merits of both LIBs and supercapacitors.

3.3.1 Experimental Details

VACNFs for this work were grown on copper foils by plasma enhanced chemical vapor deposition for 30 minutes to achieve an average length of 5.0 μm using a Black Magic system (Aixtron, Sunnyvale, CA, USA). High vacuum magnetron sputtering was employed to deposit Si or TiO₂ onto VACNFs to form coaxial shells by a commercial vendor (UHV Sputtering Inc., Morgan Hill, CA, USA). The Si deposition was performed under a processing pressure of ~ 8 mTorr (adjusted with a flux of ultrapure argon) at a deposition rate of 30 nm/min until a nominal thickness (i.e., equivalent to the film thickness on a flat surface) of 500 nm was deposited. The thickness of the film was monitored throughout the deposition with a quartz crystal microbalance. Titanium dioxide was deposited at a rate of 3.1 nm per min to a nominal thickness of 500 nm by reactive ion sputtering of a Ti target at the similar processing pressure using ultrapure argon mixed with 50% oxygen. The substrate temperature was not controlled during sputtering but was below 150 °C. SEM further validated the nominal thicknesses of the Si and TiO₂ films at the cross-section of the cleaved reference Si wafer. All deposited samples were stored under argon until use.

The morphology of the coated VACNF arrays were characterized with a SEM (FEI Nano430) at 5 kV accelerating voltage and a TEM (FEI Tecnai F20 XT) at 200 kV accelerating

voltage. The crystal structure of the coatings was examined with a Raman microscope (Model DXR, Thermo Scientific, Wisconsin, USA) with a 10X 0.25NA objective and a 532 nm laser at 5-mW power.

The full cell consisted of a lithiated Si-VACNF anode and a pristine TiO₂-VACNF cathode. Before assembly, the pristine Si-VACNF electrode was first conditioned by 4 cycles each at 90 μ A and 180 μ A between 1.50 V and 0.050 V versus a Li counter electrode in an El-Cell. The cell was stopped at 0.05 V in an additional lithiation step at 90 μ A and held constant for 300 seconds before being disassembled and then reassembled with a 16-mm diameter TiO₂-VACNF cathode into another 2032 coin cell. A separator soaked with the electrolyte was placed between the two electrodes to provide the desired amount of electrolyte that can fill the whole coin cell after compressing. The as assembled cell was in the charged state with an open circuit voltage (OCV) of \sim 1.7 V.

Galvanostatic charge-discharge cycling was performed using an 8-channel battery analyzer BST8-MA (MTI Corporation, Richmond, CA). Selected currents were used ranging from 45 μ A to 4.5 mA. The mass-specific capacity was calculated by dividing the mass of the active materials on the electrodes estimated from the measured nominal thicknesses (Si: 456 nm; TiO₂: 500 nm), known densities (Si: 2.33 g/cm³; TiO₂: 3.50 g/cm³), and the geometric electrode areas. The combined mass of Si and TiO₂ on both of the electrodes was used in some calculations to assess the overall energy storage properties.

3.3.2 Results and Discussion

The core-shell architectures with both Si and TiO₂ coatings on the VACNFs behave as battery-pseudocapacitor hybrids. The Si-VACNF electrodes contribute more of a battery-like lithium

insertion/extraction while TiO_2 -VACNF electrodes are dominated by pseudocapacitive surface reactions. The full cell performance combined a Si-VACNF anode and a TiO_2 -VACNF cathode, which operates from 1.0 to 2.5 V.

The full-cell performance depends not only on the properties of each electrode materials, but also on the capacity ratio between them.¹¹⁶ Due to the large difference in the specific capacities of Si and TiO_2 , the available Li^+ storage capacity of the Si electrode is about 16 times that of the TiO_2 electrode (0.965 mAh vs. 0.059 mAh), though the mass of the active materials is about the same. As a result, the TiO_2 cathode limits the capacity of the full cell. As illustrated in Figure 3.23⁹¹, the charge and discharge processes only caused a small potential change (< 0.20 V) in the Si-VACNF anode while the potential of the TiO_2 -VACNF cathode varied in the full range of ~ 1.5 V. The full cell charge-discharge profile at 90 μA current not only matches the full half-cell capacity of TiO_2 (0.058 mAh), but also reflects the exact shape of a TiO_2 half-cell profile. The cell voltage varies between 0.60 V and 2.15 V, about 0.1 to 0.3 V lower than the difference between two half-cell profiles, likely due to the internal polarization drop. The expected potential change at the Si anode is even smaller (< 0.1 V) while the polarization drop increases from ~ 0.8 to 0.3 V.

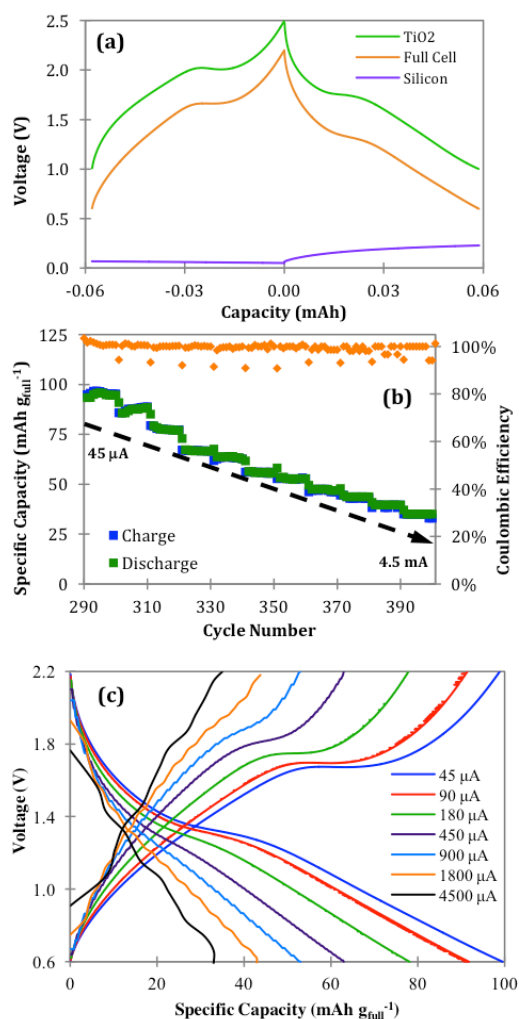


Figure 3.24 (a) The voltage profile of the Si-TiO₂ full-cell at 90 μ A in comparison with the half-cells of TiO₂-VACNF and Si-VACNF electrodes. (b) The performance of the Si-TiO₂ full-cell during charge-discharge cycling between 2.2 V and 0.6 V as the current was stepwise increased from 45 μ A to 4,500 μ A, showing charge (blue squares) and discharge (green squares) capacities (left vertical axis) and coulombic efficiency (orange diamonds) (right vertical axis). (c) The corresponding charge-discharge voltage profiles of the Si-TiO₂ full-cell at various currents.

In calculating the specific capacity of the full cell, the combined mass of Si and TiO₂, (606 μ g) was used, thus giving a value lower than the TiO₂ half-cell. Increasing the TiO₂ mass loading would increase the value, which can be achieved by using longer VACNFs and thicker TiO₂ layers at the cathode. However, this was not adopted due to the cell assembly method that may

damage the CNFs. It needs to be noted that it requires loading sufficient Li in at least one of the electrodes before cell assembly. In most commercial LIBs, lithiated cathodes with larger Li capacity than the anode serve as the Li source and the cells are assembled in the discharged state.¹¹⁷ In this study, a fully lithiated Si anode was assembled with a pristine TiO₂ cathode to form a full cell in a charged state. The overwhelming Li capacity pre-stored in the Si anode ensured that plenty of Li⁺ ions were available to flood into the TiO₂ cathode and to compensate for other side reactions during the first discharging process. Since only a small portion of the Li in the lithiated Si was involved in later charge-discharge processes, the Si anode in such full cells is much more stable than full charge/discharge cycles during the half-cell tests.

Figure 3.23b shows the full cell cycling between 2.2 to 0.6 V, with the current ranging from 45 μ A to 4.5 mA. At the lowest current of 45 μ A, the cell achieved its highest capacity of 0.0575 mAh (94.9 mAh/g_{full}), which was 97.4% of the theoretical capacity 0.059 mAh (97.4 mAh/g_{full}) of the TiO₂ cathode. At the highest current of 4.5 mA, a respectable capacity of 0.020 mAh (33.0 mAh/g_{full}) was measured, retaining ~34% of the full capacity. It took only 16 seconds to complete the full charge or discharge at 4.5 mA, essentially operating as a supercapacitor. The charge-discharge curves of the Si-TiO₂ full-cell at different current rates are shown in Figure 3.23c. The full-cell profiles closely resemble the profiles of a TiO₂ half-cell at all current rates. At higher currents, the full-cell voltage profiles become nearly linear, clearly dominated by the fast pseudocapacitive contribution.

Electrochemical impedance spectroscopy (EIS) results (Figure 3.24)⁹¹ of the Si-TiO₂ full cell after 400 charge-discharge cycles further confirmed that the TiO₂-VACNF cathode dominated the properties of the full cell. The Nyquist plots of EIS measured at the cell voltages from 0.6 V (fully discharged state) to 2.2 V (fully charged state) are dominated by a quasi-straight line slightly tilt off from the vertical axis (see inset of Figure 3.24), representing the pseudocapacitor feature. A small semicircle was only visible after zooming into the high frequency region close to the origin, indicating the small contribution of bulk faradaic reaction associated with Li insertion/extraction. At higher cell voltages, the Nyquist curve shifts toward a vertical line, closer to the feature of an ideal pseudocapacitor.

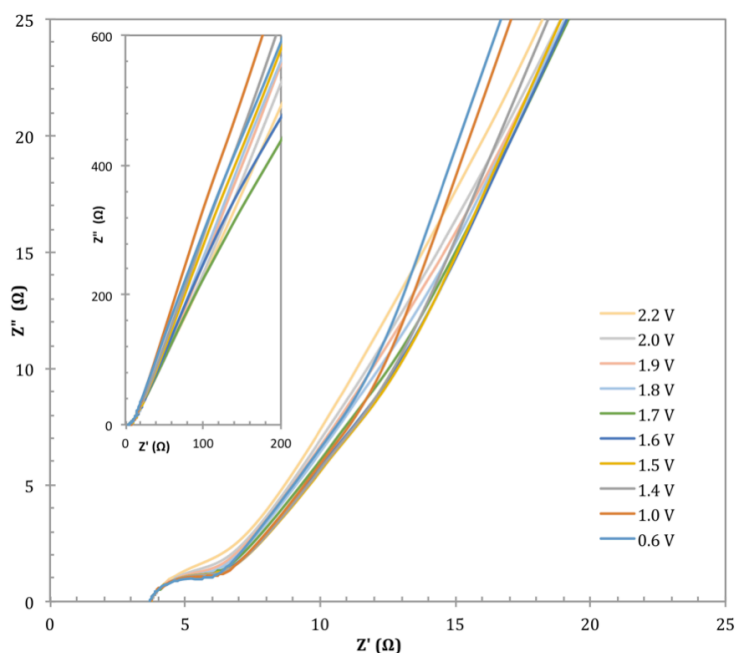


Figure 3.25 Nyquist plot of the electrochemical impedance spectra (EIS) of the Si-TiO₂ full-cell after going through 400 charge-charge cycles. Each spectrum was measured at a static voltage varied from 0.6 V to 2.2 V using a CHI 760D potentiostat (CH Instruments, Austin, TX) with a 5 mV AC voltage over a frequency range from 100 kHz to 0.01 Hz. The inset is an expanded view of the spectra.

As shown in Figure 3.23, the galvanostatic charge-discharge curves of the Si-TiO₂ full cell supported on VACNFs represent the hybrid feature of a battery (with a simple flat plateau) and an asymmetric pseudocapacitor (with a linear line). The method for calculating the specific energy and specific power is thus different from those in literature for batteries or supercapacitors.^{93, 118} Calculation methods need to be derived from the fundamental principles. Here the delivered specific energy (E , in the common unit Wh/kg) is calculated from the V - t data in the discharge curve by the following equation:

$$E = \frac{\left(\int_{Q=0}^{Q_{max}} V \times dQ\right)}{m} = \frac{\left(\int_{t=0}^{t_{max}} V \times I \times dt\right)}{m} \quad (3.15)$$

where V is the cell voltage, Q the stored charge, t the charging time, and m is the total mass of Si and TiO₂. The average specific power (P_{avg} , in the common unit W/kg) is simply the total delivered specific energy divided by the maximum discharge time (t_{max}):

$$P_{avg} = \frac{E}{t_{max}} = \frac{\left(\frac{\int_{t=0}^{t_{max}} V \times I \times dt}{m}\right)}{t_{max}} \quad (3.16)$$

Figure 3.25a⁹¹ shows that the specific discharge capacity of the Si-TiO₂ full cell, which decreased as the current was raised from 45 μ A to 4.5 mA. This is a common phenomenon for both batteries and supercapacitors. Interestingly, the cell capacity increased after long cycling and it was able to retain 36% of the capacity as the current was increased by 100 times. Figure 3.25b⁹¹ further illustrates the full cell performance in Ragone plot.

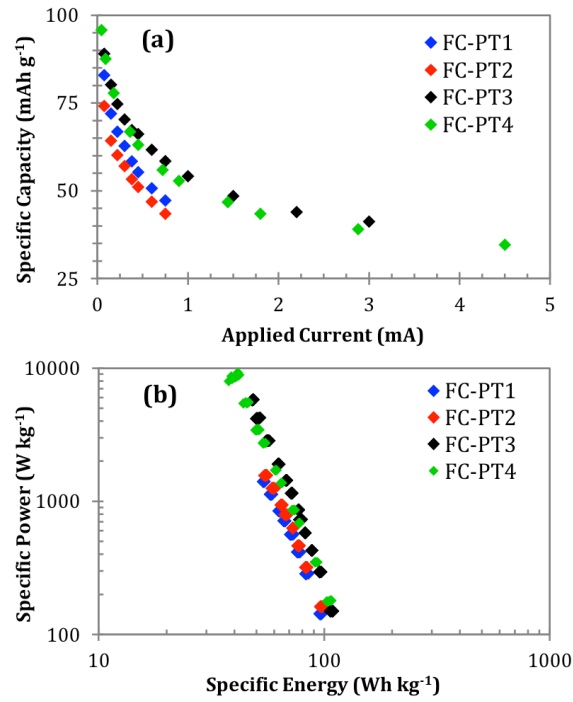


Figure 3.26 (a) The specific capacity of the Si-TiO₂ full-cell versus applied current. (b) Ragone plot of the Si-TiO₂ full cell operated at various currents. The specific energy and specific power are calculated using Eq. (1) and (2), respectively.

While the delivered specific energy (40-103 Wh/kg) matches that of a mediocre battery, the highest average power (8,830 W/kg) is nearly two orders of magnitude higher than the best batteries.¹¹⁸ The maximum delivered power (P_{max}) for a single supercapacitor electrode can be calculated by using equation 3.14. This method apparently gives much higher value in power density. For fair comparison, we adapt this method by using the total mass of Si and TiO₂ as m , and the R_s value is determined by the small voltage jump $\Delta V = 2IR_s$ when the polarity of the current was flipped during the charge-discharge transition. Figure 3.26⁹¹ shows the Ragone plot derived by this method, which reveals an even higher power performance. These values are in the range of 26,000 to 56,000 W/kg, which match the high limit for state-of-the-art supercapacitors.¹¹⁹ Furthermore, the ratio of the load resistance (R_L) to R_s in all these

measurements was high, from $\sim 12:1$ to $\sim 700:1$, and the internal energy consumption by heat dissipation is negligible in this range.⁹³ More than 92% of the stored energy is delivered to the external load even at the highest current (4.5 mA).

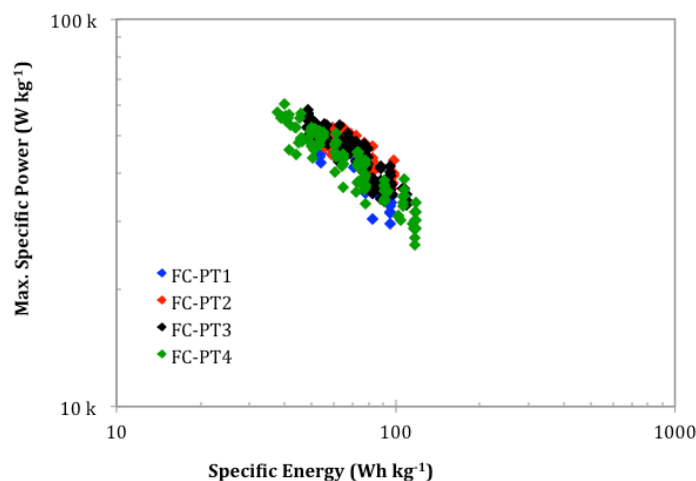


Figure 3.27 The maximum power density calculated by Eq. (4) versus the specific energy calculated by Eq. (2).

3.3.3 Summary and Conclusions

In conclusion, a unique lithium ion battery based on a Si anode and a TiO_2 cathode was demonstrated. Both electrodes were in the form of nanocolumnar shells coated on vertically aligned carbon nanofiber arrays, which served as the 3D structural support and as an effective current collector. The charge/discharge profile of the full cell resembles the hybrid feature of a battery (with a flat plateau) and a supercapacitor (with a tilt linear line), indicating the significant pseudocapacitive contribution by fast faradaic reactions at the outer surface or a thin layer near the surface of Si and TiO_2 in the nanocolumnar shells. The electrodes behave closer to a battery at low current rates but become more like a pseudo-capacitor at high current rates. The properties of the full cell can be also tuned from a battery to a pseudo-capacitor by changing the capacity ratio between the two electrodes. The Si- TiO_2 full cell showed a high specific energy (103

Wh/kg at the low current density of $\sim 74 \text{ mA/g}_{\text{full}}$), comparable to a LIB battery, and a remarkable specific power ($56,000 \text{ Wh/kg}$ at the high current density of $\sim 7.4 \text{ A/g}_{\text{full}}$) reaching the limit of the state-of-the-art supercapacitors. The Si-coated VACNF anode showed optimal properties in terms of energy, power, and stability. Using a cathode material matching the properties of the Si anode will lead to further optimization of the full-cell performance. These results provide insights into developing future high performance LIBs.

4 Plasmonic Three-Dimensional Transparent Conductor

Transparent conductors (TCs) are essential components of optoelectronic devices that need a conducting surface that is also optically transparent. Presently, indium tin oxide (ITO) is the most commonly used TC and has been studied extensively.¹²⁰ The popularity of ITO is due to its high conductivity in combination with its excellent transparency. However, the presence of the rare element indium makes ITO costly. In addition, ITO displays parasitic absorption from 350 to 500 nm, making it less desirable for photovoltaic applications.¹²¹ Therefore, an extensive amount of research has been conducted to find a better and cheaper alternative than ITO.^{24, 122}

Traditional 2D TCs are important in many applications, but an additional area of interest is to fabricate the TCs with a 3D surface nanostructure. This provides a highly desired increase in overall surface area that may be desirable for various optical, electronic, optoelectronic, and electrochemical applications.¹²³⁻¹²⁶ The transparent 3D nanostructured glass template developed by Aytug *et al.* provides a model platform on which a 3D TC can be fabricated.²⁰ The highly porous, non-conducting glass thin film network has a significantly increased surface area (i.e., a factor of 10-100) as compared to a planar surface while effectively maintaining the optical transparency of the glass substrate. Therefore, if the highly porous nanostructured glass can be conformally coated with a transparent conducting material, a possible replacement for 3D TCs made from transparent conducting oxides (TCOs) can be achieved. Unfortunately, due to its highly porous nature, a line-of-sight method provided by well-known physical vapor deposition (PVD) approaches would produce unwanted shadowing effects and chemical vapor deposition (CVD) would not provide a uniform coating. Hence, the best method to conformally coat 3D surfaces with a high aspect ratio is to use ALD, which employs gas-phase precursors that are able to penetrate porous cavities.³⁰ A TCO layer deposited by ALD is expected to generate a

continuous conducting film throughout the entire porous nanostructured glass surface due to the self-terminating, atomic layer growth process. AZO is an excellent choice as a TCO since its conductivity can be controlled by the Zn:Al ratio during the ALD process. In addition, the transmittance of AZO extends throughout the entire visible spectrum with a band gap in the range of 3.23 eV to 3.73 eV depending upon the charge doping concentration, making it ideal for photovoltaic applications.⁴³

Furthermore, the addition of plasmonic metal nanoparticles has been demonstrated as a beneficial approach to improve light management in photovoltaic devices.¹²⁷⁻¹³¹ Therefore, plasmonic nanoparticles can be combined with 3D TCO systems to further enhance their light trapping capabilities for improved performance. As light is incident on metal nanoparticles, collective oscillations of electrons on the metal surface are produced. These collective oscillations of electrons, or plasmon, become localized on the metal nanoparticles due to their restricted dimensions. When the frequency of the incident light is resonant with the collective oscillation of the electrons on the surface of the metal nanoparticles, both strong absorption and strong scattering may occur. This resonant frequency is known as localized surface plasmon resonance (LSPR). The complex dielectric constant, dimensions, and shape of the metal nanoparticles, as well as the refractive index of the surrounding material, determine the LSPR frequency. LSPR enhanced light trapping has been demonstrated in a recent study of gold plasmonic nanoparticles self-assembled on 3D fluorine-doped tin oxide (FTO) made with nanoimprint lithography and reactive ion etching.⁷⁹ Therefore, gold nanoparticles (AuNPs) can be used in unison with ALD AZO thin films in order to enhance the performance of a 3D TC for photovoltaic and other optoelectronic applications.

In this chapter, a detailed account of the ALD coating of AZO thin films on the porous nanostructured glass substrate to produce a 3D TC is provided. This original design can be used as a possible replacement for traditional 3D TCs. In addition, the 3D conducting surface also may be utilized in applications that do not require optical transparency (e.g., integrated electrodes for supercapacitors or other energy storage devices). Furthermore, the addition of AuNPs is detailed in order to complete the fabrication of a 3D plasmonic TC.¹³² This unique design provides a possible replacement for 3D TCs that may benefit from the addition of the plasmonic AuNPs such as in photovoltaics.

4.1 Experimental Details

This section details the transformation of the insulating, porous glass surface to a conducting yet transparent surface by growth of ALD AZO. It begins with a summary of the details obtained from T. Aytug's paper on the fabrication process for the nanostructured glass. Images are included from his paper in order to elucidate the physical appearance of the nanostructured glass. Following the summary of the nanostructured glass, a detailed description of the experimental process for the coating of AZO by ALD is covered. Additionally, the method and equipment used for fabricating the AuNPs on the AZO coated surface is mentioned. The section then concludes with a description of the characterization equipment and methods that were utilized.

4.1.1 Fabrication of Nanostructured Glass

The nanostructured glass used for this experiment was provided by Dr. Tolga Aytug from Oak Ridge National Laboratory. It was originally developed as an artificial superhydrophobic surface, but the unique porous nature of the glass provides the possibility for additional applications. The

scanning electron microscope image in Figure 4.1a²⁰ reveals the coral-like nature of the porous nanostructured glass as seen from above. The cross-sectional image shown in Figure 4.1b²⁰ shows that the vacant regions, produced through the etching process, continue down the whole depth of the nanostructured film with a total thickness of approximately 200 nm as determined from the scale bar. Altering the fabrication conditions can control the thickness and porosity of the nanostructured glass.

Radio-frequency magnetron sputtering was used to deposit thin film glass coatings (thickness = 0.5–1 μm) onto fused silica substrates at room temperature using a 2-inch diameter target made from a borosilicate glass composition comprising 66 mol% SiO_2 , 26 mol% B_2O_3 , and 8 mol% Na_2O . This composition ensures metastable phase separation after post-deposition thermal processing and enables removal of one of the phases through differential etching to create the desired 3D nanoporous surface structure.

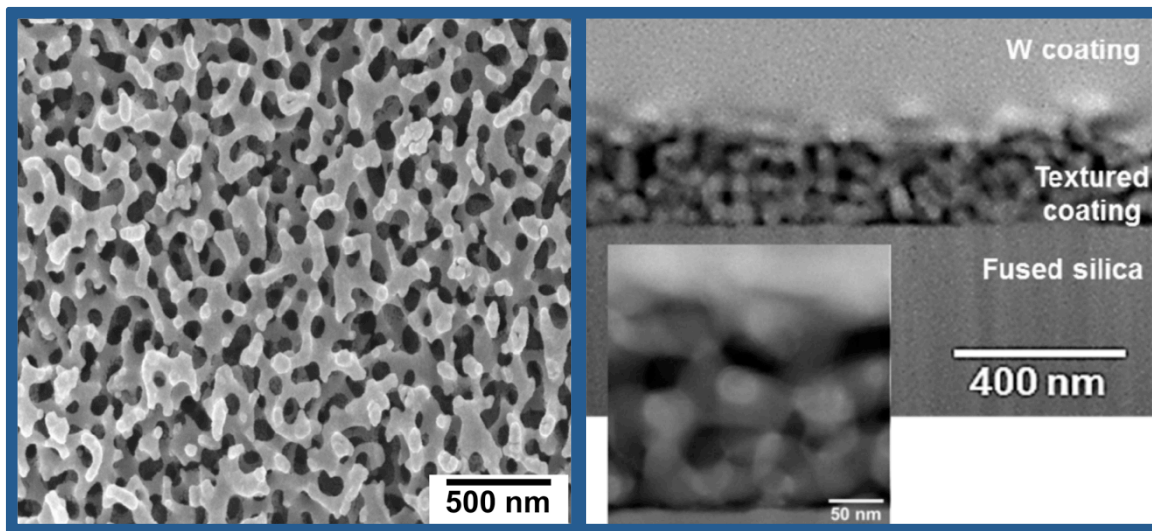


Figure 4.1 (a) Top down view of the spinodally phase-separated nanostructured glass which reveals a coral-like nature. (b) Side view of the nanostructured glass coating showing a thickness of approximately 200 nm.

4.1.2 ALD AZO Growth

Before the growth of the AZO films, conducting electrodes 21.6 mm apart were applied to the ends of the nanostructured glass for I-V measurements. The electrodes were deposited using electron-beam evaporation and consisted of 8 nm Ti and 50 nm Au. AZO films were then grown in a custom-built ALD system using high-purity H₂O (optima grade, Fisher Scientific), diethylzinc (DEZ, (C₂H₅)₂Zn; research grade, SAFC Hitech), and trimethylaluminum (TMA, Al(CH₃)₃; semiconductor grade, Akzo Nobel) as precursors. Ultrahigh purity (UHP, 99.9999%) N₂ was used as the carrier and purging gas with a constant flow rate of 5 sccm throughout all cycles during ALD operation. Every 20 cycles composed one supercycle where each supercycle contained 19 cycles of alternating H₂O and DEZ for every one doping cycle of H₂O and TMA. The 19:1 Zn/Al doping ratio achieves an AZO resistivity of around $4.2 \times 10^{-3} \Omega \cdot \text{cm}$ on planar glass. The porous nanostructured glass substrates were heated to 200 °C during AZO growth, and ALD cycling began with an H₂O exposure to prepare the nanostructured glass surface with hydroxyl groups for reaction with the first TMA pulse. After each precursor exposure, the ALD chamber and gas feeding lines were purged with UHP N₂ to prevent chemical vapor deposition from occurring. The AZO growth rate is ~0.17 nm/cycle, which is consistent to, and slightly less than, other published results of ~0.19 nm/cycle with a similar doping ratio. Initial AZO growth on the porous nanostructured glass consisted of 5 supercycles (100 total cycles) for an approximate thickness of 17 nm. Subsequent cycles were added in order to achieve AZO thicknesses of 27, 37, and 47 nm.

4.1.3 Deposition of Gold Nanoparticles

After ALD growth of the AZO conducting film, an 8 nm nominal Au film was deposited by electron-beam evaporation, where the thickness of the coating was monitored *in situ* by a quartz crystal microbalance. The AZO/nanostructured glass substrates were held at 300 °C throughout the Au deposition in order to facilitate the formation of plasmonic AuNPs. According to R. Lu *et al.*, the mean dimension of 8 nm AuNPs grown at the same temperature on SiO₂ was 32.4 ± 14.9 nm and on graphene was 31.2 ± 12.9 nm.⁸⁰ Therefore, the dimensions of the AuNPs for this experiment are expected to be approximately the same size. AuNPs with these dimensions were chosen because they provide less Ohmic loss while maximizing light trapping due to scattering.¹²⁷

4.1.4 Characterization Equipment

Surface morphology characterization for the uncoated and coated porous nanostructured glass substrates was accomplished by employing field emission scanning electron microscopy (FESEM, LEO 1550) and atomic force microscopy (AFM, WITec alpha300). Optical transmittance measurements were acquired utilizing a Horiba automated imaging spectrometer (iHR550) with an attached Labsphere integrating sphere (RTC-060-SF). The planar, non-conducting side of the glass was used as the light incident side during the transmittance measurements to represent the typical configuration of a functional solar cell. Electrical characterization was performed on a custom-built, 4-probe system utilizing an Agilent B1505A Power Device Analyzer/Curve Tracer.

4.2 Results and Discussion

4.2.1 Schematic and Scanning Electron Microscope Images

Figure 4.2a¹³² is a cross-sectional drawing representing the morphology of the porous nanostructured glass (blue in color) that was used in this study. Since ALD coating is highly conformal, a continuous AZO film (marked as green) with uniform thickness on top of the nanostructured glass is expected in the selected thickness range as is shown in Figure 4.2b¹³². Note that with the increased AZO thickness, some of the small pores having radii comparable to the ALD AZO coating thickness may have completely closed up (i.e., the case where the AZO film completely fills the openings of some cavities). This results in more of a surface porous nature than a true 3D porous structure, but varying the glass etching conditions, as well as utilizing a thinner AZO layer can help prevent that from occurring. Considering the similarities between morphology and surface chemistry, the schematic also shows formation of AuNPs (denoted in gold) on the AZO surface in a fashion similar to those that formed on a trapezoidal FTO surface pattern as reported by Wang *et al.*⁷⁹ The trapezoidal FTO surface contained 50 nm diameter AuNPs after deposition of a 15 nm nominal thickness Au film. A finite-difference time-

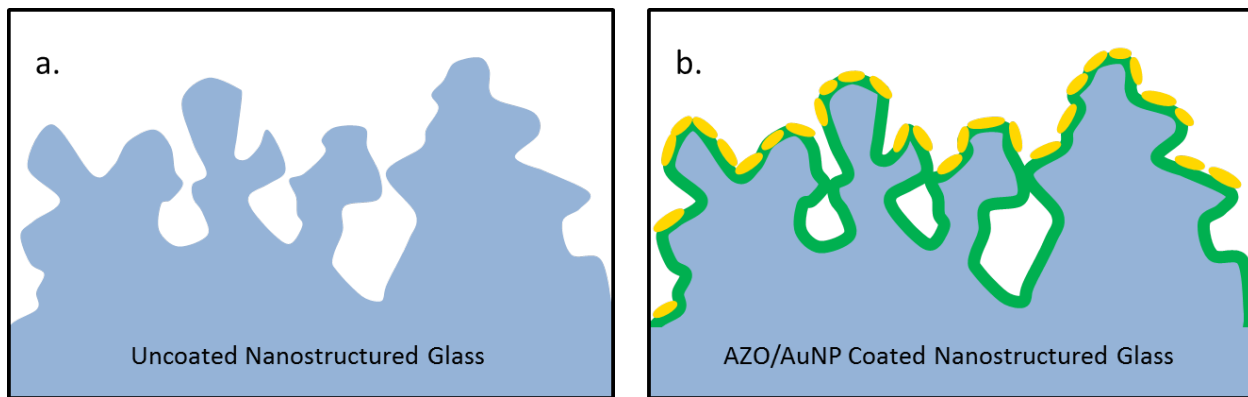


Figure 4.2 Cross-sectional schematics representing the (a) porous uncoated nanostructured glass (in blue) and (b) coated nanostructured glass with AZO (in green) and AuNPs (in gold).

domain simulation of the AuNP/nanopatterned FTO structure revealed that the combination of the photonic structured TCO with plasmonic AuNPs led to a considerable enhancement in light trapping as compared to the case of either a photonic or plasmonic nanostructure. Compared to the AuNP/nanopatterned FTO, the AuNP/AZO/porous nanostructured glass reported here has an economical advantage owing to a simplified processing scheme and its scalability for commercialization.

The FESEM images taken of the porous nanostructured glass before and after coating with AZO and AuNPs are compared in Figure 4.3¹³². Figure 4.3a reveals the coral-like nature of a representative uncoated porous nanostructured glass with approximate pore sizes of 40-80 nm. A substantial difference in surface morphology is apparent after coating with 47 nm AZO, as shown in Figures 4.3b and 4.3c. The rough surface of the nanostructured glass is clearly evident, but it does not appear to be as porous as the uncoated sample. This is to be expected since all of

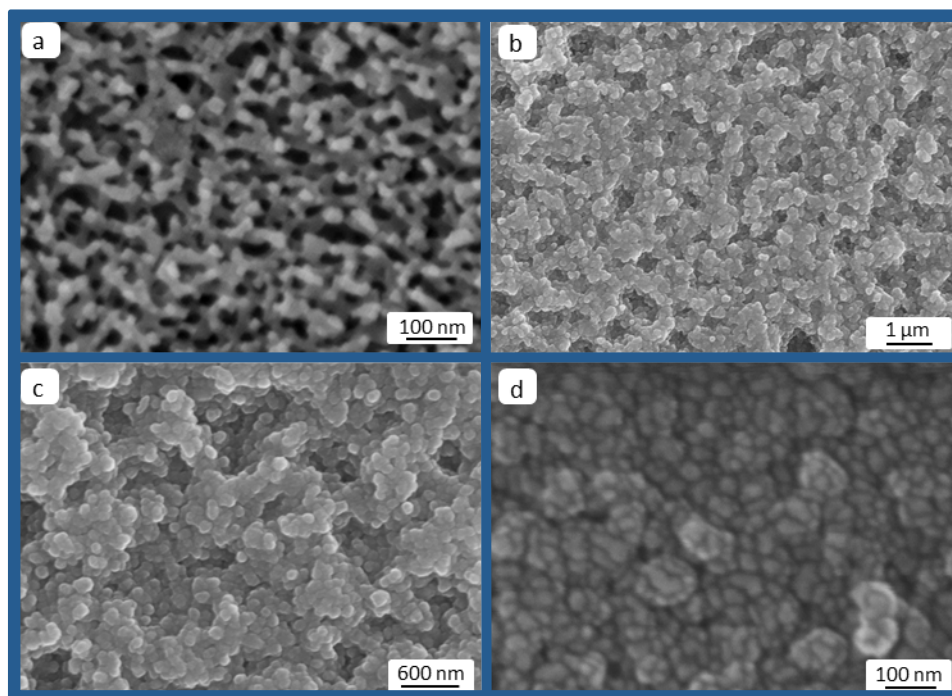


Figure 4.3 FESEM images of nanostructured glass. (a) Uncoated quartz, (b) & (c) quartz with 47 nm AZO at different magnifications, and (d) borosilicate with 27 nm AZO and 8 nm AuNPs.

the pores with openings less than twice the deposition thickness will ultimately be closed. Therefore, if the maximum surface area is desired for applications, then it is important to keep the AZO thickness as thin as possible while still maintaining the best possible conductivity. However, note that the dimensions of the porosity, as well as the size of the silica skeleton, can easily be manipulated through adjustment of the processing parameters for desired TCO coverage and electrical properties. The ALD coated AZO has a much smoother surface morphology compared to TCO films constructed from other physical or chemical vapor deposition approaches. For example, commercial FTO films have a distinctive granular surface morphology with feature dimensions typically on the order of a few hundred nanometers.⁷⁹ In contrast, the AZO films shown in Figures 4.3b and 4.3c appear to coat the porous glass smoothly and conformally. This is expected because of the layer-by-layer coating mechanism inherent to the ALD process and the employment of a low growth temperature further prevents mobility of the surface species to form distinctive features. Figure 4.3d reveals the size and distribution of the AuNPs on the surface of nanostructured borosilicate glass coated with 27 nm AZO. For 8 nm Au electron beam deposition at 300 °C, the observed lateral dimensions of the AuNPs between 20-50 nm are reasonable according to previously published results.⁷⁹⁻⁸⁰

To investigate the surface morphology further, AFM was used to compare the porous nanostructured glass before coating with AZO (Figure 4.4a)¹³² to the surface porous nature that appears after coating with AZO and AuNPs (Figure 4.4b)¹³². It can be seen that the roughness of the porous nanostructured glass surface sharply increased after coating a layer of AZO with AuNPs where the peak-to-valley distance is on the order of 250 nm within the spatial range of only 30 nm. The AuNPs do not show up clearly on the line scan of Figure 4.4b because their nominal thickness and spacing is very small compared to the peak-to-valley distances shown.

The observed smaller roughness obtained on the uncoated sample is most probably caused by the inaccessibility of the AFM tip into the small pores of the nanostructured film matrix. In the line scan of Figure 4.4a, pores are shown as shallow dents of depth on the order of tens of nanometers and appear to occur more frequently than the vertical changes in direction for the line scan of Figure 4.4b. The overall vertical roughness was brought up after AZO/AuNP coating, since the edges around the pores have added height. The increased nonuniformity of the surface roughness may also be attributed to the pore size variation. While larger pores remain, smaller ones might have been completely filled with AZO. It is interesting to note that, comparing the line-scan in Figure 4.4b with the photonic structures made on FTO using nanoimprint lithography, a comparable lateral pitch size of $\sim 300\text{-}500$ nm is observable for the AZO-coated porous nanostructured glass as well. In particular, the conversion from the porous to protruding nanostructured surface after ALD AZO coating is beneficial for further fabrication of functional structures atop, such as solar cells, using PVD or CVD methods.

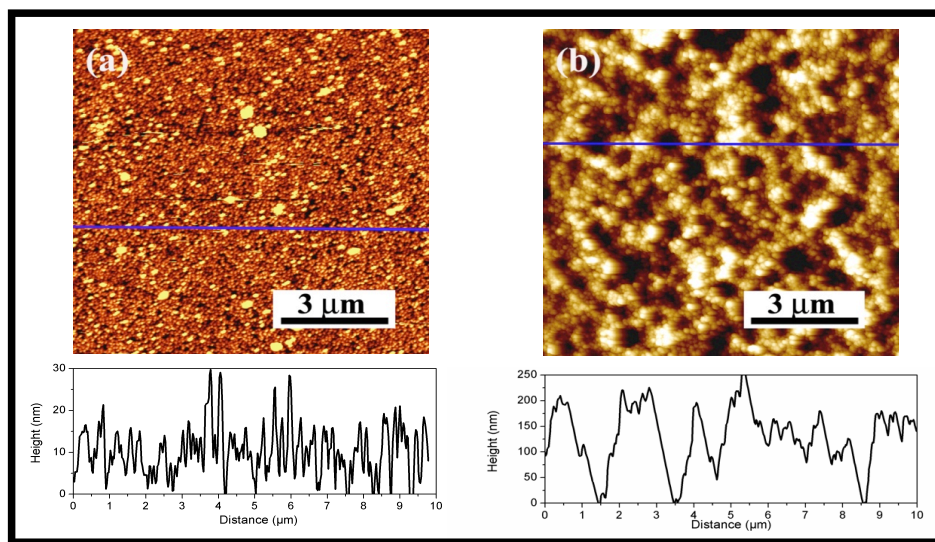


Figure 4.4 AFM images of the (a) uncoated nanostructured glass and (b) nanostructured glass coated with 47 nm AZO and 8 nm AuNPs. The height profiles were taken along the blue line shown on the AFM images. These profiles reveal the rough nature of the substrate surfaces.

4.2.2 Transmittance Measurements

A photograph showing the transparency through an uncoated nanostructured glass sample (on the left) as well as a coated counterpart having 27 nm AZO (on the right) is shown in Figure 4.5a¹³².

The University of Kansas Jayhawk logo is clearly visible through both samples with the coated

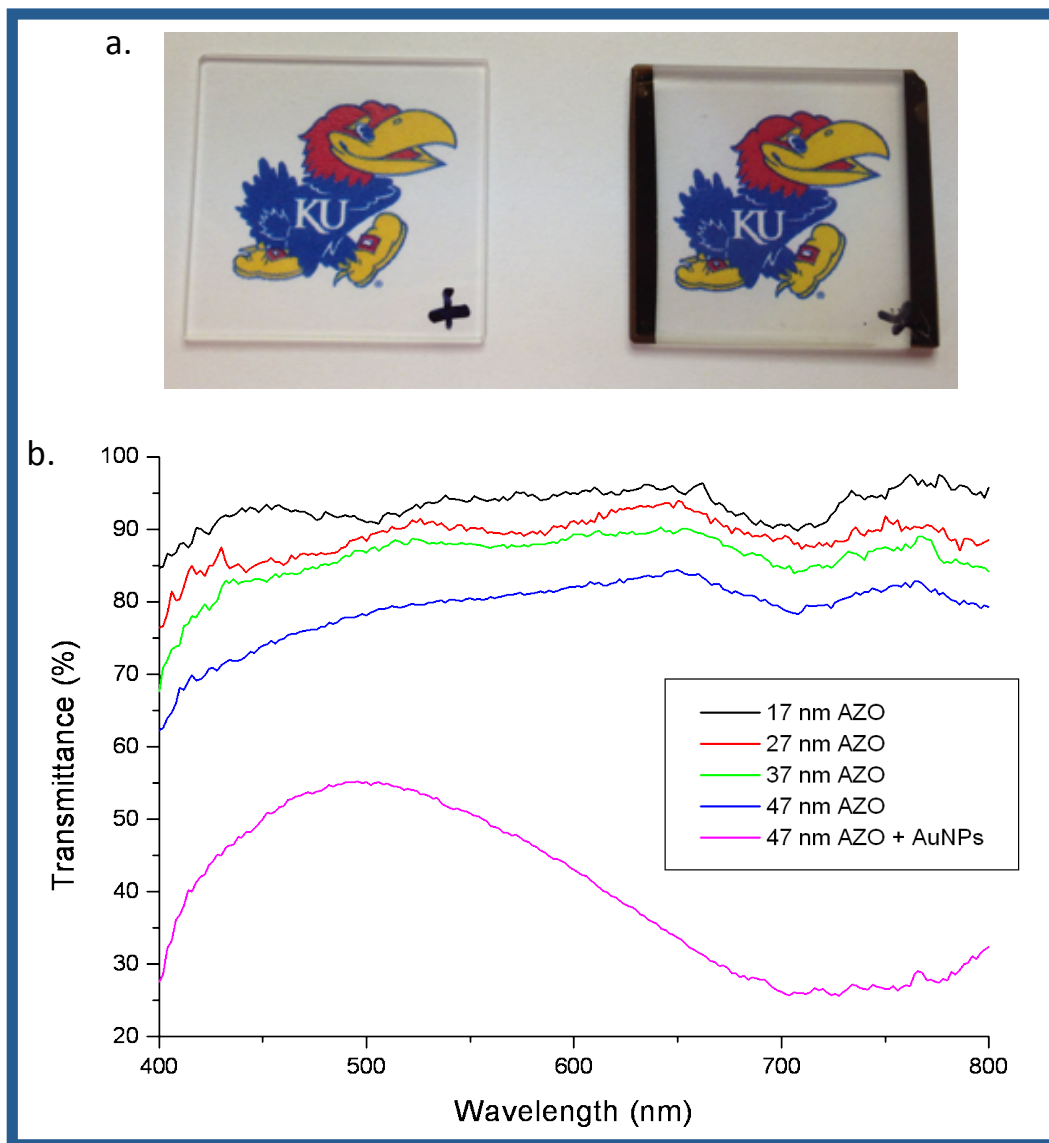


Figure 4.5 (a) Photograph showing transparency of uncoated nanostructured glass on the left and nanostructured glass with 27 nm AZO coating on the right. (b) Transmittance vs. wavelength spectra for the 17, 27, 37, and 47 nm thick AZO coatings. Data for the 47 nm AZO sample with 8 nm AuNPs is also shown, clearly revealing the LSPR wavelength of 728 nm and the corresponding minimum transmittance of 25.7%.

sample having 89.2% transmittance of the uncoated sample at 550 nm. The sample on the right also shows the Ti/Au contacts that were applied to decrease the contact resistance for electrical measurements. The wavelength dependent optical transmittance over a spectral range from 400 to 800 nm for 17, 27, 37, and 47 nm thicknesses of AZO films, as well as for the 47 nm AZO coupled with 8 nm AuNP sample, are shown in Figure 4.5b¹³². As expected, the transmittance decreases with increasing AZO thickness but still stays above 80.5% at 550 nm for the thickest film, which is comparable to that of TCOs employed in solar cells. Once the AuNPs were added to the 47 nm AZO film, the overall transmittance greatly decreased due to plasmonic light trapping associated with the surface AuNPs. This verification of the plasmonic effect is associated with a conversion of the far field light to evanescent light which cannot be detected by the integrating sphere. These results were anticipated due to the work of Xu *et al.* where they demonstrated the light trapping nature of plasmonic nanoparticles in a simulation of the intensity distribution for the electric field after scattering.¹³³ The LSPR wavelength λ_p and the minimum transmittance at λ_p were determined to be 728 nm and 25.7%, respectively. Figure 4.6¹³² shows an FESEM image of the AZO/AuNP coated nanostructured glass along with a picture of the coated glass revealing the reduced transparency. In addition to the expected low transmittance, the LSPR wavelength was anticipated to be quite long compared to those determined by R. Lu *et al.* for 8 nm AuNPs on SiO₂. Their results produced an LSPR wavelength of 632 nm but, with the addition of a conducting graphene layer between the AuNPs and SiO₂, the LSPR wavelength was red-shifted toward 666 nm.⁸⁰ Therefore, it is possible that the coating of the nanostructured glass with a conducting AZO layer was responsible for producing the long LSPR wavelength of 728 nm for the 8 nm AuNPs achieved in this work.

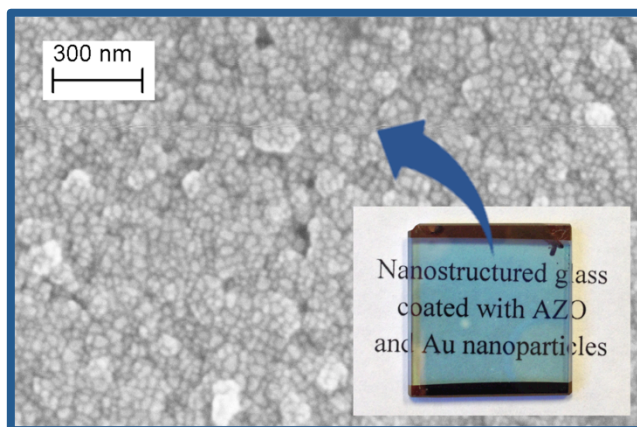


Figure 4.6 FESEM image of AuNP coated nanostructured glass. The reduced transparency provided by the AuNP coated nanostructured glass is revealed in the inset.

4.2.3 Conductivity Measurements

Resistance values of the samples were determined from the I-V curves shown in Figure 4.7¹³². A clear decreasing trend of 586, 188, 131, 126, and 116 Ω was obtained corresponding to AZO film thicknesses of 17, 27, 37, 47 nm, and 47 nm/AuNPs, respectively. The average length between the Ti/Au contacts was 21.6 mm and the average width of the nanostructured glass was 25.5 mm. These dimensions, along with the resistance values listed above, were utilized to calculate the sheet resistance values of 692, 222, 155, 149, and 137 Ω/\square , respectively. The greatest decrease in sheet resistance is attained when the thickness of the AZO film reached a critical level greater than 17 nm, above which, while there is still a steady decline in values, the relative drop rate is weakened. This can be attributed to the pores with small lateral openings being completely filled with the AZO films having thickness values around 20 nm, providing a completely percolative path for the current transport. Therefore, increased thickness beyond a critical value will not provide as much decrease in sheet resistance. For instance, pores with diameters less than 74 nm (see Figure 4.1a) are most likely completely filled when the thickness

of the AZO is grown to 37 nm. The corresponding resistivity values of the samples with only AZO appear to corroborate with this observation. In general, resistivity values should stay constant regardless of the thickness of the conducting film as long as it is not thick enough to be considered a bulk material. The calculated resistivity values are 1.2×10^{-3} , 6.0×10^{-4} , 5.7×10^{-4} , and $7.0 \times 10^{-4} \Omega \cdot \text{cm}$, corresponding to the 17, 27, 37, and 47 nm AZO films, respectively. All of these values are smaller than the $4.2 \times 10^{-3} \Omega \cdot \text{cm}$ resistivity that our system routinely produces on planar glass substrates; however, after the 27 nm AZO growth, the resistivities obtained on

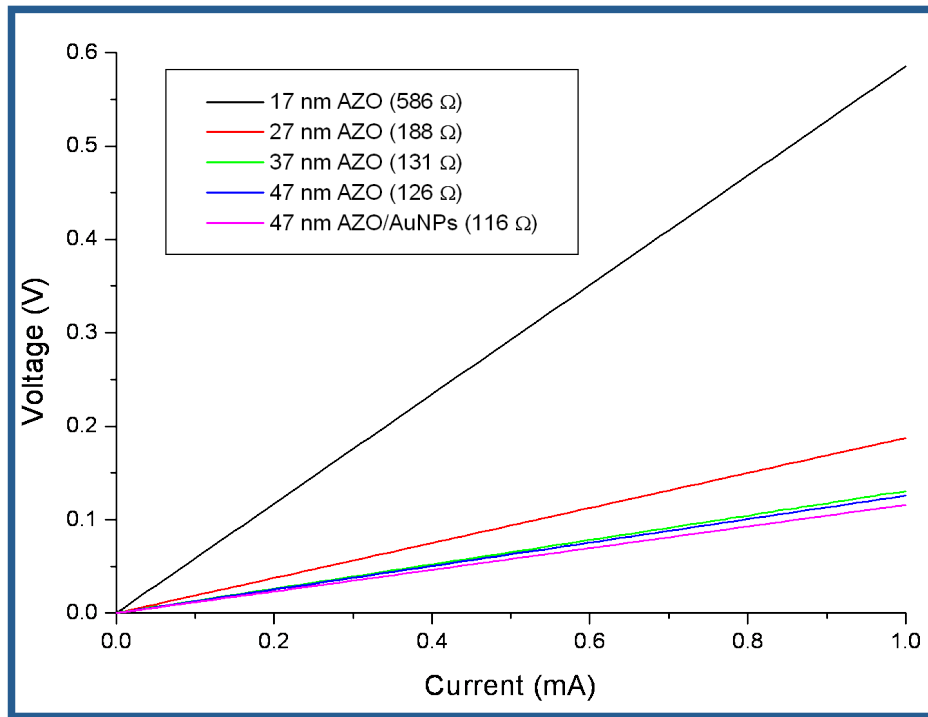


Figure 4.7 Voltage vs. current curves displaying the ohmic nature of the transparent conductors deposited on nanotextured glass substrates. Resistance values obtained for each sample are displayed in the figure.

the nanostructured glass appear to trend toward the expected value of counterpart AZO on flat glass.

Figure 4.8¹³² displays the transmittance values at 550 nm versus their corresponding sheet resistance values for the coated porous nanostructured glass samples. Transmittances of 93.3,

89.2, 88.0, 80.5, and 50.8% were obtained for the AZO thicknesses of 17, 27, 37, 47 nm, and 47 nm/AuNPs, respectively. These values reveal a clear drop in transmittance after the 37 nm thick AZO deposition with very little gain in conductivity. Nevertheless, AZO thicknesses less than 47 nm still provides optimal light transmittance at greater than 80% while the sheet resistance remains close to or below 150 Ω/\square . The optimal combination is observed for the 37 nm thick AZO film with a transmittance of 88.0% and corresponding sheet resistance of 155 Ω/\square . These observations are remarkable considering standard commercial TCOs containing ITO or FTO have thicknesses up to hundreds of nanometers, which merits the applicability of TCO coated porous nanostructured glass for various optoelectronic applications.

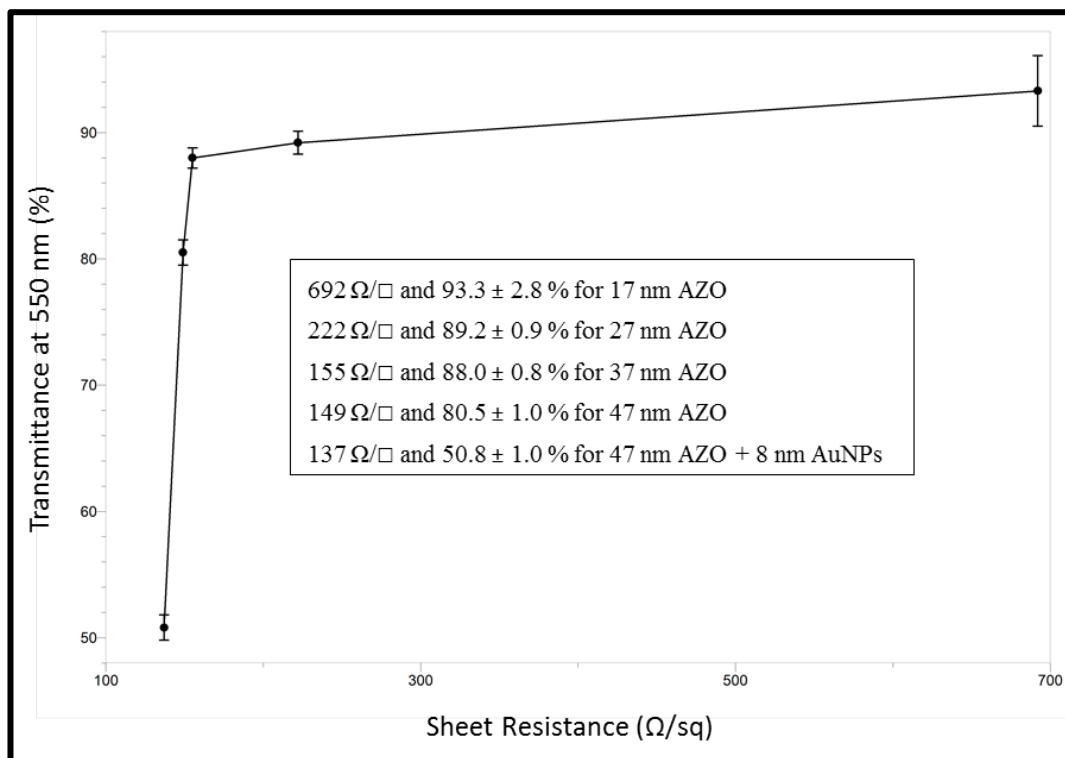


Figure 4.8 Transmittance at 550 nm versus sheet resistance for different thicknesses of AZO films and AuNPs deposited on the nanostructured glass substrates. The transmittance error bars represent one standard deviation and the sheet resistance error bars are not shown due to negligible size.

4.3 Summary and Conclusions

Transparent, nanostructured porous glass film coatings on glass platforms were utilized as a substrate for the fabrication of plasmonic 3D TCs. The non-conducting, porous nanostructured surface was converted to a conducting surface by growing conformal AZO films within the cavities of the glass-film network using ALD. AZO films ranging from 17 nm to 47 nm were achieved. After ALD AZO growth, AuNPs were incorporated onto the surface of the AZO film in order to create a plasmonic effect for the 3D TC architecture. FESEM images revealed that the highly porous nature of the conducting nanostructured glass was maintained after the AZO and AuNP growth. Line scans from AFM images displayed a large increase in surface roughness

after AZO/AuNP coating. Sheet resistance values of $\sim 150 \Omega/\square$ were obtained for the 37 and 47 nm thick AZO coated samples with good transmittance properties above $\sim 80\%$ within the visible regime. The optimal combination of transmittance (88.0% at 550 nm) and sheet resistance ($155 \Omega/\square$) was obtained for the 37 nm thick AZO film. With the incorporation of AuNPs on the AZO layer, while the sheet resistance values were maintained at high quality, the transmittance decreased significantly due to the plasmonic resonance associated with the AuNPs providing an LSPR wavelength of 728 nm and corresponding minimum transmittance of 25.7%. The encouraging results of the plasmonic 3D TC based on AZO coated nanostructured glass lead to a possible replacement for traditional TCs in optoelectronic device applications. Furthermore, the unique 3D conducting platform may be utilized for devices that do not require optical transparency, such as integrated electrodes for supercapacitors or other energy storage devices.

5 Overall Conclusions

The overall goal of this work, which was to fabricate unique 3D nanostructured substrates with the potential toward application of advanced energy storage electrodes and plasmonic transparent conductors, was accomplished. This chapter consists of a brief overview of these results and some final comments regarding this work.

Al_2O_3 conformal coating of the VACNFs was successful and ultimately led to the conformal coating with AZO to produce VACNF core-shell structures, but this accomplishment was met with the realization that coating AZO on top of Al_2O_3 will alter the doping ratio of the AZO layer. This unfortunate result of the Al_2O_3 /AZO core-shell coating led to the work with HfO_2 to be utilized as a diffusion barrier or as a complete replacement for the Al_2O_3 layer. Despite these issues, the results obtained confirmed that VACNF arrays could be coated via ALD without the need for intrusive functionalization. Furthermore, the ALD Al_2O_3 film was shown to provide an excellent dielectric layer when grown on the planar substrate. This was an important step because it provided evidence that the custom-build ALD system was functional as well as verification that the Al_2O_3 film was of superior quality.

Additional work was performed with VACNF arrays in order to fabricate a working electrochemical capacitor electrode. Sputtered Mn shells were coated on VACNF arrays and then electrochemically oxidized to form rose-petal-like mesoporous MnO_2 layers. The 3D MnO_2 /VACNF array hybrid architecture provided enhanced ion diffusion across the mesoporous MnO_2 shell and yielded excellent current collecting capability using the conductive VACNF core, both required for high-performance supercapacitors. It was shown that an excellent specific power of $\sim 240 \text{ kW/kg}$ can be obtained with such a hybrid electrode material in the specific energy range from ~ 1 to 10 Wh/kg . This design strategy clearly demonstrated the remarkable

capability of using VACNF core structures as a template for high-powered energy storage devices.

Transformation of the nanostructured glass surface from a non-conducting, porous substrate to a plasmonic transparent conductor was also successful. This too was accomplished via ALD, but this time with only AZO. As additional layers of AZO were grown on the nanostructured glass substrate, confirmed decreases in the sheet resistance were measured. Ultimately, it was shown that the AZO film thickness of ~ 37 nm provided the optimal combination of high transmittance with low sheet resistance. To complete the transformation to a plasmonic transparent conductor, successful growth of AuNPs were applied and the plasmonic effect verified.

For me personally, one of the great triumphs of this work was mastering the intricacies of ALD. This was the benefit of utilizing a custom-build system over a commercial system. Not only was I able to learn from the successful growth of Al_2O_3 and AZO, but I was also able to learn about the minor details that can result in unsuccessful growth as was the case with HfO_2 . I leave this work with confidence knowing that I have required the knowledge to build an ALD system if someone else would provide the financial means to do so.

The final chapter comes with many positive accomplishments that led to a number of quality publications that hopefully can be utilized as the foundation for someone else's future work. As is probably the case with most dissertations, the end is not truly the end, but instead, just a stopping point. Nevertheless, this work successfully accomplished the fabrication of two 3D nanostructures via atomic layer deposition for development of advanced energy storage electrodes and plasmonic transparent conductors as well as a higher-power supercapacitor electrode based on Mn oxide coating of VACNF arrays.

References

1. <http://www.worldenergyoutlook.org/publications/>.
2. <http://www.eia.gov/forecasts/ieo/>.
3. http://www.sandia.gov/~jytsao/Solar_FAQs.pdf.
4. Crabtree, G. W.; Lewis, N. S., Solar energy conversion. *Physics Today* **2007**, 60 (3), 37-42.
5. http://www.sc.doe.gov/bes/reports/files/SEU_rpt.pdf.
6. <http://iea-pvps.org/>.
7. http://www.nrel.gov/ncpv/images/efficiency_chart.jpg.
8. Green, M. A., Third generation photovoltaics advanced solar energy conversion. SpringerLink, Ed. Berlin New York : Springer: Berlin New York, **2006**.
9. Rolison, D. R.; Long, J. W.; Lytle, J. C.; Fischer, A. E.; Rhodes, C. P.; McEvoy, T. M.; Bourg, M. E.; Lubers, A. M., Multifunctional 3D nanoarchitectures for energy storage and conversion. *Chemical Society reviews* **2009**, 38 (1), 226-52.
10. Guo, Y.-G.; Hu, J.-S.; Wan, L.-J., Nanostructured Materials for Electrochemical Energy Conversion and Storage Devices. *Advanced Materials* **2008**, 20 (15), 2878-2887.
11. Arico, A. S.; Bruce, P.; Scrosati, B.; Tarascon, J. M.; van Schalkwijk, W., Nanostructured materials for advanced energy conversion and storage devices. *Nature materials* **2005**, 4 (5), 366-77.
12. Jiang, H.; Lee, P. S.; Li, C., 3D carbon based nanostructures for advanced supercapacitors. *Energy Environ. Sci.* **2013**, 6 (1), 41-53.
13. Zhang, L. L.; Zhao, X. S., Carbon-based materials as supercapacitor electrodes. *Chemical Society reviews* **2009**, 38 (9), 2520-31.
14. Pan, H.; Li, J.; Feng, Y., Carbon nanotubes for supercapacitor. *Nanoscale research letters* **2010**, 5 (3), 654-68.
15. Sherrill, S. A.; Banerjee, P.; Rubloff, G. W.; Lee, S. B., High to ultra-high power electrical energy storage. *Physical chemistry chemical physics : PCCP* **2011**, 13 (46), 20714-23.
16. Simon, P.; Gogotsi, Y., Materials for electrochemical capacitors. *Nature materials* **2008**, 7 (11), 845-54.
17. Pint, C. L.; Nicholas, N. W.; Xu, S.; Sun, Z.; Tour, J. M.; Schmidt, H. K.; Gordon, R. G.; Hauge, R. H., Three dimensional solid-state supercapacitors from aligned single-walled carbon nanotube array templates. *Carbon* **2011**, 49 (14), 4890-4897.
18. Li, J.; Stevens, R.; Delzeit, L.; Ng, H. T.; Cassell, A.; Han, J.; Meyyappan, M., Electronic properties of multiwalled carbon nanotubes in an embedded vertical array. *Applied Physics Letters* **2002**, 81 (5), 910.
19. Banerjee, P.; Perez, I.; Henn-Lecordier, L.; Lee, S. B.; Rubloff, G. W., Nanotubular metal-insulator-metal capacitor arrays for energy storage. *Nat Nanotechnol* **2009**, 4 (5), 292-6.
20. Aytug, T.; Simpson, J. T.; Lupini, A. R.; Trejo, R. M.; Jellison, G. E.; Ivanov, I. N.; Pennycook, S. J.; Hillesheim, D. A.; Winter, K. O.; Christen, D. K.; Hunter, S. R.; Haynes, J. A., Optically transparent, mechanically

durable, nanostructured superhydrophobic surfaces enabled by spinodally phase-separated glass thin films. *Nanotechnology* **2013**, *24* (31), 315602.

21. Lytle, J. C.; Wallace, J. M.; Sassin, M. B.; Barrow, A. J.; Long, J. W.; Dysart, J. L.; Renninger, C. H.; Saunders, M. P.; Brandell, N. L.; Rolison, D. R., The right kind of interior for multifunctional electrode architectures: carbon nanofoam papers with aperiodic submicrometre pore networks interconnected in 3D. *Energy & Environmental Science* **2011**, *4* (5), 1913-1925.

22. Scrosati, B.; Garche, J., Lithium batteries: Status, prospects and future. *Journal of Power Sources* **2010**, *195* (9), 2419-2430.

23. Patil, A.; Patil, V.; Wook Shin, D.; Choi, J.-W.; Paik, D.-S.; Yoon, S.-J., Issue and challenges facing rechargeable thin film lithium batteries. *Materials Research Bulletin* **2008**, *43* (8-9), 1913-1942.

24. Hecht, D. S.; Hu, L.; Irvin, G., Emerging transparent electrodes based on thin films of carbon nanotubes, graphene, and metallic nanostructures. *Adv Mater* **2011**, *23* (13), 1482-513.

25. O'Regan, B.; Grätzel, M., A low-cost, high-efficiency solar cell based on dye-sensitized colloidal TiO₂ films. *Nature* **1991**, *353* (6346), 737-740.

26. Grätzel, M., Dye-sensitized solar cells. *Journal of Photochemistry and Photobiology C: Photochemistry Reviews* **2003**, *4* (2), 145-153.

27. Peter, L. M., The Grätzel Cell: Where Next? *The Journal of Physical Chemistry Letters* **2011**, *2* (15), 1861-1867.

28. Zhang, G.; Wu, H.; Chen, C.; Wang, T.; Wu, W.; Yue, J.; Liu, C., Transparent nanotubular capacitors based on transplanted anodic aluminum oxide templates. *ACS applied materials & interfaces* **2015**, *7* (9), 5522-7.

29. Puurunen, R. L., A Short History of Atomic Layer Deposition: Tuomo Suntola's Atomic Layer Epitaxy. *Chemical Vapor Deposition* **2014**, *20* (10-11-12), 332-344.

30. George, S. M., Atomic layer deposition: an overview. *Chem Rev* **2010**, *110* (1), 111-31.

31. Miikkulainen, V.; Leskelä, M.; Ritala, M.; Puurunen, R. L., Crystallinity of inorganic films grown by atomic layer deposition: Overview and general trends. *Journal of Applied Physics* **2013**, *113* (2), 021301.

32. Tanninen, V. P.; Oikkonen, M.; Tuomi, T. O., X-ray diffraction study of thin electroluminescent ZnS films grown by atomic layer epitaxy. *Physica Status Solidi (a)* **1981**, *67* (2), 573-583.

33. Sanders, B. W., Zinc oxysulfide thin films grown by atomic layer deposition. *Chemistry of Materials* **1992**, *4* (5), 1005-1011.

34. Kaariainen, T., *Atomic layer deposition : principles, characteristics, and nanotechnology applications*. 2nd Edition.. ed.; Salem, Massachusetts : Scrivener Publishing: **2013**.

35. *Atomic layer deposition of nanostructured materials*. Weinheim : Wiley-VCH
Chichester : John Wiley distributor: Weinheim : Chichester, **2012**.

36. Hausmann, D. M.; Kim, E.; Becker, J.; Gordon, R. G., Atomic Layer Deposition of Hafnium and Zirconium Oxides Using Metal Amide Precursors. *Chemistry of Materials* **2002**, *14* (10), 4350-4358.

37. Groner, M. D.; Elam, J. W.; Fabreguette, F. H.; George, S. M., Electrical characterization of thin Al₂O₃ films grown by atomic layer deposition on silicon and various metal substrates. *Thin Solid Films* **2002**, *413* (1-2), 186-197.
38. Widjaja, Y.; Musgrave, C. B., Quantum chemical study of the mechanism of aluminum oxide atomic layer deposition. *Applied Physics Letters* **2002**, *80* (18), 3304.
39. Elam, J. W.; Routkevitch, D.; George, S. M., Properties of ZnO/Al₂O₃ alloy films grown using atomic layer deposition techniques. *J Electrochem Soc* **2003**, *150* (6), G339-G347.
40. Elam, J. W.; Sechrist, Z. A.; George, S. M., ZnO/Al₂O₃ nanolaminates fabricated by atomic layer deposition: growth and surface roughness measurements. *Thin Solid Films* **2002**, *414* (1), 43-55.
41. Elam, J. W.; George, S. M., Growth of ZnO/Al₂O₃ alloy films using atomic layer deposition techniques. *Chemistry of Materials* **2003**, *15* (4), 1020-1028.
42. Dasgupta, N. P.; Neubert, S.; Lee, W.; Trejo, O.; Lee, J.-R.; Prinz, F. B., Atomic Layer Deposition of Al-doped ZnO Films: Effect of Grain Orientation on Conductivity. *Chemistry of Materials* **2010**, *22* (16), 4769-4775.
43. Banerjee, P.; Lee, W.-J.; Bae, K.-R.; Lee, S. B.; Rubloff, G. W., Structural, electrical, and optical properties of atomic layer deposition Al-doped ZnO films. *Journal of Applied Physics* **2010**, *108* (4), 043504.
44. Ahn, C. H.; Kim, H.; Cho, H. K., Deposition of Al doped ZnO layers with various electrical types by atomic layer deposition. *Thin Solid Films* **2010**, *519* (2), 747-750.
45. Ahn, C. H.; Kong, B. H.; Kim, H.; Cho, H. K., Improved Electrical Stability in the Al Doped ZnO Thin-Film-Transistors Grown by Atomic Layer Deposition. *J Electrochem Soc* **2011**, *158* (2), H170.
46. Kong, B. H.; Choi, M. K.; Cho, H. K.; Kim, J. H.; Baek, S.; Lee, J.-H., Conformal Coating of Conductive ZnO:Al Films as Transparent Electrodes on High Aspect Ratio Si Microrods. *Electrochemical and Solid-State Letters* **2010**, *13* (2), K12.
47. Hou, Q. Q.; Meng, F. J.; Sun, J. M., Electrical and optical properties of Al-doped ZnO and ZnAl₂O₄ films prepared by atomic layer deposition. *Nanoscale research letters* **2013**, *8*.
48. Kukli, K.; Pilvi, T.; Ritala, M.; Sajavaara, T.; Lu, J.; Leskelä, M., Atomic layer deposition of hafnium dioxide thin films from hafnium tetrakis(dimethylamide) and water. *Thin Solid Films* **2005**, *491* (1-2), 328-338.
49. Perez, I.; Robertson, E.; Banerjee, P.; Henn-Lecordier, L.; Son, S. J.; Lee, S. B.; Rubloff, G. W., TEM-based metrology for HfO₂ layers and nanotubes formed in anodic aluminum oxide nanopore structures. *Small* **2008**, *4* (8), 1223-32.
50. Wang, Y.; Ho, M. T.; Goncharova, L. V.; Wielunski, L. S.; Rivillon-Amy, S.; Chabal, Y. J.; Gustafsson, T.; Moumen, N.; Boleslawski, M., Characterization of Ultra-Thin Hafnium Oxide Films Grown on Silicon by Atomic Layer Deposition Using Tetrakis(ethylmethyl-amino) Hafnium and Water Precursors. *Chemistry of Materials* **2007**, *19* (13), 3127-3138.
51. Elam, J. W.; Groner, M. D.; George, S. M., Viscous flow reactor with quartz crystal microbalance for thin film growth by atomic layer deposition. *Rev Sci Instrum* **2002**, *73* (8), 2981-2987.

52. Elliot, A. J.; Malek, G. A.; Lu, R.; Han, S.; Yu, H.; Zhao, S.; Wu, J. Z., Integrating atomic layer deposition and ultra-high vacuum physical vapor deposition for in situ fabrication of tunnel junctions. *Rev Sci Instrum* **2014**, *85* (7), 073904.
53. Malek, G. A.; Brown, E.; Klankowski, S. A.; Liu, J.; Elliot, A. J.; Lu, R.; Li, J.; Wu, J., Atomic layer deposition of Al-doped ZnO/Al₂O₃ double layers on vertically aligned carbon nanofiber arrays. *ACS applied materials & interfaces* **2014**, *6* (9), 6865-71.
54. Novoselov, K. S.; Geim, A. K.; Morozov, S. V.; Jiang, D.; Zhang, Y.; Dubonos, S. V.; Grigorieva, I. V.; Firsov, A. A., Electric field effect in atomically thin carbon films. *Science* **2004**, *306* (5696), 666-9.
55. Klein, K. L.; Melechko, A. V.; McKnight, T. E.; Retterer, S. T.; Rack, P. D.; Fowlkes, J. D.; Joy, D. C.; Simpson, M. L., Surface characterization and functionalization of carbon nanofibers. *Journal of Applied Physics* **2008**, *103* (6), 061301.
56. Ngo, Q.; Yamada, T.; Suzuki, M.; Ominami, Y.; Cassell, A. M.; Li, J.; Meyyappan, M.; Yang, C. Y., Structural and electrical characterization of carbon nanofibers for interconnect via applications. *Ieee T Nanotechnol* **2007**, *6* (6), 688-695.
57. White, C. T.; Mintmire, J. W., Fundamental properties of single-wall carbon nanotubes. *The journal of physical chemistry. B* **2005**, *109* (1), 52-65.
58. Ouyang, M.; Huang, J. L.; Lieber, C. M., Fundamental electronic properties and applications of single-walled carbon nanotubes. *Acc Chem Res* **2002**, *35* (12), 1018-25.
59. Liu, J. W.; Essner, J.; Li, J., Hybrid Supercapacitor Based on Coaxially Coated Manganese Oxide on Vertically Aligned Carbon Nanofiber Arrays. *Chemistry of Materials* **2010**, *22* (17), 5022-5030.
60. Endo, M.; Kim, Y. A.; Hayashi, T.; Fukai, Y.; Oshida, K.; Terrones, M.; Yanagisawa, T.; Higaki, S.; Dresselhaus, M. S., Structural characterization of cup-stacked-type nanofibers with an entirely hollow core. *Applied Physics Letters* **2002**, *80* (7), 1267.
61. Hirsch, A., Functionalization of single-walled carbon nanotubes. *Angew Chem Int Edit* **2002**, *41* (11), 1853-1859.
62. Banerjee, S.; Hemraj-Benny, T.; Wong, S. S., Covalent surface chemistry of single-walled carbon nanotubes. *Advanced Materials* **2005**, *17* (1), 17-29.
63. Farmer, D. B.; Gordon, R. G., Atomic layer deposition on suspended single-walled carbon nanotubes via gas-phase noncovalent functionalization. *Nano Lett* **2006**, *6* (4), 699-703.
64. Quoc, N.; Cassell, A. M.; Austin, A. J.; Jun, L.; Krishnan, S.; Meyyappan, M.; Yang, C. Y., Characteristics of aligned carbon nanofibers for interconnect via applications. *IEEE Electron Device Letters* **2006**, *27* (4), 221-224.
65. Liu, J.; Kuo, Y. T.; Klabunde, K. J.; Rochford, C.; Wu, J.; Li, J., Novel dye-sensitized solar cell architecture using TiO₂-coated vertically aligned carbon nanofiber arrays. *ACS applied materials & interfaces* **2009**, *1* (8), 1645-9.
66. Zhang, L.; Austin, D.; Merkulov, V. I.; Meleshko, A. V.; Klein, K. L.; Guillorn, M. A.; Lowndes, D. H.; Simpson, M. L., Four-probe charge transport measurements on individual vertically aligned carbon nanofibers. *Applied Physics Letters* **2004**, *84* (20), 3972.

67. Liu, J.; Li, J.; Sedhain, A.; Lin, J.; Jiang, H., Structure and Photoluminescence Study of TiO₂Nanoneedle Texture along Vertically Aligned Carbon Nanofiber Arrays. *The Journal of Physical Chemistry C* **2008**, *112* (44), 17127-17132.
68. Bohm, D.; Pines, D., A Collective Description of Electron Interactions. I. Magnetic Interactions. *Physical Review* **1951**, *82* (5), 625-634.
69. Pines, D.; Bohm, D., A Collective Description of Electron Interactions: II. CollectivevsIndividual Particle Aspects of the Interactions. *Physical Review* **1952**, *85* (2), 338-353.
70. Bohm, D.; Pines, D., A Collective Description of Electron Interactions: III. Coulomb Interactions in a Degenerate Electron Gas. *Physical Review* **1953**, *92* (3), 609-625.
71. Ritchie, R. H., Plasma Losses by Fast Electrons in Thin Films. *Physical Review* **1957**, *106* (5), 874-881.
72. Stern, E. A.; Ferrell, R. A., Surface Plasma Oscillations of a Degenerate Electron Gas. *Physical Review* **1960**, *120* (1), 130-136.
73. Willets, K. A.; Van Duyne, R. P., Localized surface plasmon resonance spectroscopy and sensing. *Annual review of physical chemistry* **2007**, *58*, 267-97.
74. Kim, S.-S.; Na, S.-I.; Jo, J.; Kim, D.-Y.; Nah, Y.-C., Plasmon enhanced performance of organic solar cells using electrodeposited Ag nanoparticles. *Applied Physics Letters* **2008**, *93* (7), 073307.
75. Pillai, S.; Catchpole, K. R.; Trupke, T.; Green, M. A., Surface plasmon enhanced silicon solar cells. *Journal of Applied Physics* **2007**, *101* (9), 093105.
76. Beck, F. J.; Mokkaapati, S.; Catchpole, K. R., Plasmonic light-trapping for Si solar cells using self-assembled, Ag nanoparticles. *Progress in Photovoltaics: Research and Applications* **2010**, *18* (7), 500-504.
77. Beck, F. J.; Polman, A.; Catchpole, K. R., Tunable light trapping for solar cells using localized surface plasmons. *Journal of Applied Physics* **2009**, *105* (11), 114310.
78. Bohren, C. F., *Absorption and scattering of light by small particles*. New York : Wiley: New York, **1983**.
79. Wang, F.; Wang, Q.; Xu, G.; Hui, R.; Wu, J., Light Trapping on Plasmonic-Photonic Nanostructured Fluorine-Doped Tin Oxide. *The Journal of Physical Chemistry C* **2013**, *117* (22), 11725-11730.
80. Lu, R.; Konzelmann, A.; Feng, X.; Gong, Y.; Liu, J.; Liu, Q.; Xin, M.; Hui, R.; Wu, J., High Sensitivity Surface Enhanced Raman Spectroscopy of R6G on in situ Fabricated Au Nanoparticle/Graphene Plasmonic Substrates. *Wiley-VCH* **2014**.
81. Elliot, A. J.; Malek, G.; Wille, L.; Mao, B.; Han, S.; Wu, J. Z.; Talvacchio, J.; Lewis, R. M., Probing the Nucleation of Al₂O₃ in Atomic Layer Deposition on Aluminum for Ultrathin Tunneling Barriers in Josephson Junctions. *Ieee T Appl Supercon* **2013**, *23* (3).
82. Rochford, C.; Li, Z. Z.; Baca, J.; Liu, J. W.; Li, J.; Wu, J., The effect of annealing on the photoconductivity of carbon nanofiber/TiO₂ core-shell nanowires for use in dye-sensitized solar cells. *Applied Physics Letters* **2010**, *97* (4).
83. *Impedance spectroscopy : theory, experiment, and applications*. 2nd ed. / edited by Evgenij Barsoukov, J. Ross Macdonald.. ed.; Hoboken, N.J. : John Wiley: Hoboken, N.J., **2005**.
84. Lide, D. R., *CRC Handbook of Chemistry and Physics*. **2004**.

85. Liu, X.; Ramanathan, S.; Longdergan, A.; Srivastava, A.; Lee, E.; Seidel, T. E.; Barton, J. T.; Pang, D.; Gordon, R. G., ALD of Hafnium Oxide Thin Films from Tetrakis(ethylmethylamino)hafnium and Ozone. *J Electrochem Soc* **2005**, *152* (3), G213.
86. Lu, M.; Beguin, F.; Frackowiak, E., Supercapacitors: Materials, Systems and Applications. *John Wiley & Sons* **2013**.
87. Yu, G.; Xie, X.; Pan, L.; Bao, Z.; Cui, Y., Hybrid nanostructured materials for high-performance electrochemical capacitors. *Nano Energy* **2013**, *2* (2), 213-234.
88. Klankowski, S. A.; Pandey, G. P.; Malek, G.; Thomas, C. R.; Bernasek, S. L.; Wu, J.; Li, J., Higher-power supercapacitor electrodes based on mesoporous manganese oxide coating on vertically aligned carbon nanofibers. *Nanoscale* **2015**, *7* (18), 8485-94.
89. Huang, C.; Young, N. P.; Grant, P. S., Spray processing of TiO₂ nanoparticle/ionomer coatings on carbon nanotube scaffolds for solid-state supercapacitors. *Journal of Materials Chemistry A* **2014**, *2* (29), 11022.
90. *Review of the Research Program of the Partnership for a New Generation of Vehicles: Sixth Report*. The National Academies Press: Washington, DC, **2000**; p 132.
91. Klankowski, S. A.; Pandey, G. P.; Malek, G. A.; Wu, J.; Rojeski, R. A.; Li, J., A Novel High-Power Battery-Pseudocapacitor Hybrid Based on Fast Lithium Reactions in Silicon Anode and Titanium Dioxide Cathode Coated on Vertically Aligned Carbon Nanofibers. *submitted to Journal of Power Sources, under review* **2015**.
92. Armand, M.; Tarascon, J. M., Building better batteries. *Nature (London)* **2008**, *451* (7179), 652-657.
93. B.E., C., Electrochemical supercapacitors: scientific fundamentals and technological applications. *Kluwer Academic/Plenum: New York* **1999**.
94. Augustyn, V.; Simon, P.; Dunn, B., Pseudocapacitive oxide materials for high-rate electrochemical energy storage. *Energy & environmental science* **2014**, *7* (5), 1597-1614.
95. Bruce, P. G.; Scrosati, B.; Tarascon, J.-M., Nanomaterials for rechargeable lithium batteries. *Angewandte Chemie (International ed.)* **2008**, *47* (16), 2930-2946.
96. Okubo, M.; Hosono, E.; Kim, J.; Enomoto, M.; Kojima, N., Nanosize effect on high-rate Li-ion intercalation in LiCoO₂ electrode. *Journal of the American Chemical Society* **2007**, *129* (23), 7444-7452.
97. Chandrasekaran, R.; Magasinski, A.; Yushin, G.; Fuller, T. F., Analysis of Lithium Insertion/Deinsertion in a Silicon Electrode Particle at Room Temperature. *J Electrochem Soc* **2010**, *157* (10), A1139-A1151.
98. Chan, C. K.; Peng, H.; Liu, G.; McIlwrath, K.; Zhang, X. F., High-performance lithium battery anodes using silicon nanowires. *Nat Nanotechnol* **2008**, *3* (1), 31-35.
99. Park, M.-H.; Kim, M. G.; Joo, J.; Kim, K.; Kim, J., Silicon nanotube battery anodes. *Nano Lett* **2009**, *9* (11), 3844-3847.
100. Szczech, J. R.; Jin, S., Nanostructured silicon for high capacity lithium battery anodes. *Energy & environmental science* **2011**, *4* (1), 56-72.
101. Kasavajjula, U.; Wang, C.; Appleby, A. J., Nano- and bulk-silicon-based insertion anodes for lithium-ion secondary cells. *Journal of power sources* **2007**, *163* (2), 1003-1039.

102. Yao, Y.; McDowell, M. T.; Ryu, I.; Wu, H.; Liu, N., Interconnected silicon hollow nanospheres for lithium-ion battery anodes with long cycle life. *Nano Lett* **2011**, *11* (7), 2949-2954.
103. Liu, N.; Wu, H.; McDowell, M. T.; Yao, Y.; Wang, C., A yolk-shell design for stabilized and scalable li-ion battery alloy anodes. *Nano Lett* **2012**, *12* (6), 3315-3321.
104. Zamfir, M. R.; Hung Tran, N.; Moyen, E.; Lee, Y. H.; Pribat, D., Silicon nanowires for Li-based battery anodes: a review. *Journal of materials chemistry. A, Materials for energy and sustainability* **2013**, *1* (34), 9566-9586.
105. Cui, L.-F.; Yang, Y.; Hsu, C.-M.; Cui, Y., Carbon-silicon core-shell nanowires as high capacity electrode for lithium ion batteries. *Nano Lett* **2009**, *9* (9), 3370-3374.
106. Lee, S. W.; Kim, J.; Chen, S.; Hammond, P. T.; Shao-Horn, Y., Carbon nanotube/manganese oxide ultrathin film electrodes for electrochemical capacitors. *Acs Nano* **2010**, *4* (7), 3889-3896.
107. Qu, J.; Li, H.; Henry, J. J.; Martha, S. K.; Dudney, N. J., Self-aligned Cu-Si core-shell nanowire array as a high-performance anode for Li-ion batteries. *Journal of power sources* **2012**, *198*, 312-317.
108. Gohier, A.; Laik, B.; Kim, K.-H.; Maurice, J.-L.; Pereira-Ramos, J.-P., High-rate capability silicon decorated vertically aligned carbon nanotubes for Li-ion batteries. *Advanced materials (Weinheim)* **2012**, *24* (19), 2592-2597.
109. Fan, Y.; Zhang, Q.; Xiao, Q.; Wang, X.; Huang, K., High performance lithium ion battery anodes based on carbon nanotube-silicon core-shell nanowires with controlled morphology. *Carbon (New York)* **2013**, *59*, 264-269.
110. Klankowski, S. A.; Rojas, R. A.; Cruden, B. A.; Liu, J.; Wu, J.; Li, J., A high-performance lithium-ion battery anode based on the core-shell heterostructure of silicon-coated vertically aligned carbon nanofibers. *Journal of Materials Chemistry A* **2013**, *1* (4), 1055.
111. Klankowski, S. A.; Pandey, G. P.; Cruden, B. A.; Liu, J.; Wu, J., Anomalous capacity increase at high-rates in lithium-ion battery anodes based on silicon-coated vertically aligned carbon nanofibers. *Journal of power sources* **2015**, *276*, 73-79.
112. Zhu, G.-N.; Wang, Y.-G.; Xia, Y.-Y., Ti-based compounds as anode materials for Li-ion batteries. *Energy & environmental science* **2012**, *5* (5), 6652-6667.
113. Wang, J.; Polleux, J.; Lim, J.; Dunn, B., Pseudocapacitive Contributions to Electrochemical Energy Storage in TiO₂ (Anatase) Nanoparticles. *Journal of physical chemistry. C* **2007**, *111* (40), 14925-14931.
114. Shin, J.-Y.; Samuelis, D.; Maier, J., Sustained Lithium-Storage Performance of Hierarchical, Nanoporous Anatase TiO₂ at High Rates: Emphasis on Interfacial Storage Phenomena. *Advanced functional materials* **2011**, *21* (18), 3464-3472.
115. Yang, Z.; Choi, D.; Kerisit, S.; Rosso, K. M.; Wang, D., Nanostructures and lithium electrochemical reactivity of lithium titanates and titanium oxides: A review. *Journal of power sources* **2009**, *192* (2), 588-598.
116. Weng, Z.; Li, F.; Wang, D.-W.; Wen, L.; Cheng, H.-M., Controlled electrochemical charge injection to maximize the energy density of supercapacitors. *Angewandte Chemie (International ed.)* **2013**, *52* (13), 3722-3725.
117. Aida, T.; Yamada, K.; Morita, M., An Advanced Hybrid Electrochemical Capacitor That Uses a Wide Potential Range at the Positive Electrode. *Electrochemical and solid-state letters* **2006**, *9* (12), A534-A536.

118. Winter, M.; Brodd, R. J., What are batteries, fuel cells, and supercapacitors? *Chem Rev* **2004**, *104* (10), 4245-4270.
119. Zhang, S.; Pan, N., Supercapacitors Performance Evaluation. *Advanced energy materials* **2015**, *5* (6), n-a-n/a.
120. Edwards, P. P.; Porch, A.; Jones, M. O.; Morgan, D. V.; Perks, R. M., Basic materials physics of transparent conducting oxides. *Dalton Trans* **2004**, (19), 2995-3002.
121. Ferry, V. E.; Polman, A.; Atwater, H. A., Modeling Light Trapping in Nanostructured Solar Cells. *Acs Nano* **2011**, *5* (12), 10055-10064.
122. Kumar, A.; Zhou, C. W., The Race To Replace Tin-Doped Indium Oxide: Which Material Will Win? *Acs Nano* **2010**, *4* (1), 11-14.
123. Wang, F.; Subbaiyan, N. K.; Wang, Q.; Rochford, C.; Xu, G.; Lu, R.; Elliot, A.; D'Souza, F.; Hui, R.; Wu, J., Development of nanopatterned fluorine-doped tin oxide electrodes for dye-sensitized solar cells with improved light trapping. *ACS applied materials & interfaces* **2012**, *4* (3), 1565-72.
124. Tetreault, N.; Arsenault, E.; Heiniger, L. P.; Soheilnia, N.; Brillet, J.; Moehl, T.; Zakeeruddin, S.; Ozin, G. A.; Gratzel, M., High-efficiency dye-sensitized solar cell with three-dimensional photoanode. *Nano Lett* **2011**, *11* (11), 4579-84.
125. Yang, Z.; Gao, S.; Li, W.; Vlasko-Vlasov, V.; Welp, U.; Kwok, W. K.; Xu, T., Three-dimensional photonic crystal fluorinated tin oxide (FTO) electrodes: synthesis and optical and electrical properties. *ACS applied materials & interfaces* **2011**, *3* (4), 1101-8.
126. Forman, A. J.; Chen, Z.; Chakthranont, P.; Jaramillo, T. F., High Surface Area Transparent Conducting Oxide Electrodes with a Customizable Device Architecture. *Chemistry of Materials* **2014**, *26* (2), 958-964.
127. Atwater, H. A.; Polman, A., Plasmonics for improved photovoltaic devices. *Nature materials* **2010**, *9* (3), 205-13.
128. Ferry, V. E.; Munday, J. N.; Atwater, H. A., Design considerations for plasmonic photovoltaics. *Adv Mater* **2010**, *22* (43), 4794-808.
129. Catchpole, K. R.; Polman, A., Plasmonic solar cells. *Opt Express* **2008**, *16* (26), 21793-800.
130. Catchpole, K. R.; Polman, A., Design principles for particle plasmon enhanced solar cells. *Applied Physics Letters* **2008**, *93* (19), 191113.
131. Wu, J. L.; Chen, F. C.; Hsiao, Y. S.; Chien, F. C.; Chen, P. L.; Kuo, C. H.; Huang, M. H.; Hsu, C. S., Surface Plasmonic Effects of Metallic Nanoparticles on the Performance of Polymer Bulk Heterojunction Solar Cells. *Acs Nano* **2011**, *5* (2), 959-967.
132. Malek, G. A.; Aytug, T.; Liu, Q.; Wu, J., Plasmonic three-dimensional transparent conductor based on Al-doped zinc oxide-coated nanostructured glass using atomic layer deposition. *ACS applied materials & interfaces* **2015**, *7* (16), 8556-61.
133. Xu, G.; Liu, J.; Wang, Q.; Hui, R.; Chen, Z.; Maroni, V. A.; Wu, J., Plasmonic graphene transparent conductors. *Adv Mater* **2012**, *24* (10), OP71-6.